LA FISICA AL COLLIDER SpS DEL CERN (1980 – 1990)

L`idea di far circolare nella stesso sincrotrone un fascio di antiprotoni in un verso ed uno di protoni nell`altro era stata discussa da almeno 15 anni. Dopotutto, la ψ era stata scoperta nel 1974 ad un anello di accumulazione e^+e^-. La complicazione stava in

a) Disporre di un sincrotrone il cui vuoto fosse di qualita` tale da consentire la circolazione stabile di un fascio di alta intensita` per ore invece che per secondi;
b) Disporre di un sincrotrone in cui alimentazione e raffreddamento dei magneti permettessero di funzionare in continua per ore ad una energia vicina a quella massima;
c) Creare un sistema di raccolta e di accumulazione di antiprotoni, capace di fornire una corrente dell`ordine del 10% di quella del fascio di protoni
d) Creare un sistema di compattazione (“raffreddamento”) degli antiprotoni che li rendessero un bersaglio abbastanza denso.

Risolvere i problemi c), d) fu impresa di storica importanza.

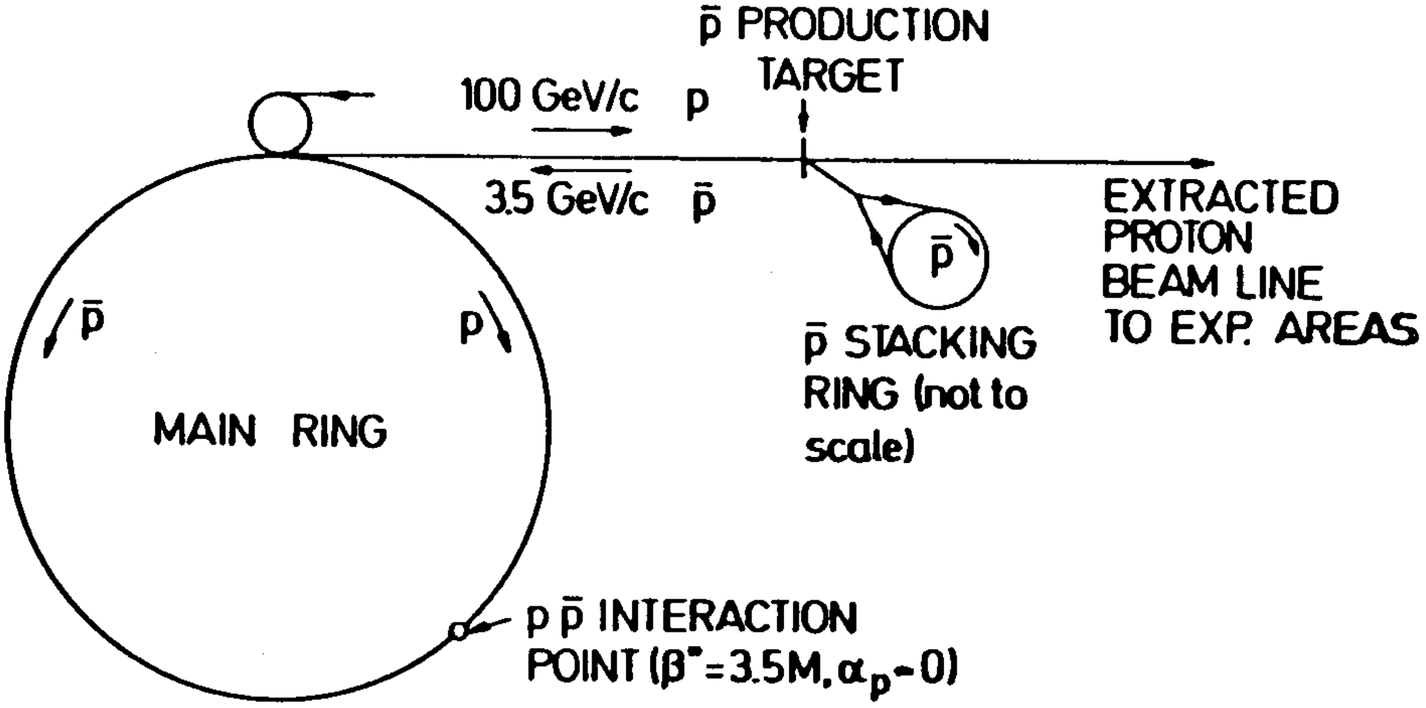

Fig. 5. General layout of the $p\bar{p}$ colliding scheme, from Ref. [9]. Protons (100 GeV/c) are periodically extracted in short bursts and produce 3.5 GeV/c antiprotons, which are accumulated and cooled in the small stacking ring. Then $\bar{p}$'s are reinjected in an RF bucket of the main ring and accelerated to top energy. They collide head on against a bunch filled with protons of equal energy and rotating in the opposite direction.

La idea fu originariamente proposta da C. Rubbia, D.Cline e P. Mac Intyre come una modifica del Main Ring da 450 GeV di Fermilab.

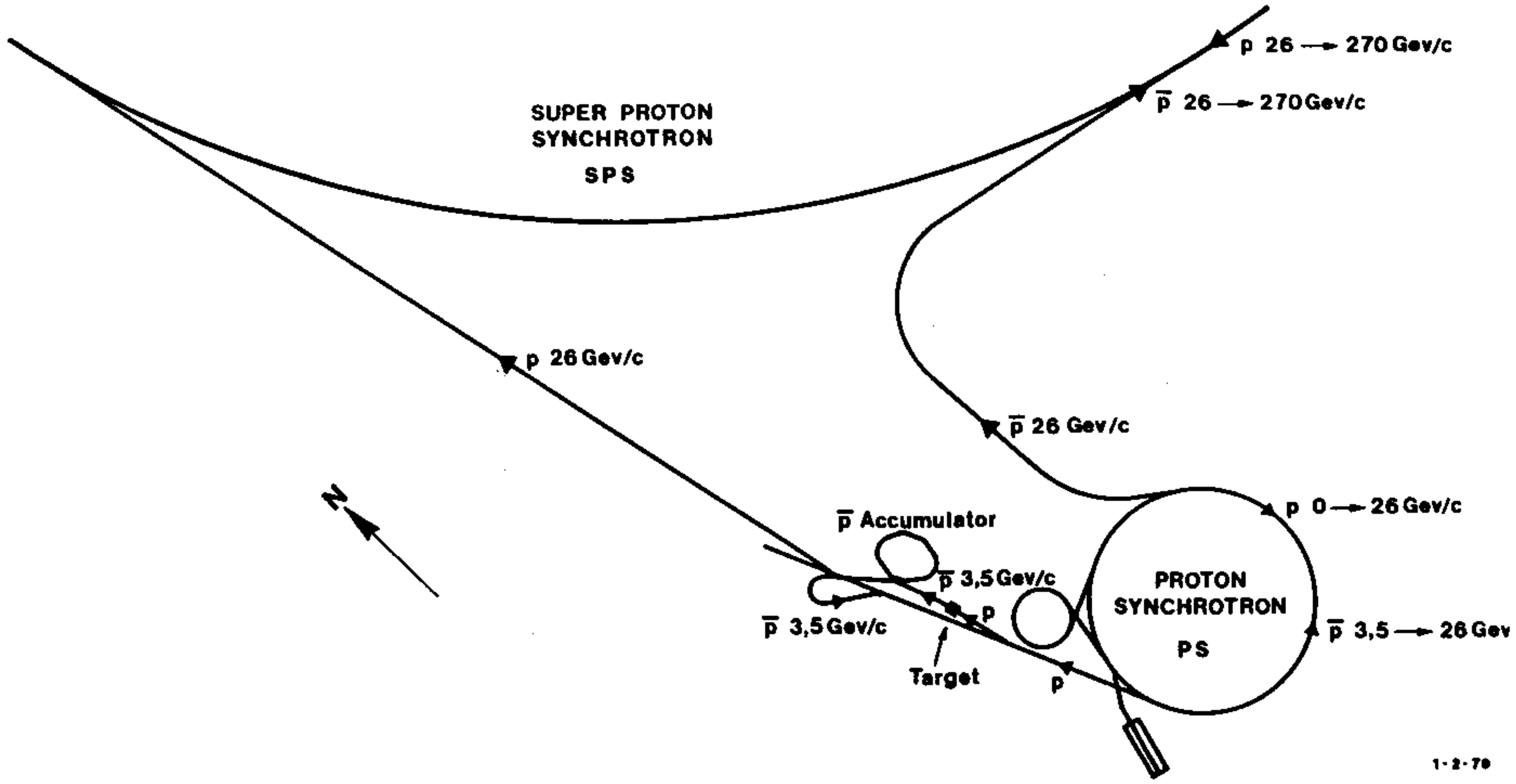

Fig. 1. Overall layout of the p$\bar{p}$ project.

Il progetto fu poi realizzato al CERN, dove furono costruiti l`accumulatore di antiprotoni ed una serie di canali per il trasferimento dei fasci.

ANTIPROTON PRODUCTION, STACKING, ACCELERATION

- The extracted 26 GeV/c proton beam from the CPS is directed to the antiproton production target.
- antiprotons are collected at 3.5 GeV/c and cooled in the accumulator.
- the rate of accumulated antiprotons was typically $3x10^6$/s.
- cooled antiprotons are redirected to the CPS and accelerated to 26 GeV/c.
- antiprotons are extracted from the CPS, injected into the SPS and accelerated from 26 to 270 GeV/c together with a pre-injected proton beam. Beams run against each other for several hours.
- design luminosity ~ $5x10^{28}$ $cm^{-2}s^{-1}$, achieved luminosity in the first collider run (1981-1985), L ~ 4.10^{29} .

In 1986 a second ring ACOL was included in the source and the collider energy was increased to 630 GeV. Operation with 6 circulating bunches became possible. The luminosity was boosted up to 3.10^{30} $cm^{-2}s^{-1}$. UA2 was optimized for the search for the top quark in a second run from winter 1987 to winter 1989.

PRINCIPLE OF STOCKASTIC COOLING

Suppose we measure with a sensor the transverse displacement of a particle at its maximum along the orbit. After ¼ betatron wavelength that particle will cross the equilibrium orbit at an angle proportional to the original displacement. A kicker can apply a bending and align the particle along the orbit.

The response time T_s of the sensor is by far too long, or equivalently the bandwidth W of the electronics is too narrow ($T_s = 1/2W$) to be able to distinguish one particle from another in a bunch. If N is the number of particles in a bunch rotating at a frequency f, the number of particles N_s affected by the signal will be $N_s = NfT_s = Nf/2W$.

The pickup and the correction signals will in reality be applicable to the r.m.s. displacement $<x^2_{rms}>$ of the N_s particles.

==

D. Mohl, Stockastic Cooling for Beginners, CERN 84-15, 1984, P.97.

S.van der Meer, Stockastic Cooling and the Accumulation of Antiprotons, Rew. Mod. Physics, Vol 57,No.3, part1, July 1985.

Let x^2_{rms}= average square displacement of a single particle.
$< x^2_{rms} >$ = average of x^2_{rms} over N_s particles: $< x^2_{rms} > = x^2_{rms}/N_s$

The decrease of x^2_{rms} per second will be

$$\frac{dx^2{}_{rms}}{dt} = \frac{-x^2{}_{rms} f}{N_s}, \quad and$$

$$x^2{}_{rms} = \left(x^2{}_{rms}\right)_0 e^{-\frac{ft}{N_s}}, \quad or\ x_{rms} = \left(x_{rms}\right)_0 e^{-\frac{ft}{2N_s}}$$

The last expression gives the damping time is $t_d = 2N_s/f = N/W$.

For a typical bandwidth of 250 MHz, one gets $t_d = 1$s for $2{,}5 \times 10^8$ p. Since at the CERN collider the number of collected antiprotons was about 3×10^6/s, the cooling rate was not a limit to the collider luminosity.

TRANSVERSE COOLING
(time domain)

The transit time from pick-up to kicker is made equal to the particle transit time. The betatron phase changes by an odd multiple of π/2 in a revolution. Because of the dependence of revolution time on particle momentum, mixing occurs. The population of a given phase volume changes largely in one revolution. On the other hand, mixing during the transit time from pick-up to kicker is smaller.

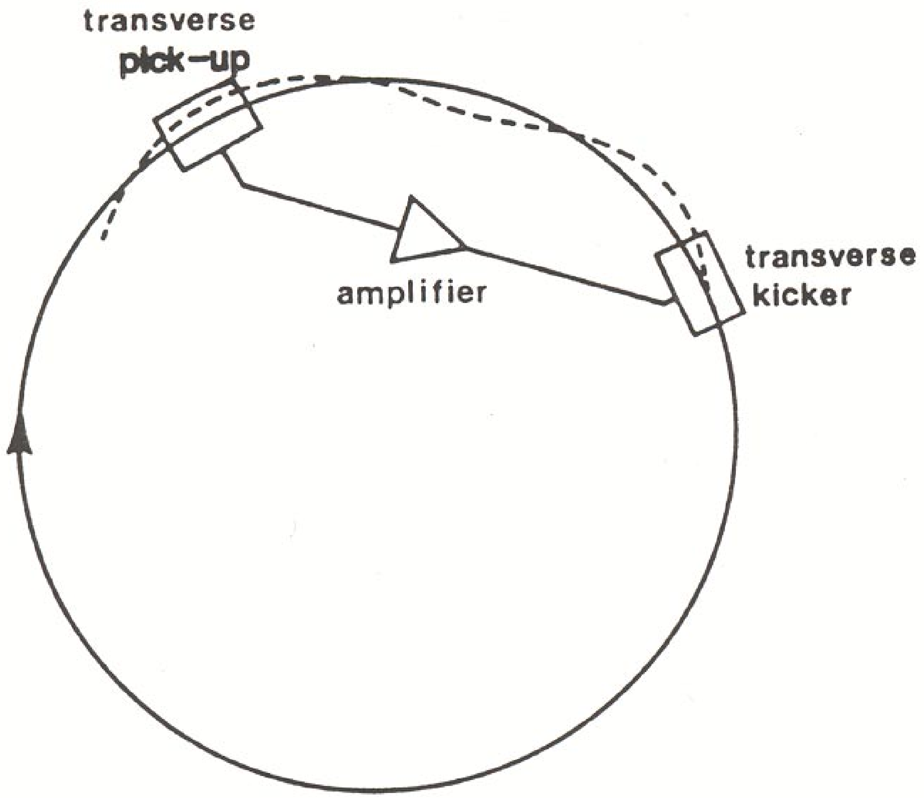

FIG. 2. Cooling of the horizontal betatron oscillation of a single particle.

LONGITUDINAL COOLING
(frequency domain)

Longitudinal cooling reduces the energy spread and increases the longitudinal density in the bunch. The simplest system works as for transverse cooling. The pick-up is placed in a region where dispersion is high, i.e. the particle position depends strongly on its momentum. The kicker must give a longitudinal kick and reduce momentum of particles with energy in excess of average, and viceversa.

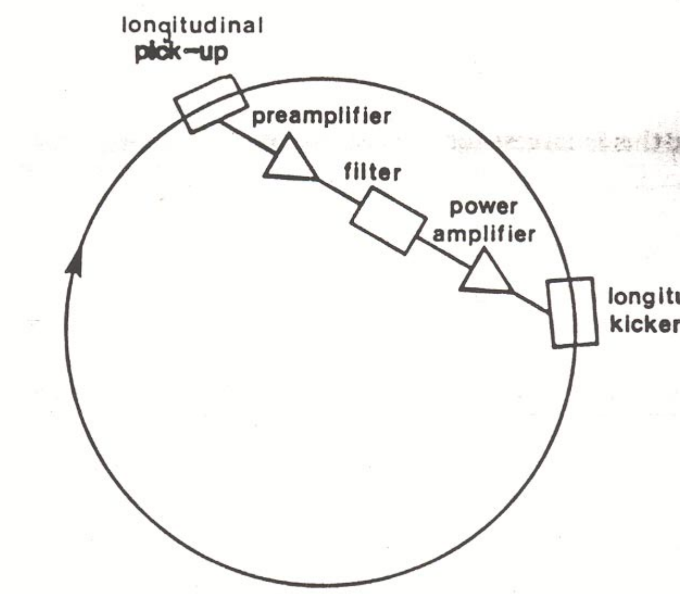

FIG. 7. Filter cooling.

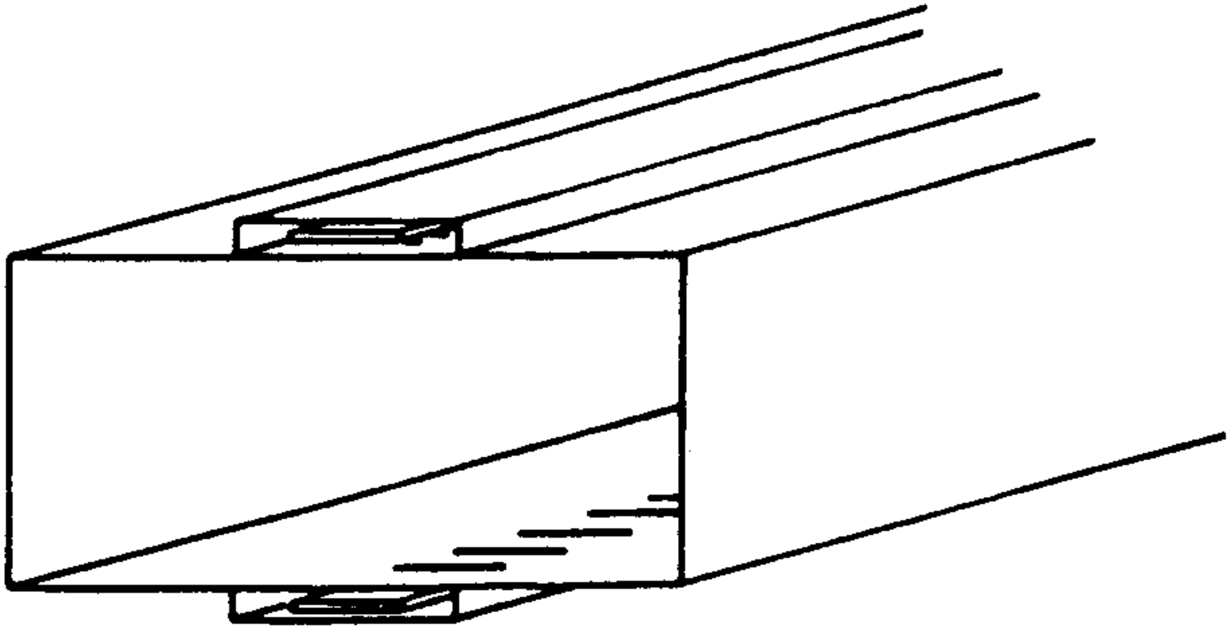

FIG. 10. Slot-type pick-up or kicker. One end of the transmission line is terminated with its own characteristic impedance.

Particles of different momenta have different rotation frequencies. Transmission line pick-ups/kickers with periodically varying characteristic impedance can select frequency bands and be used for longitudinal cooling.

694 S. van der Meer: Sto

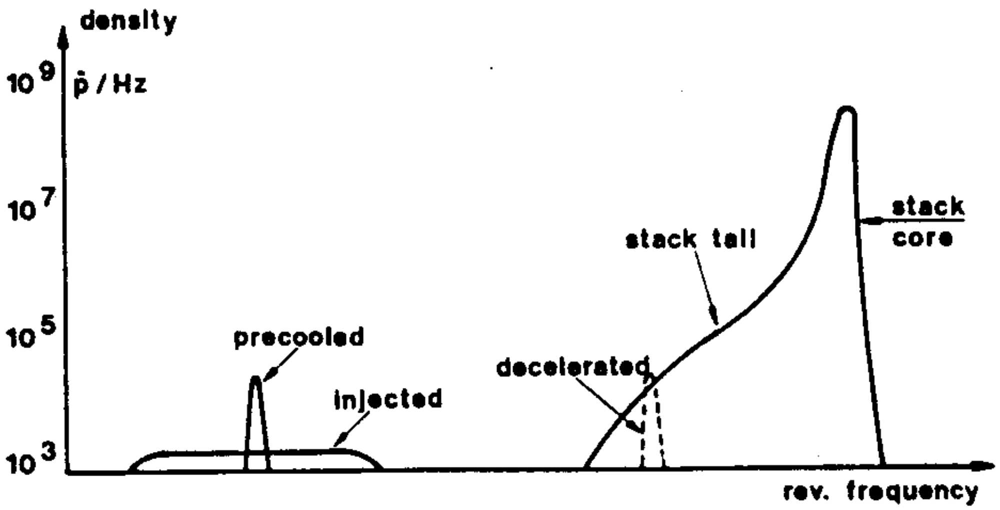

FIG. 11. Density distribution vs revolution frequency in the Antiproton Accumulator. On the right, the stack; on the left, the newly injected batch, before and after precooling.

A low density beam is injected every 2.5 s at large radii (left), in a region of large dispersion. The new beam is fully separated from the stack in these regions. Pick-ups and kickers can be installed here and can operate without affecting the stack. The new beam can thus be separately pre-cooled in about 2 s. The new beam is then r.f. bunched and decelerated in order to move to smaller radii, the r.f. is slowly switched off and the beam is stored in the stack tail. In order to free phase space for a new injection, a longitudinal cooling system operates on the tail and moves the new beam further to the stack core.

Filtered coolers can be phase-tuned to cool preferentially
the stack tail. The stack tail
is quickly cooled in 2.4 s both longitudinally and transversally.

Perturbations induced in the core are slowly corrected with additional low-power coolers.

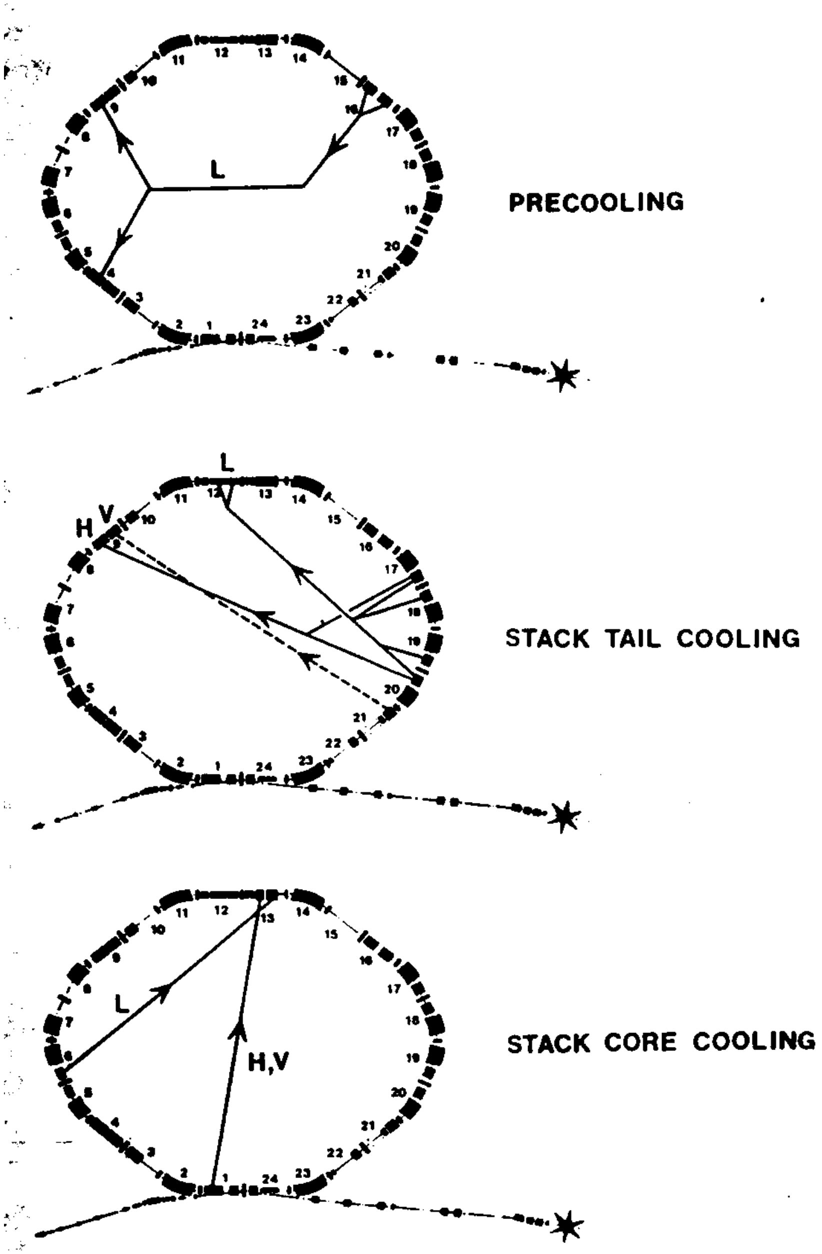

G. 14. Plan of the AA ring with its 7 cooling systems.
=longitudinal, V=vertical, H=horizontal.

To transfer cool antiprotons to the PS and later to the SPS, the core was r.f. bunched and bunched antiprotons were accelerated through the tail till reaching the same orbit where normally particles were injected. During the acceleration process the continuous store tail was practically unaffected.

From the outer injection orbit the bunched beam could be fast extracted without affecting the store.

Typically 30% of the store, about $6x10^{10}$ antiprotons, were extracted each time.

==

D.Moel et al., Physics Reports 58, No.2 (1980), p.73.

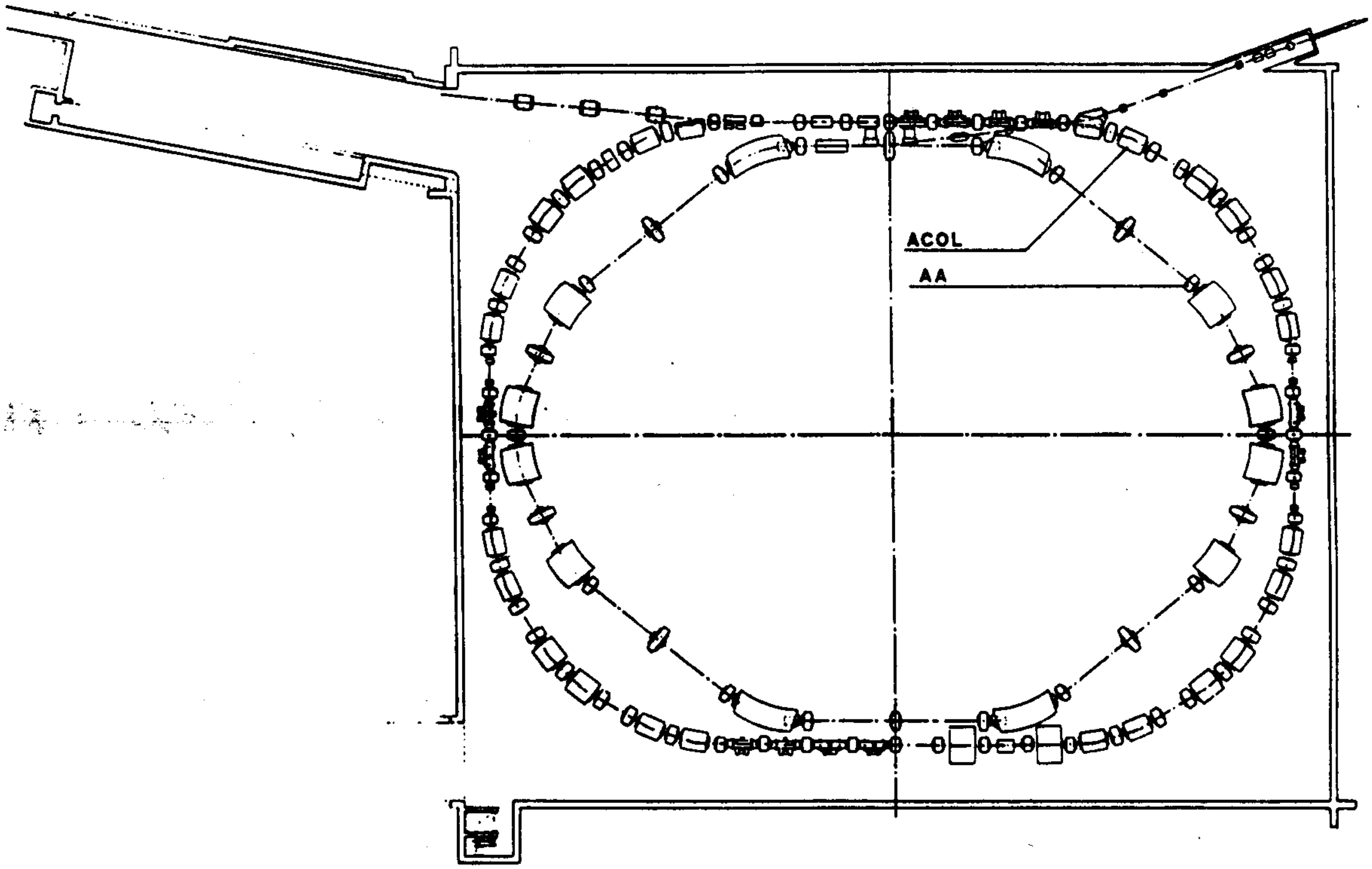

Гhe new ACOL ring (under construction) around the AA. This ring will increase the stacking rate by an order of m stack will still be kept in the AA ring.

A second generation antiproton source implemented an intermediate strong focusing, large acceptance ring ACOL before the accumulator proper. More antiprotons could be accepted in each shot and pre-cooled in ACOL before being stacked in AA.

THE CERN SPS COLLIDER EXPERIMENTS
(in Underground Areas)

1) UA1 : 4π magnetic detector: search for W,Z
2) UA2 : search for W,Z
3) UA3 : search for magnetic monopoles
4) UA4 : elastic scattering and total cross section
5) UA5 : overall survey of inelastic events

Main results:

a) Discovery of W,Z : UA1, UA2
b) Discovery of parton jets : UA2, UA1

Integrated luminosity:
in run 1 (1981 to 1985, $\sqrt{s} = 540$ GeV) ~ 0,9 pb^{-1} by both experiments
in run 2 (1988 to 1990, $\sqrt{s} = 630$ GeV) ~ 4,7 pb^{-1} by UA1, ~ 7,1 pb^{-1} by UA2.

THE BIRTH OF CALORIMETER-DOMINATED 4π DETECTORS

-Detection of high p_t jets emphasizes calorimetry over tracking.
Typical resolution of a sampling electromagnetic calorimeter:

$$\frac{\Delta E}{E} = \frac{0{,}15}{\sqrt{E(GeV)}} = 1{,}5\%\ at\ E = 100\ GeV$$

which is a factor of 10 (UA1) to 6 (CDF) better than what one can obtain at 100 GeV with a curvature measurement in a 4π detector.
Typical resolution of a sampling hadronic calorimeter:

$$\frac{\Delta E}{E} = \frac{0{,}70}{\sqrt{E(GeV)}} = 7\%\ at\ 100\ GEV$$

a factor of 3 to 2 better than what one can obtain with a curvature measurement, and a more unbiased measurement of electron energy.
-Search for neutrinos by $E_{t,miss}$ measurement dictates hermetic detectors.
-Large multiplicity of jet prongs calls for highly segmented calorimeters in order to make sure that the entire jet is measured.

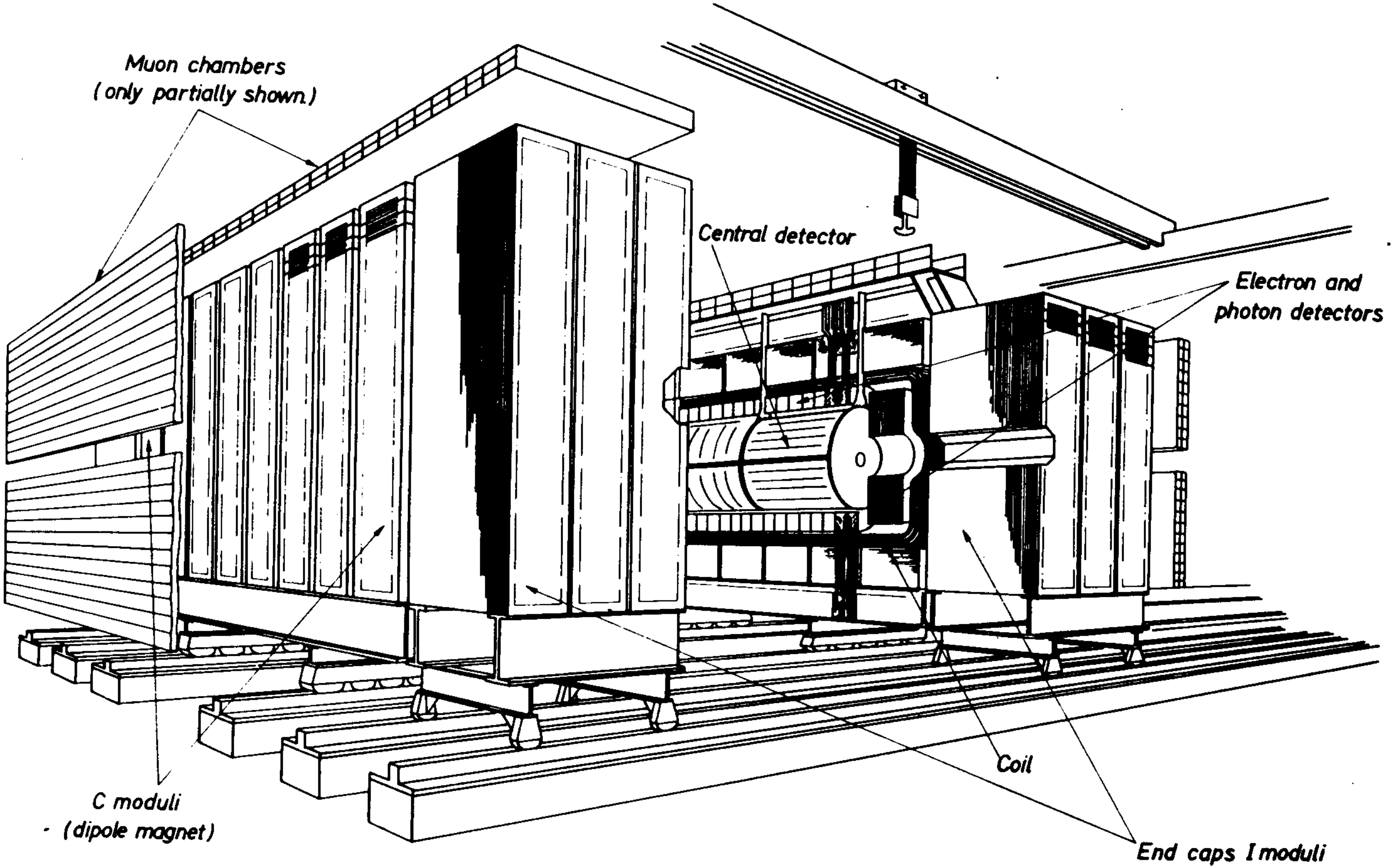

Fig. 1. The Large Angle Detector of the UA1 Apparatus.

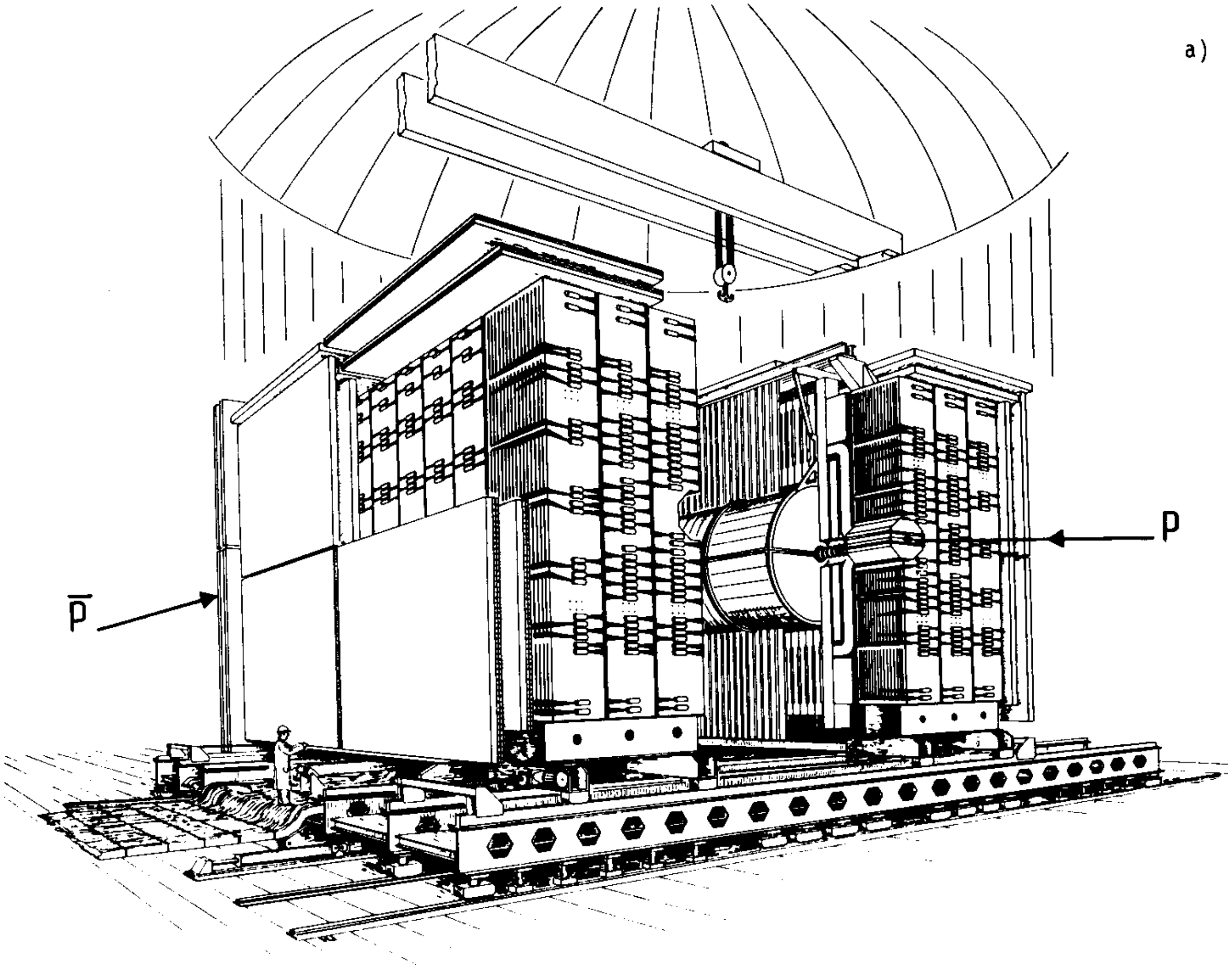

The UA1 detector was housed in an underground cavern.

PARAMETERS OF THE UA1 DETECTOR

-horizontal dipole magnetic field of 7 KG
-box of image chambers with 8000 wires up to 5m long, with ~200µm resolution, covering the full azimuth
-a telescope of twin C-shaped electromagnetic calorimeters at large angles, in a raw along the beams ("gondolas"), with 4 longitudinal compartments
-iron flux return yoke instrumented with plastic scintillator to form a hadron calorimeter, with 2 longitudinal compartments
-end-cap e.m. and hadron calorimeters at angles $25° < \theta < 5°$
-8 planes of large drift chambers enclosing the detector volume to signal traversing muons.

====================================

Anne Kernan, Proc. of the Proton-Antiproton Collider Physics 1981 Workshop, Madison Wisconsin, V.Barger et al. Editors, p. 325.

The central drift chamber assembly was 6m long and 2,4 m in diameter. Wires were parallel to the field, and electron drift over a distance up to 18 cm was transverse to it.

The hit position along the wires was measured by charge division.

2-track resolution was ~ 3 mm. Specific ionization loss dE/dx was measured over the whole volume, with a resolution of ~16%.

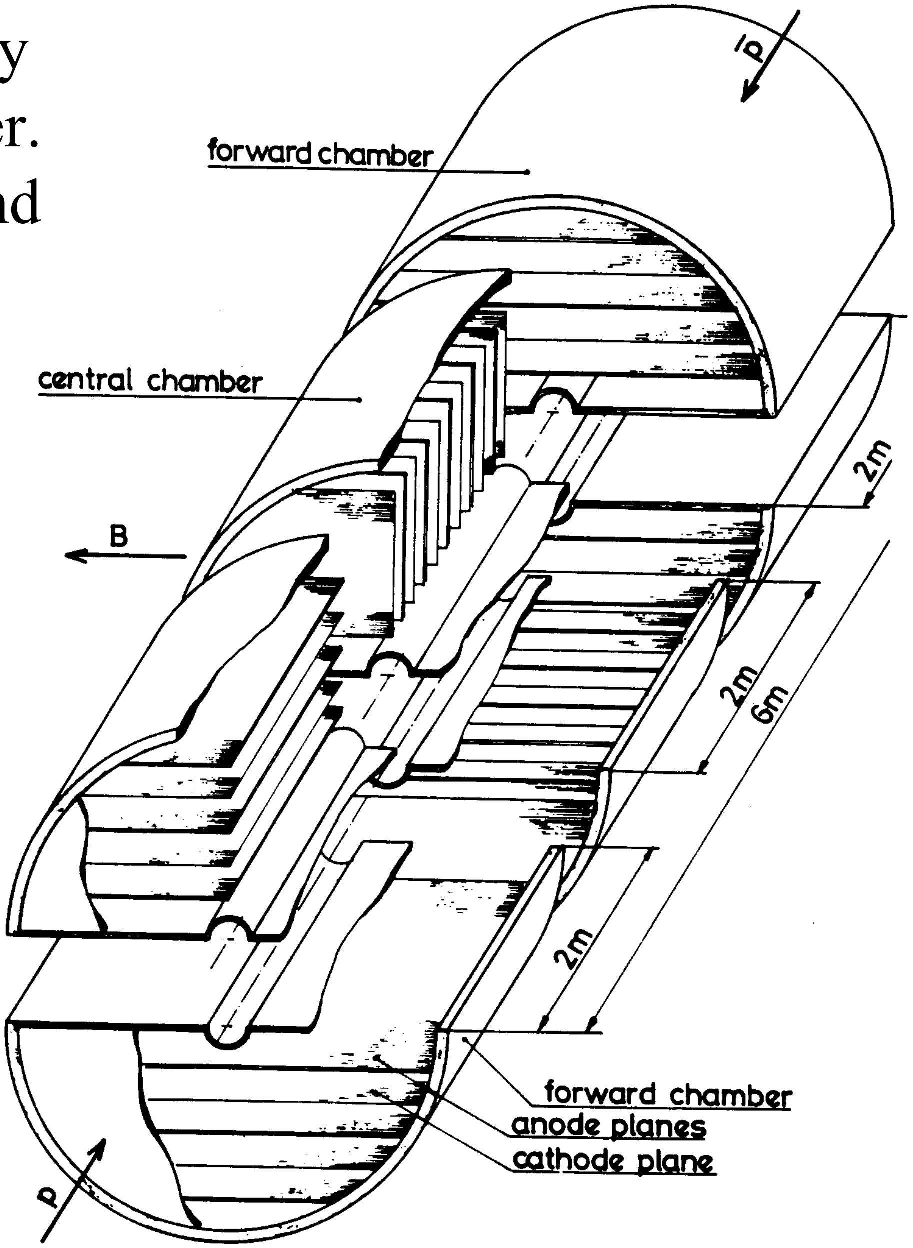

Fig. 4. The Central Detector "image" drift chambers.

48 double “gondolas” in a row form the central e.m. calorimeter at 25° < θ < 155°. End-walls extend the coverage and cover the range 25° > θ > 5°.

Counters are sandwiches of 1,2 mm lead interleaved with 1,5 mm scintillator.

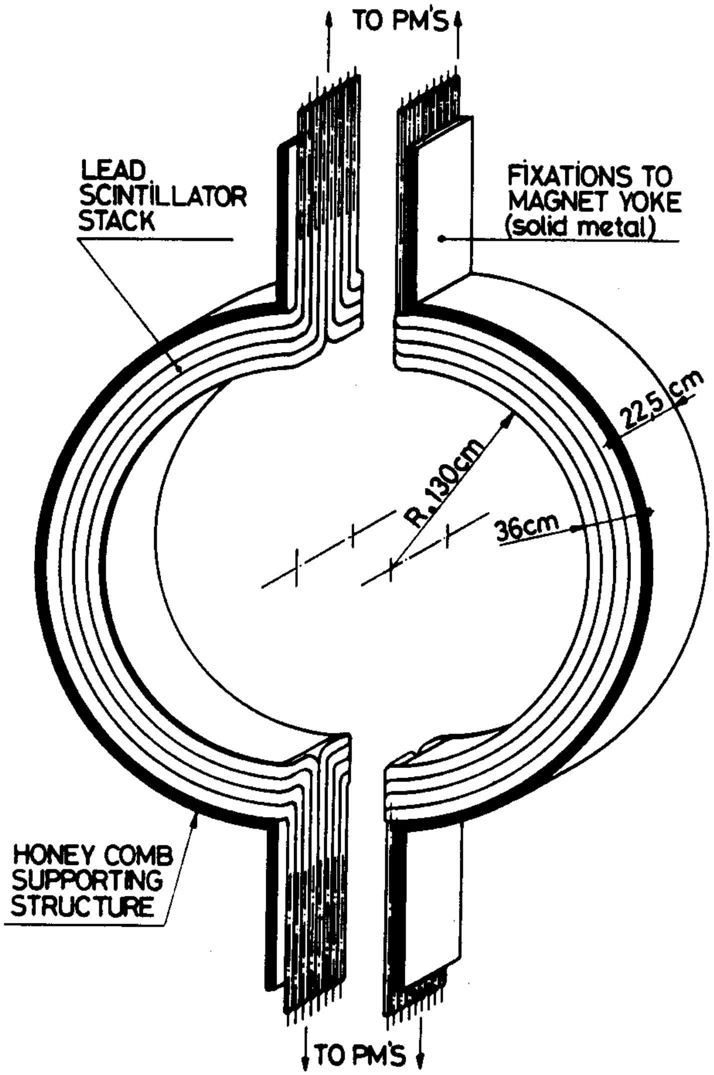

Fig. 3. Two units of the large angle electromagentic calorimeter.

8 independent C-shaped magnet sections providing a uniform horizontal field of 0,7T over a volume of 7,2x3,5x3,2 m^3.
Yoke is instrumented with 1cm scintillator every 5 cm iron, into a hadron calorimeter 5,5 interaction lengths thick.

Additional end-cap walls of similar construction extend the calorimeter coverage to $-3{,}0 < \eta < +3{,}0$.

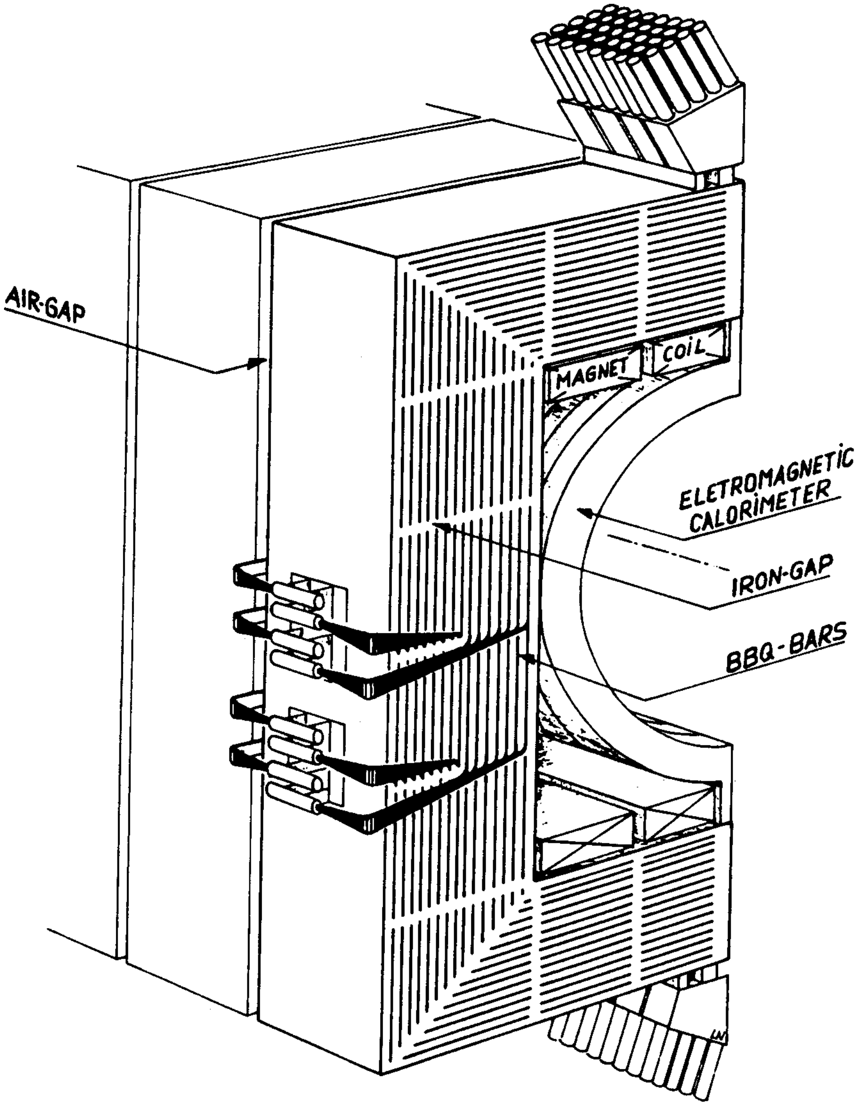

Fig. 2. One of the 16 "C" models comprising the magnet yoke and hadron calorimeter.

The exterior of UA1 was covered at θ > 10° by two tracking detectors made of sandwiches of 4 staggered drift tube planes.

Detectors were ~ 60 cm apart to allow measuring the exit direction of candidate muons

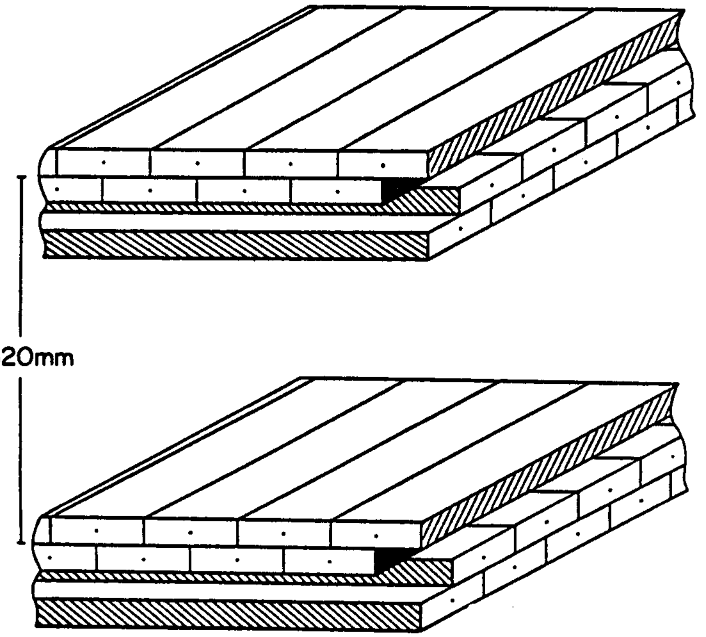

Fig. 6. Muon chamber setup.

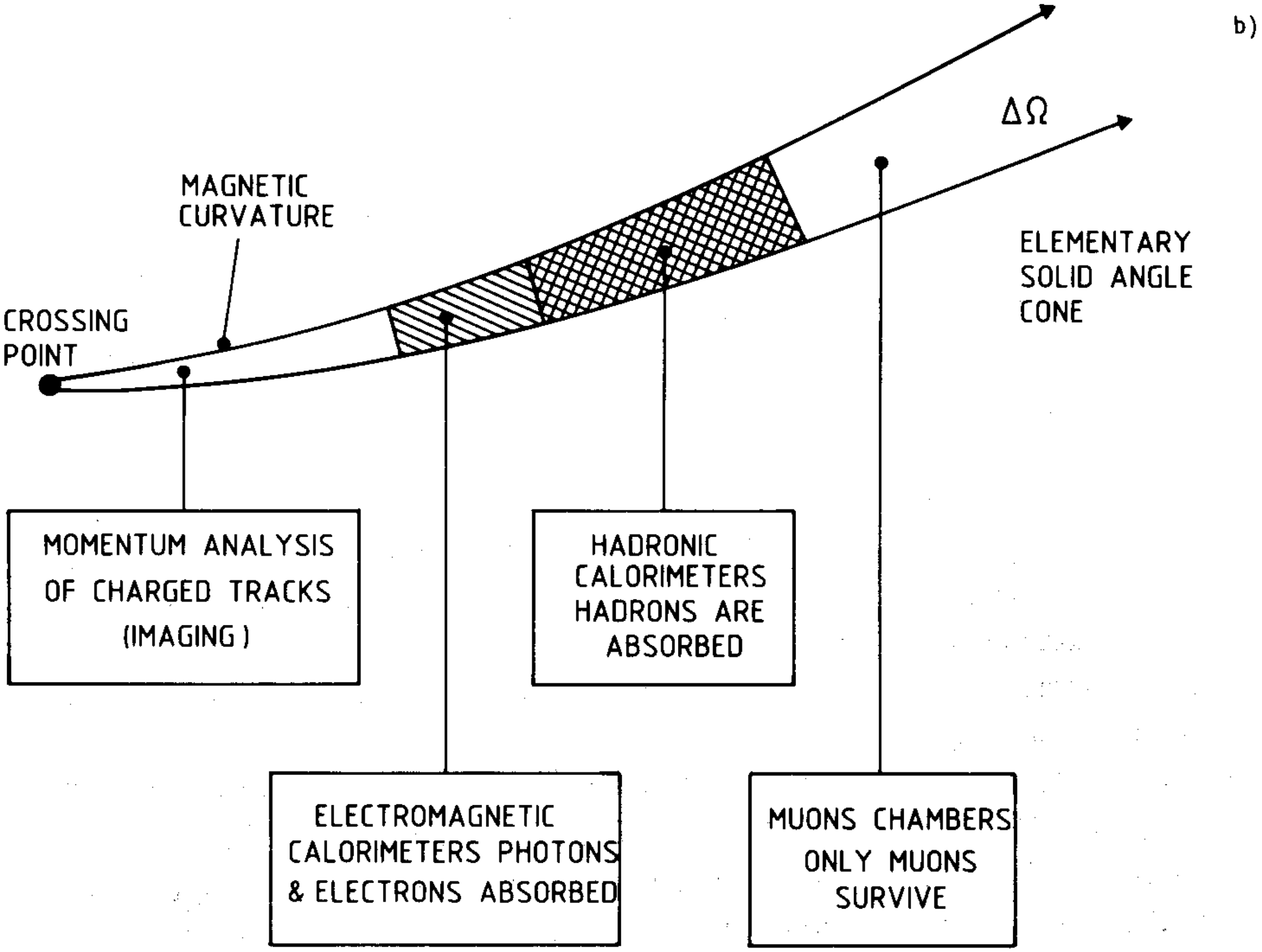

Fig. 8b. The schematic functions of each of the elementary solid-angle elements constituting the detector structure.

UA1 measured particle momentum, energy and penetration. Electron and muon momentum, and electron energy were measured.

Separation of electrons from pions was achieved by requiring the proper energy deposition in the first and in the last electromagnetic compartments, and a minimal had/e.m. signal ratio..

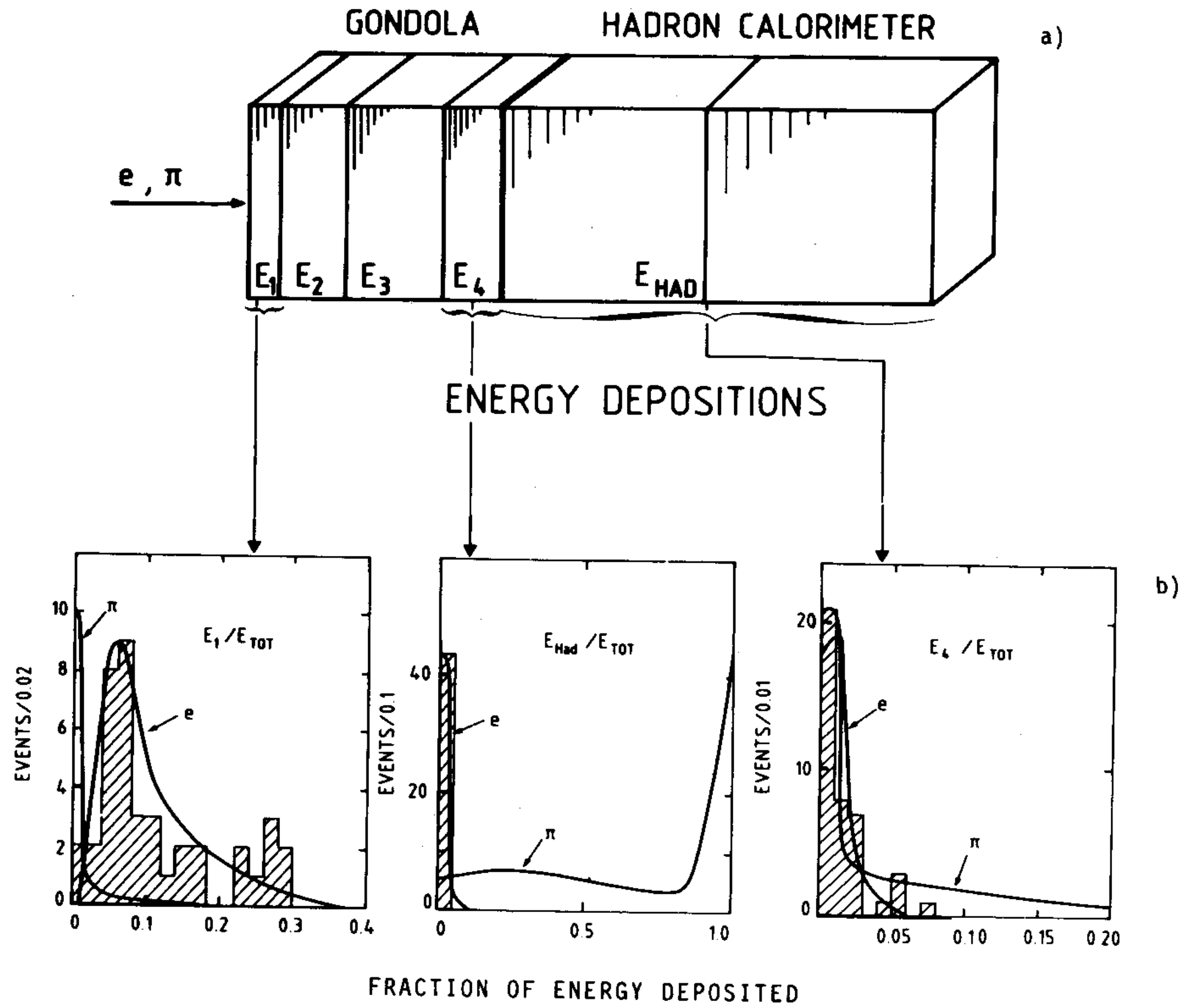

Fig. 9. a) Schema of an elementary solid-angle cell. After four segments of lead/scintillator sandwich, there are two elements of iron/scintillator sandwich, which is also the magnetic field return loop. b) Energy depositions for high-energy pions and electrons. The nature of the particle can be discriminated looking at the transition curve.

A significant momentum imbalance may indicate a missing neutrino.

An energy flow vector is associated to each calorimeter cell and the total transverse energy vector is constructed.

In the case of a missing neutrino,

$$\vec{P}_\nu = -\Sigma \vec{E}_t$$

CONSTRUCTION OF ENERGY VECTORS

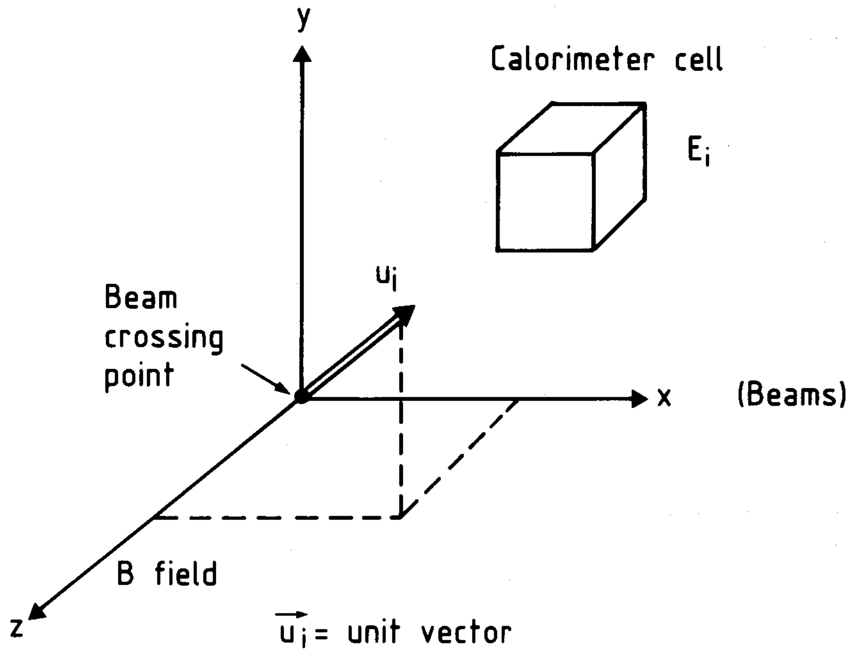

$\vec{u}_i$ = unit vector

$\vec{E}_i = E_i \vec{u}_i$

Momentum conservation (ideal detector) $\longrightarrow \Sigma_i \vec{E}_i = 0$

$\Delta \vec{E}_m = \Sigma \vec{E}_i$

$\Sigma |E_T|$ = event "temperature"

THE FERMI MODEL OF WEAK INTERACTIONS

332 *G. Salvini and A. Silverman, Physics with matter–antimatter colliders*

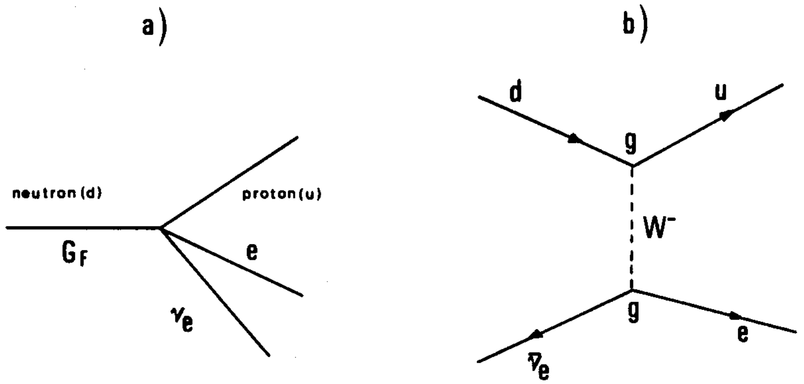

Fig. 3.1. (a) Point-like four-fermion interaction of the Fermi theory. (b) G_F is replaced by a coupling constant g at each quark and lepton vertex.

In the Fermi model the $e\nu_e$ lepton pair is radiated directly by the neutron, as a photon is radiated by an electron. The coupling constant is $G_F \sim 1{,}17.10^{-5}$ GeV^{-2} rather than α_e. However, in this model weak cross sections diverge with energy,

e.g. $\sigma_{Born}(\nu_\mu e^- \to \nu_e \mu^-) = (4G_F^2/\pi)k^2$ (k = cms momentum)

A W propagator avoids the divergence by introducing a cutoff at $\sqrt{s} \sim m_W$. The new W particle was searched primarily in the $W \to e\upsilon$ channel (however, UA1 exploited also the $W \to \mu\nu$ decay).

The neutrino charged current cross section was still in agreement with the Fermi model.

The charged mediator W had to be very heavy. (M>>40 GeV from the data shown).

LOWER LIMIT TO A CHARGED WEAK PROPAGATOR

C. Rubbia 241

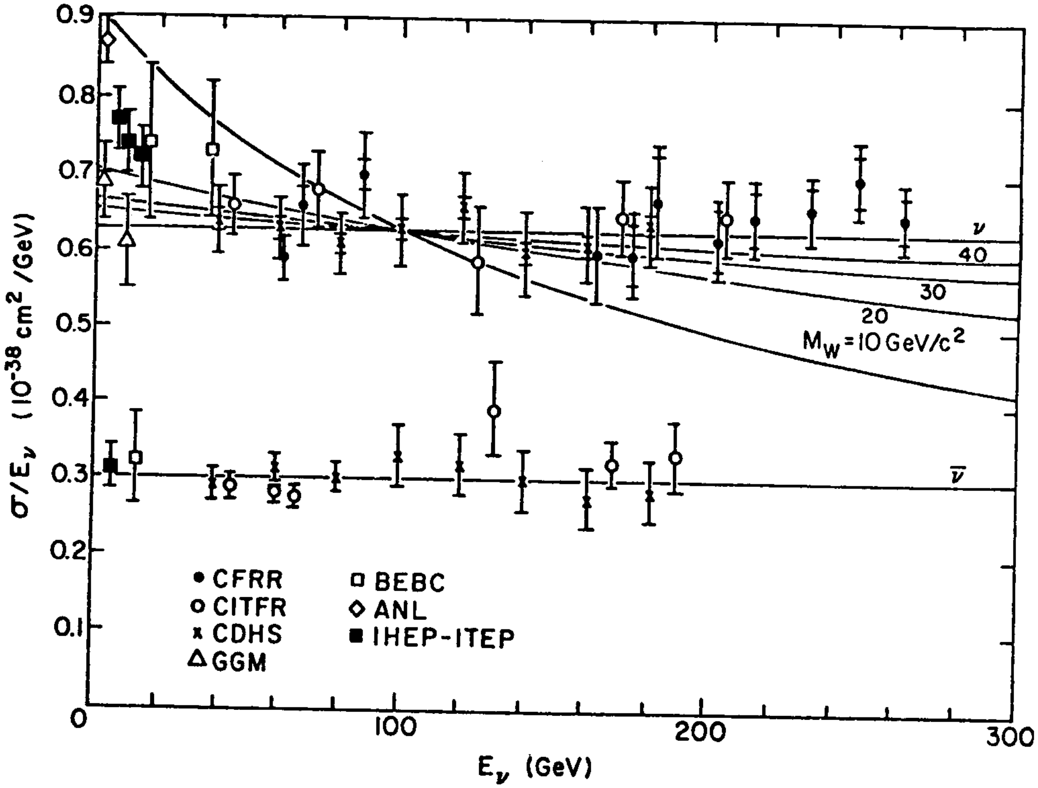

Fig. 1. The muon neutrino and antineutrino charged-current total cross-section as a function of the neutrino energy. Data are from the Particle Data Group (Rev. Mod. Phys. *56,* No. 2, Part 2, April 1984) reprinted at CERN. The lines represent the effects of the W propagator.

The same diagrams would be responsible for neutron and proton (in nuclei) weak decay and for W^+, W^- production in quark-antiquark collisions.

The weak interaction cross sections are readily computed.

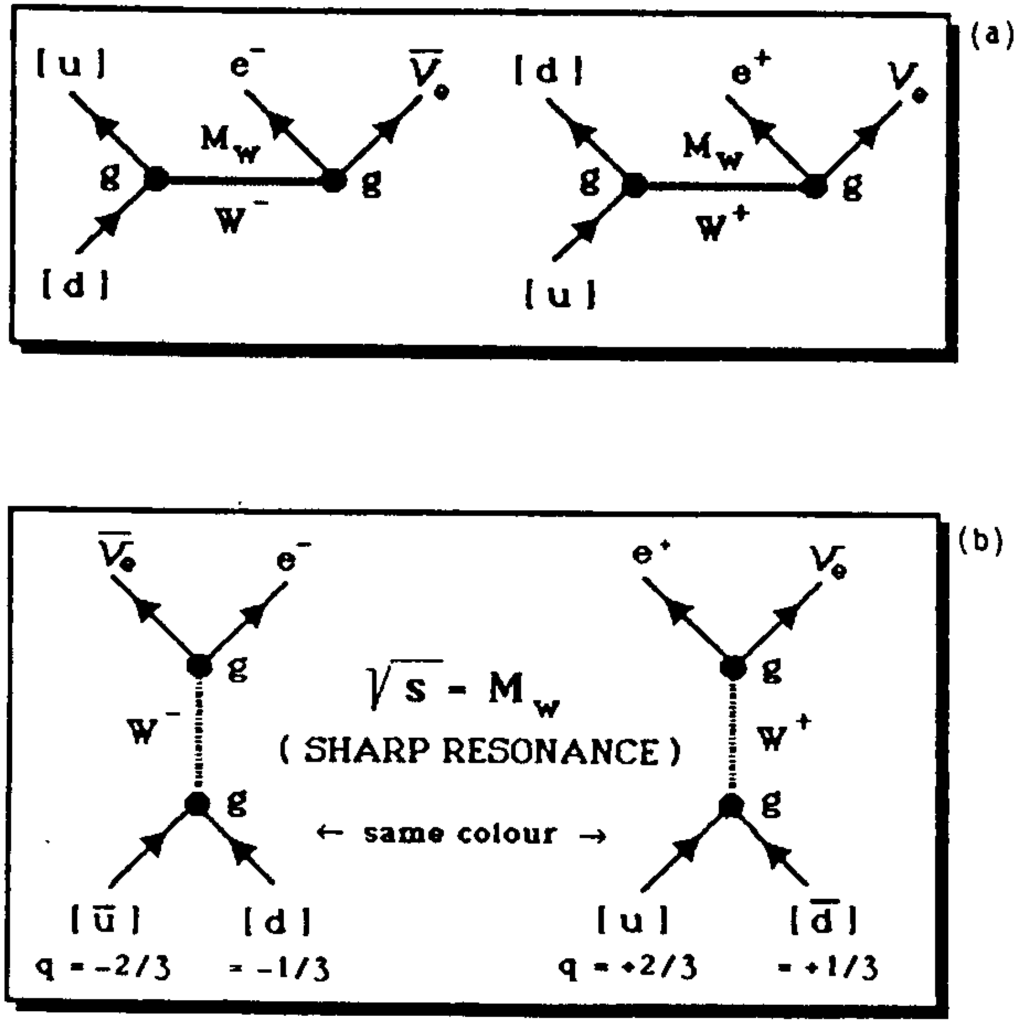

FIG. 2. (a) Feynman diagram of virtual *W* exchange mediating the weak process [reaction (2)]. (b) Feynman diagram for the direct production of a *W* particle. Note that the quark transformation has been replaced by a quark-antiquark annihilation.

The structure functions F(x) measured in neutrino and in electron scattering provide the parton momentum distributions in the proton: $F_2(x) = xu(x)$. At large Q^2 one may assume that these functions give the equivalent beam and target densities, and that they factorize with interaction cross sections.

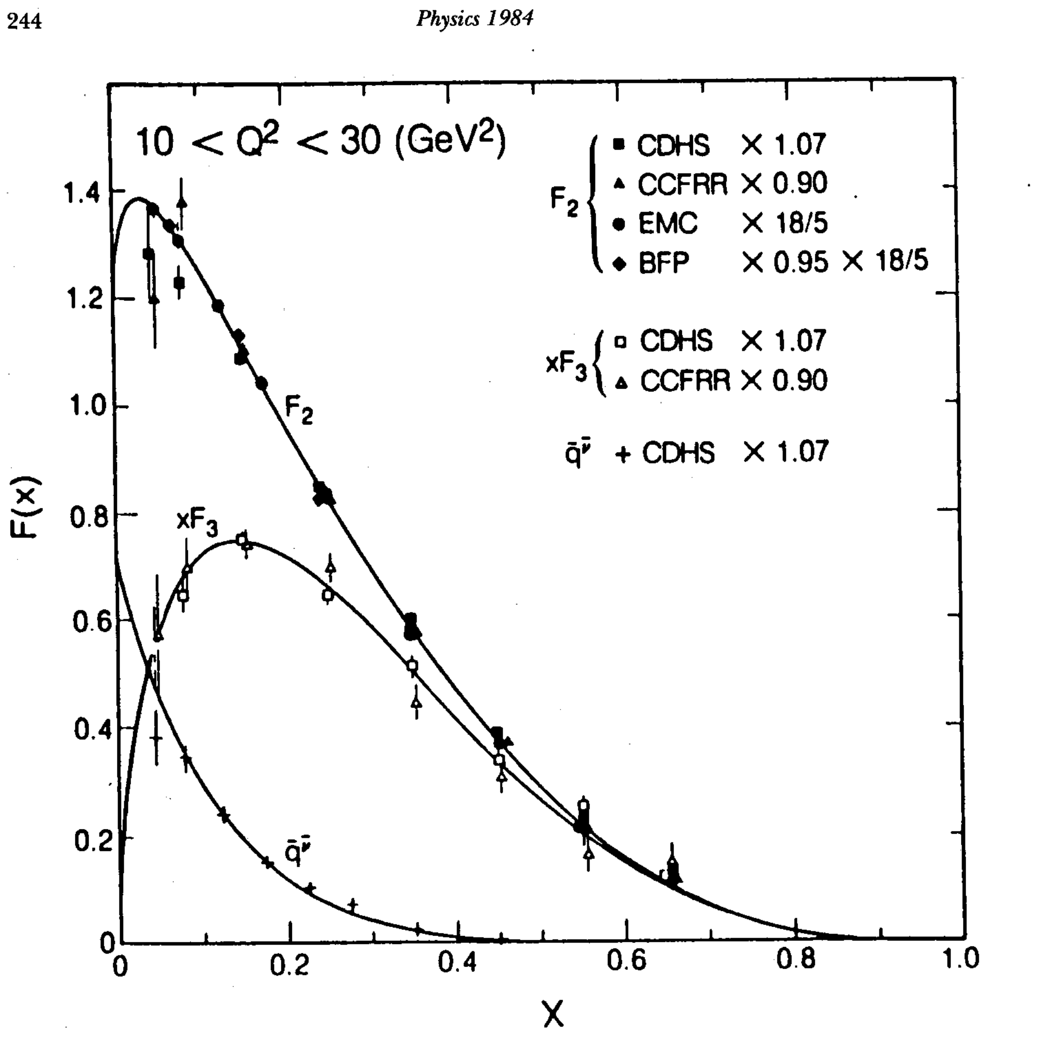

In order to predict the event rate, one convolutes the parton cross sections with the parton structure functions.

PRODUCTION CROSS SECTION OF CHARGED W

Neglecting the W width, the cross section for the process $\mathrm{u} + \underline{\mathrm{d}} \rightarrow \mathrm{W}^{+}$ is $\hat{\sigma}(x_1, x_2) = \sqrt{2}\pi G M_W^2 \cos^2 \vartheta_c \delta(x_1 x_2 s - M_W^2)$

and the product of the parton fluxes is $F^{+}(x_1, x_2) = \frac{1}{3}\left[u(x_1)d(x_2) + d(x_1)u(x_2)\right]$

giving a production cross section at the Collider

$$\sigma(W^{+}) = \int_0^1 dx_1 \int_0^1 dx_2 \hat{\sigma}(x_1, x_2) F^{+}(x_1, x_2)$$

One integration can be made by exploiting the δ function:

$$\sigma(W^{+}) = \sqrt{2}\pi G \frac{M_W^2}{s} \cos \vartheta_c \int_{\frac{M_W^2}{s}}^{1} \frac{dx}{x} F^{+}(x, \frac{M_W^2}{xs})$$

(remember that $\int f(x)\delta[g(x)]dx = \frac{f(x_0)}{|g'(x_0)|}, \quad where\ g(x_0) = 0$)

==

L.di Lella, notes of lectures to the Pisa graduate students (1993 ?)

At $\sqrt{s} = 540$ GeV and for $m_W = 80$ GeV, the W production cross section is $\sigma B = 0.54 \times 10^{-33}$ cm^2. $B(W \rightarrow e\upsilon) \sim 11\%$

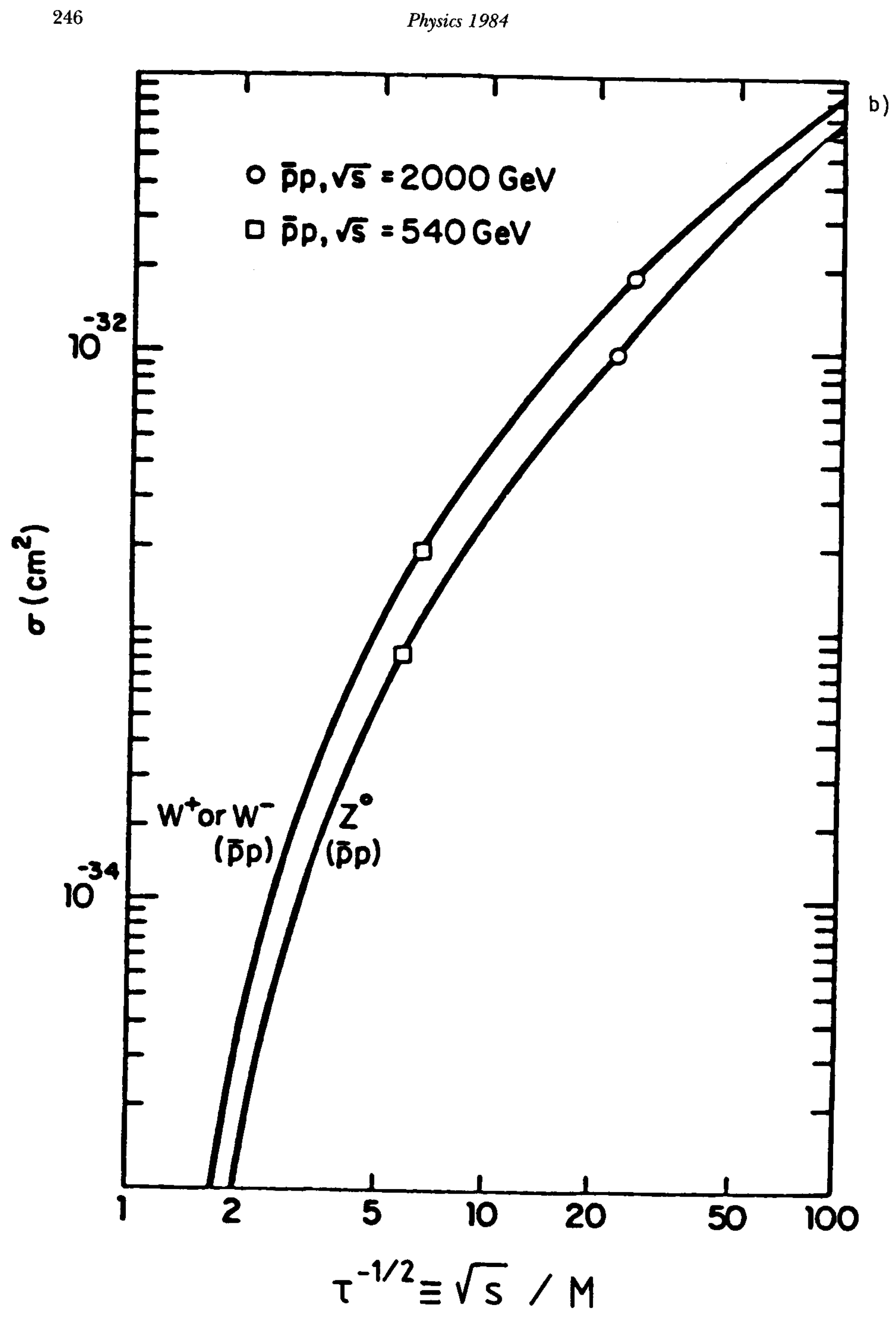

246

Physics 1984

THE STANDARD MODEL W WIDTH

The Fermi constant determines the partial W width into leptons:

$$\Gamma(W \to e\nu_e) = \Gamma(W \to \mu\nu_\mu) = \Gamma(W \to \tau\nu_\tau) \cong 232 \quad MeV$$

The width into quark pairs depends on the CKM matrix elements and on α_s. For quarks of negligible mass:

$$\frac{\Gamma(W \to q\overline{q}')}{\Gamma(W \to e\nu_e)} = 3|U_{qq'}|^2(1+\frac{\alpha_s}{\pi}) \approx 3$$

the factor 3 being due to color, and assuming the dominant U_{qq} to be ~1. If the W→tb channel is closed there are 2 quark decay channels and $\Gamma_W = 3\Gamma_{leptonic} + 2\Gamma_{hadronic} = (3+6)\Gamma_{leptonic} \cong 2{,}09\ GeV$

$$B(e\nu) = \frac{\Gamma(e\nu)}{\Gamma_W} \cong \frac{1}{9}$$

Below m_t ~ 60 MeV the W→tb decay would have an appreciable rate as:

$$\frac{\Gamma(tb)}{\Gamma(e\nu)} = 3|U_{tb}|^2\left(1-\frac{m_t^2}{M_W^2}\right)^2\left(1+\frac{1}{2}\frac{m_t^2}{M_W^2}\right)\left(1+\frac{\alpha_s}{\pi}\right)$$

THE STANDARD MODEL Z WIDTH

Z couples to leptons and quarks with vector V and axial-vector A couplings. Quark channels are favored because of a color factor 3 and of a small QCD correction:

$$\Gamma(Z \to l\bar{l}) = \frac{GM_Z^2}{24\pi\sqrt{2}}(V_l^2 + A_l^2)$$

$$\left|A_{fermion}\right| = (1 - 4Q_{fermion}\sin^2\vartheta_W)$$

$$\Gamma(Z \to q\bar{q}) = 3\frac{GM_Z^2}{24\pi\sqrt{2}}(V_q^2 + A_q^2)(1 + \frac{\alpha_s}{\pi})$$

A couplings depend on the fermion charge. In particular ee, μμ decay widths are reduced due to a conspiracy between the lepton charge being 1 and $\sin^2\theta_W \sim 1/4$. V couplings vary because the Weinberg angle plays a different role from one case another. The result is

$\Gamma(\nu\nu)$ =171 MeV, $\Gamma(\nu\nu)/\Gamma(e^+e^-)/\Gamma(uu)/\Gamma(dd)$ = 2/1.01/3.46/4.45,

Γ_Z = 2,58 GeV, $B(e^+e^-) = \Gamma(e^+e^-)/\Gamma_Z \sim$ 3,3%.

In the UA1 search for W→eν, events were triggered by the electron calorimeter only. An energy cluster >10GeV was requested.

Off line, cuts were applied on the longitudinal energy release in the calorimeter cells. A track pointing to the energy cluster was required, and events with jets were rejected.

In the 1983 W discovery run (integrated luminosity L=0,136 pb^{-1}), 55 events were left having a high quality electron signature in the calorimeter.

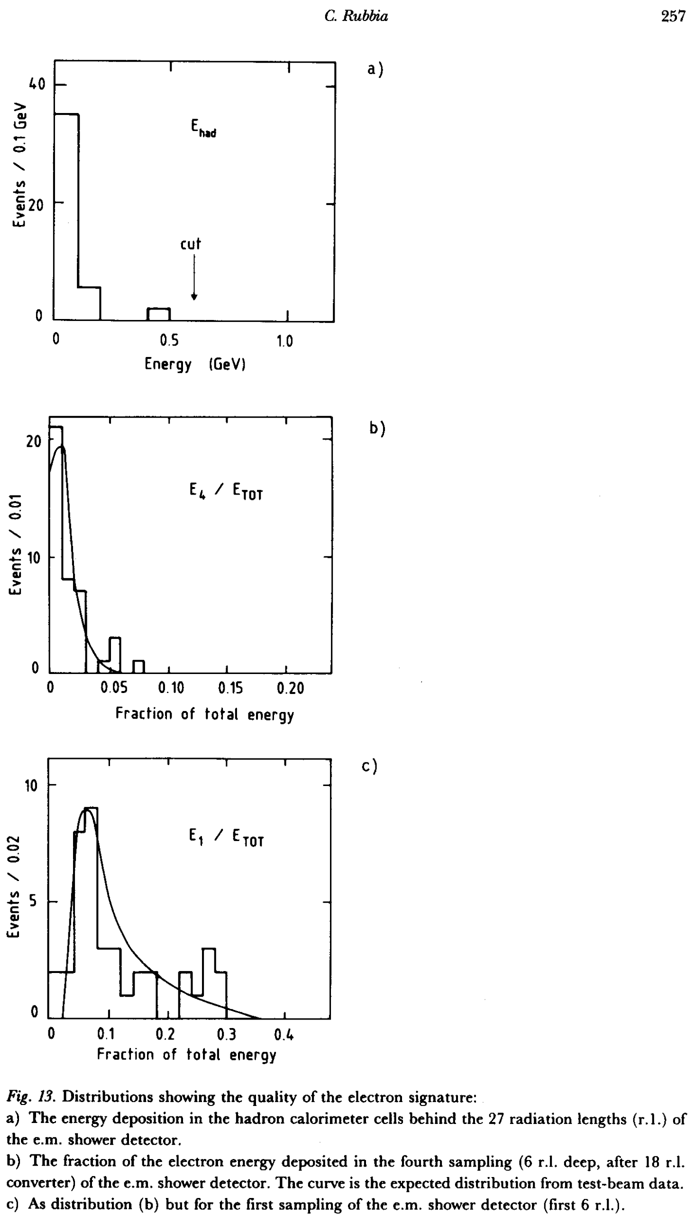
C. Rubbia 257

Fig. 13. **Distributions showing the quality of the electron signature:**
a) The energy deposition in the hadron calorimeter cells behind the 27 radiation lengths (r.l.) of the e.m. shower detector.
b) The fraction of the electron energy deposited in the fourth sampling (6 r.l. deep, after 18 r.l. converter) of the e.m. shower detector. The curve is the expected distribution from test-beam data.
c) As distribution (b) but for the first sampling of the e.m. shower detector (first 6 r.l.).

ELECTRON AND NEUTRINO JACOBIAN PEAKS

In the W$^+$ rest frame the decay angular distribution of the e$^+$ vanishes in the direction opposite to the W$^+$ helicity:

$$\frac{d\sigma}{d\cos\theta^*} \propto \left(1+\cos\theta^*\right)^2$$

254 **Weak Boson Production and Decay**

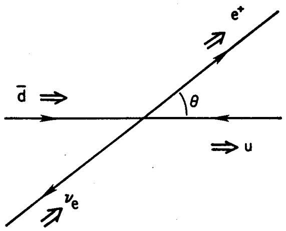

Fig. 8.8. Subprocess for $W^+ \to e^+\nu$ in W rest-frame. Arrows denote momenta, double arrows denote helicities.

$p_t = (M_W/2)\sin\theta^*$ not measurable as such, but $p_t = p\sin\theta$ can be measured in the lab.

Neglecting the transverse momenta of the u and $\bar{\text{d}}$ quarks, the electron (or neutrino) p_t in the lab is the same as in the c.m. of the W. The angular cross section can be transformed into a p_t cross section

$$\frac{dn}{dp_t} = \frac{dn}{d\cos\vartheta^*}\,\frac{d\cos\vartheta^*}{dp_t}, \quad \cos\vartheta^* = \sqrt{1-\sin^2\vartheta^*} = \sqrt{1-\left(\frac{2p_t}{M_W}\right)^2}$$

$$\left|\frac{d\cos\vartheta^*}{dp_t}\right| = \frac{4\dfrac{p_t}{M_W^{\,2}}}{\sqrt{1-\dfrac{4p_t^{\,2}}{M_W^{\,2}}}}$$

which has a divergence (“Jacobian peak”) at $p_t = \sqrt{s}/2 \sim m_W/2$.

TRANSVERSE MASS

The W jacobian peak is smeared by the non-zero transverse momentum of the initial state quark pair. A parameter that shows a peak close to the W mass and which is insensitive to the W transverse momentum is the "transverse mass" of the neutrino and the electron. Neglecting the e, ν masses

$$m_t^{\,2} = \left(E_{e,t} + E_{\nu,t}\right)^2 - \left(\vec{E}_{e,t} + \vec{E}_{\nu,t}\right)^2 = 2\,p_t^{\,e}\,p_t^{\,\nu}\left(1-\cos\phi_{\nu e}\right) = 4\,p_t^{\,e}\,p_t^{\,\nu}\sin^2\frac{\phi_{\nu e}}{2}$$

where ϕ is the angle between the electron and the missing p_t in the plane transverse to the beams. A transverse boost of the W with velocity β leaves m_t unchanged up to β^2 terms.

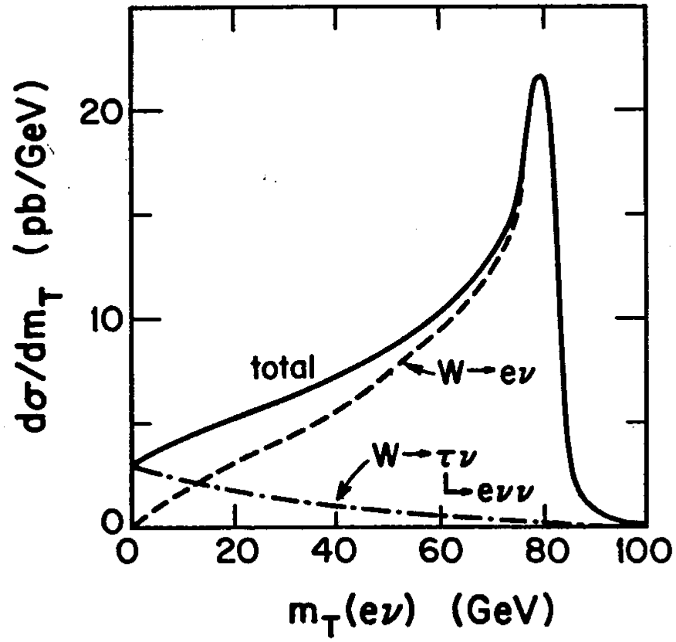

Fig. 8.11. Predicte distribution of transverse mass $m_T(e\nu$ for $p\bar{p} \to W^{\pm} \to e$ collisions at $\sqrt{s} = 63$ GeV.

The transverse mass distribution is strongly peaked near the W mass. However, the finite missing E_t resolution of the experiment causes a significant spread.

Calibration errors, calorimeter imperfections, finite calorimeter resolution create an apparent $\vec{E}_{miss}$ even if there are no neutrinos. The $\vec{E}_{miss}$ resolution can be measured by studying its distribution in soft inclusive events or in events with two exclusive jets.

Because of the large fluctuations of the energy loss around the beams the energy vector imbalance is studied only on the transverse plane.

At UA1 the transverse energy resolution was found to grow with the total scalar transverse energy flow:

$$\sigma(\Delta E_x) = 0{,}41\sqrt{\sum_i \left|E_t^i\right| (GeV)}$$

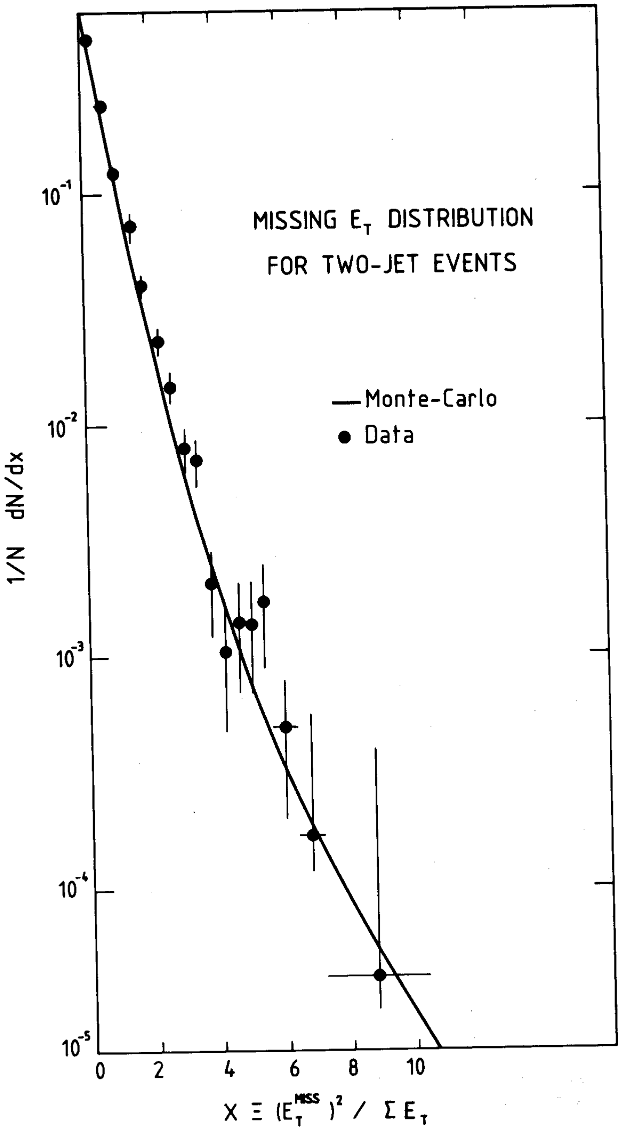

Fig. 12. Transverse energy balance observed for a sample of two-jet events. To convert the horizontal scale to the number of standard deviations (n), use the relationship $n^2 \approx 2x$. Variables have been chosen in such a way as to transform a Gaussian basic response of the calorimeters into a linear plot. The continuous line is the result of a calculation based on the expected calorimeter responses, as measured with test-beam particles.

A clear jacobian peak was seen by UA1 in the missing E_t spectrum.

52 out of the 55 events with good large E_t electrons passed the cut $E_{t,miss}>15$ GeV.

258 *Physics 1984*

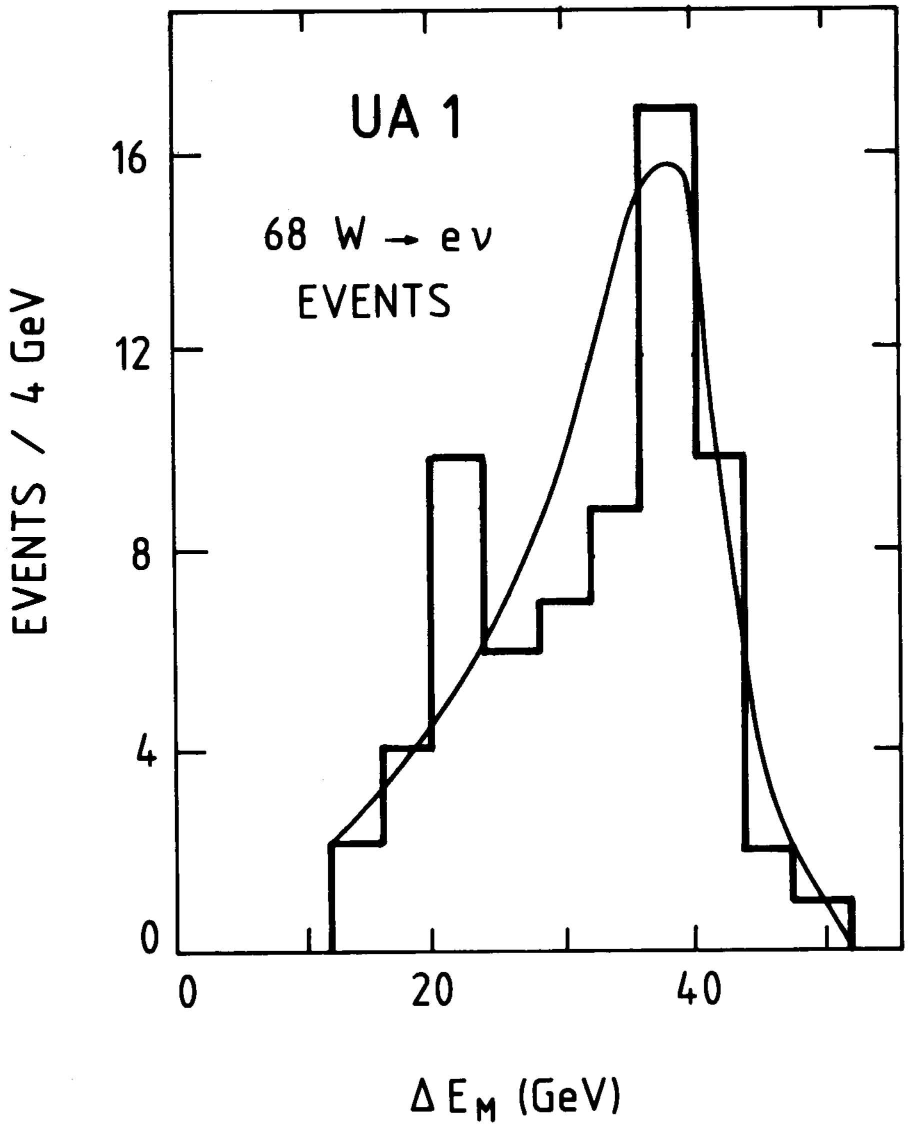

Fig. 14. The distribution of the missing transverse energy for those events in which there is a single electron with $E_T>15$ GeV, and no coplanar jet activity. The curve represents the resolution function for no missing energy normalized to the three lowest missing-energy events.

A jacobian peak was seen in the electron transverse energy spectrum.

A cut requiring the electrons to hit the calorimeter cells more than 15 cm away from edges accepted 43 events.

Montecarlo simulation showed that the electron E_t distribution was incompatible with the hypothesis that neutrinos were 2 rather than 1.

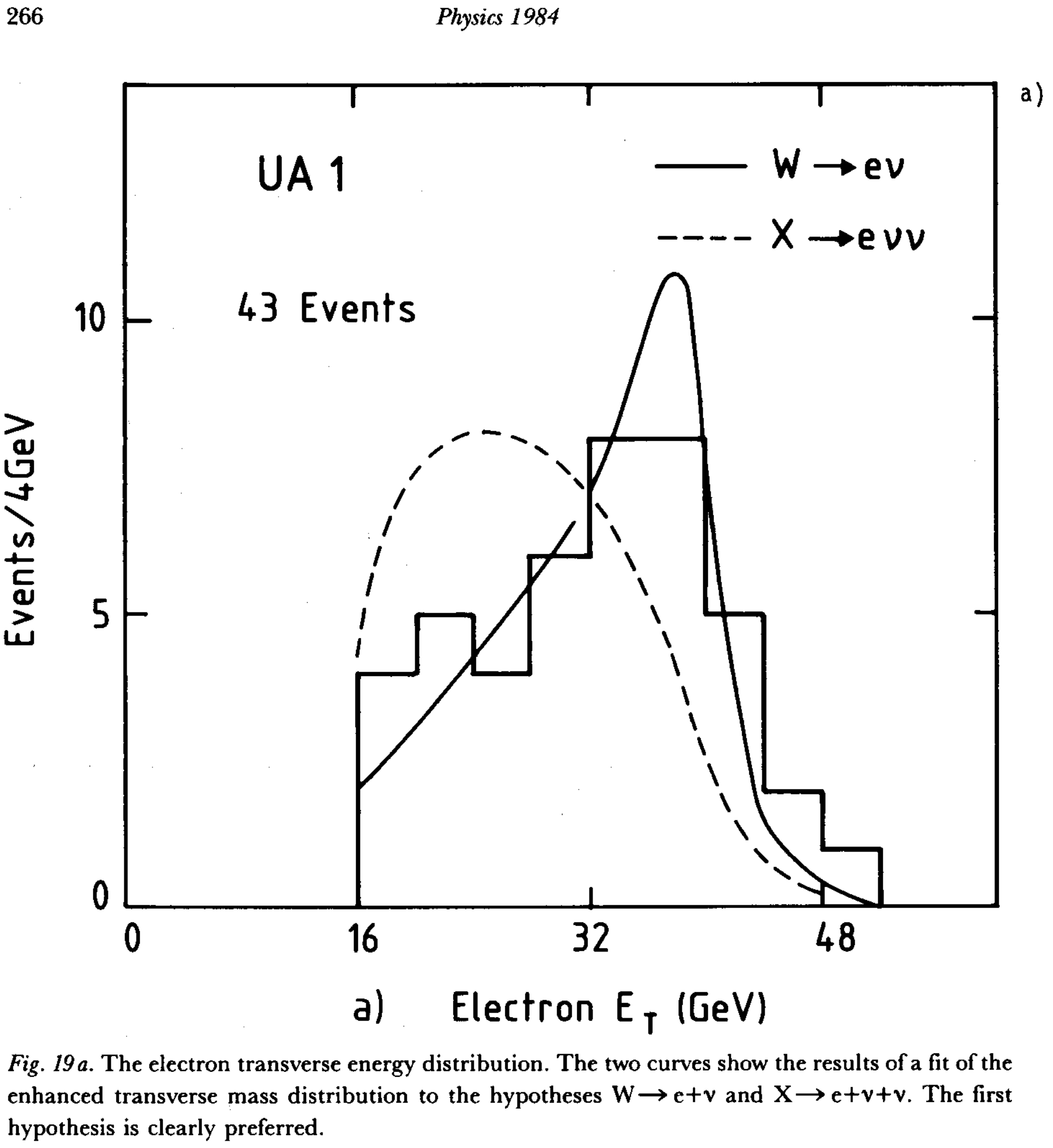

266 Physics 1984

Fig. 19a. The electron transverse energy distribution. The two curves show the results of a fit of the enhanced transverse mass distribution to the hypotheses W→e+ν and X→e+ν+ν. The first hypothesis is clearly preferred.

The electron energy was roughly proportional to the missing energy.

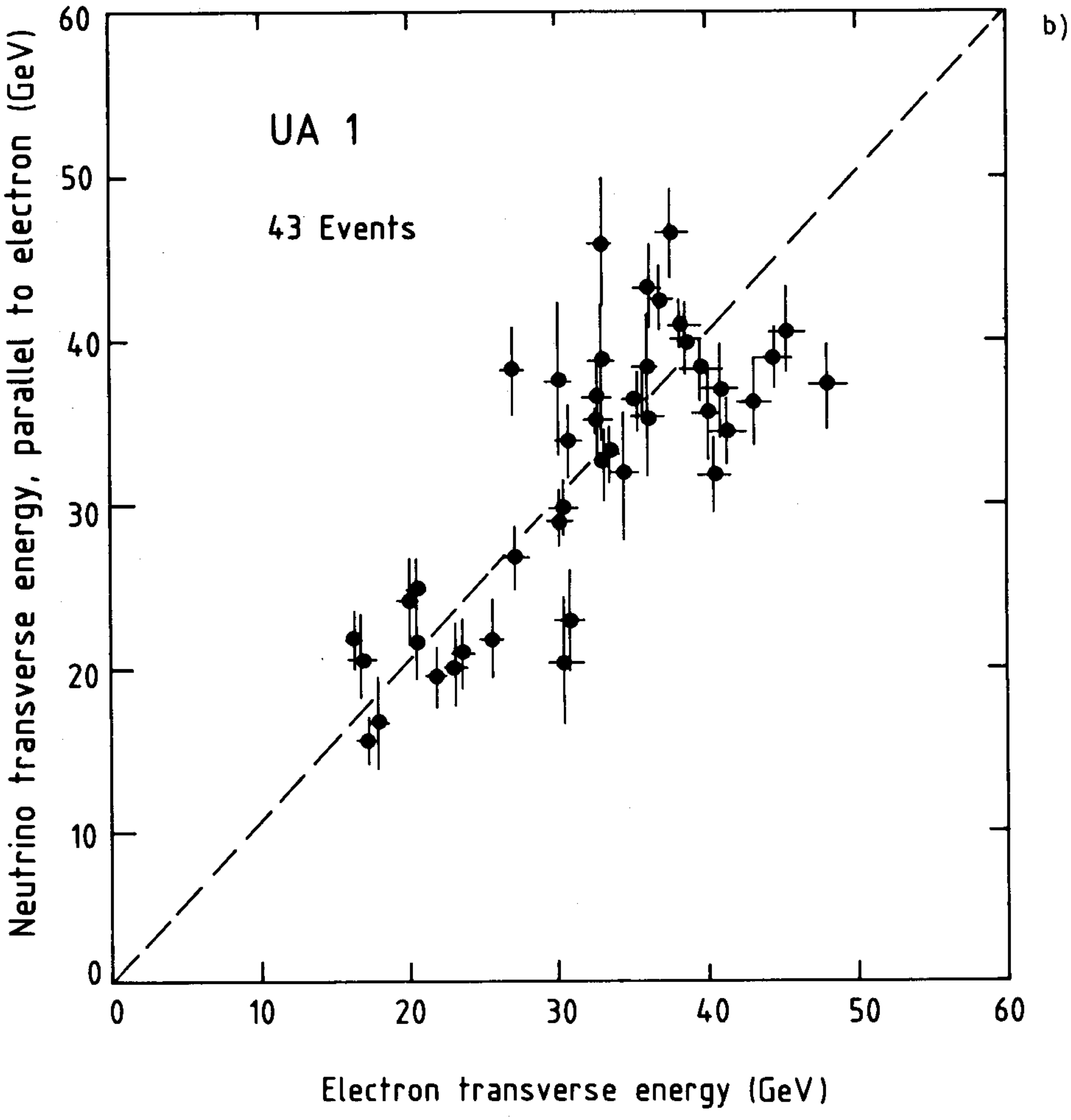

Fig. 17b. Correlation between the electron and neutrino transverse energies. The neutrino component along the electron direction is plotted against the electron transverse energy.

The azimuthal angle of the electron (rotated to be aligned along the y-axis in the figure) differed by π from the azimuthal angle of $\vec{E}_{t,miss}$.

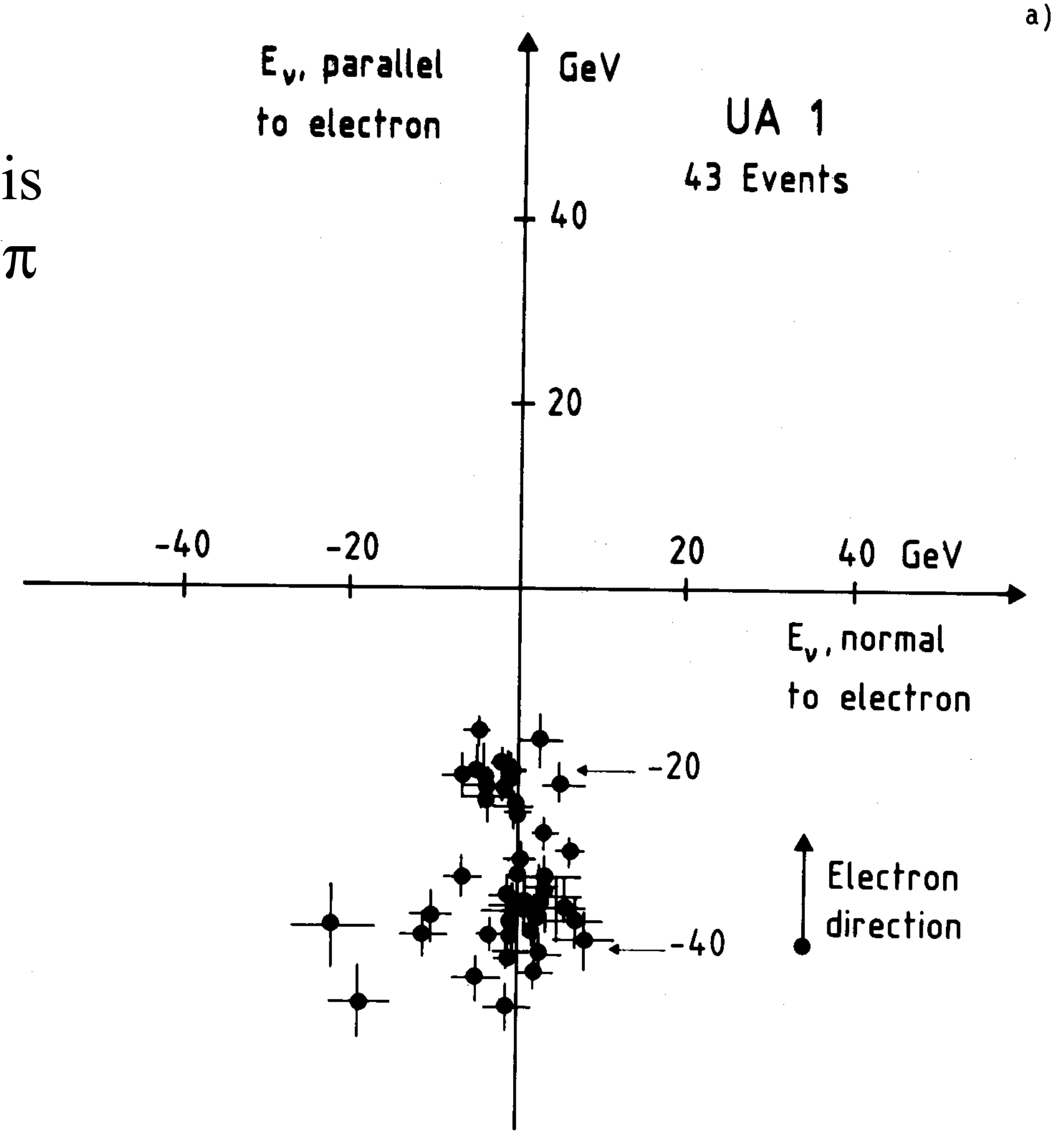

Fig. 17a. Two-dimensional plot of the transverse components of the missing energy (neutrino momentum). Events have been rotated to bring the electron direction to point along the vertical axis. The striking back-to-back configuration of the electron–neutrino system is apparent.

The neutrino and electron jacobian peaks in the final UA1 W data.

338 *G. Salvini and A. Silverman, Physics with matter–antimatter colliders*

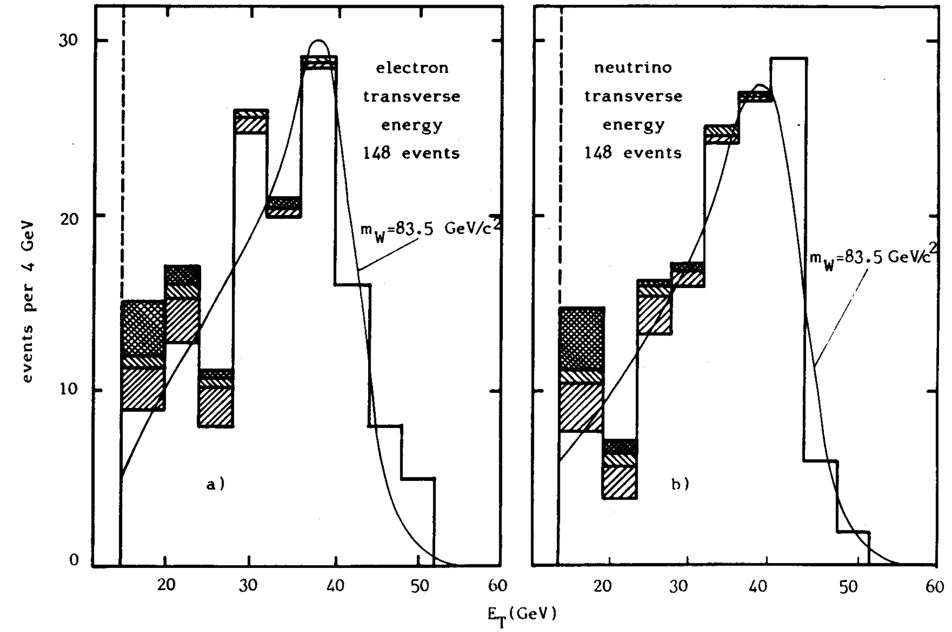

Fig. 3.5. The lepton transverse energy distributions for the UA1 sample of well-measured $W^{\pm} \to e^{\pm}\nu_e$ events, (a) the electron transverse energy distribution and (b) the neutrino transverse energy distribution. The shaded parts show the expected contributions from jet–jet fluctuations (cross-hatched) and $W \to \tau\nu$ decays with $\tau \to$ hadrons (top left to bottom right hatching) and $\tau \to e\nu_e\nu_\tau$ (top right to bottom left hatching). The curves show the predictions for the background subtracted distributions (normalized to the data) corresponding to W with a mass of 83.5 GeV/c^2. Transverse energy and transverse momentum are in this case equivalent expressions (UA1 [21]).

G.Salvini and A. Silverman, Physics Reports 171,n.5,6 (1983),231.

LEPTON ASYMMETRY IN W DECAY

V-A interaction selects left-handed u-quarks, and thus polarizes the W^+ in the direction opposite to the incoming u-quark, i.e. along the antiproton. The opposite is true for the W^-, and the W^- spin is aligned along the proton beam. Thus a distribution like $(1+\cos^2\theta)$ relative to the proton beam is expected for the W^- decay electrons in the W^- rest frame.

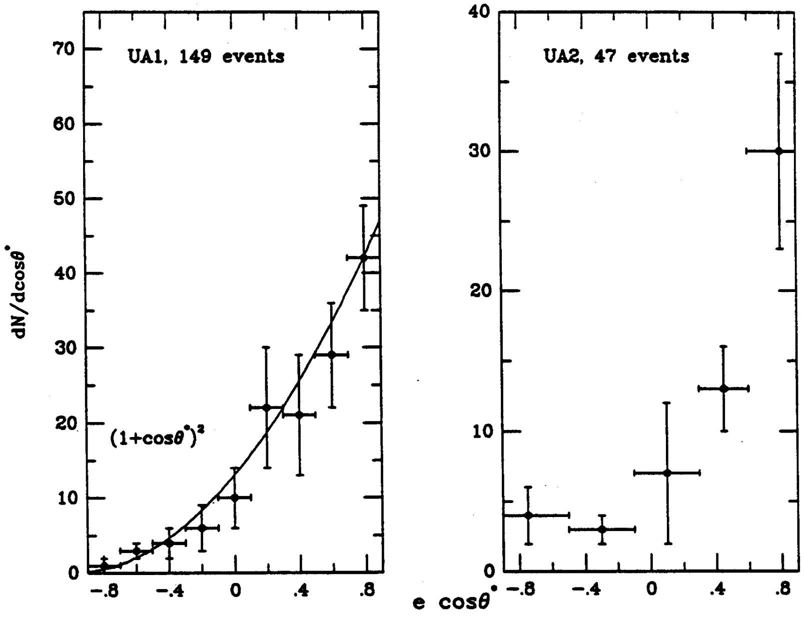

Figure 40: Angular distribution of leptons from W-boson decay.

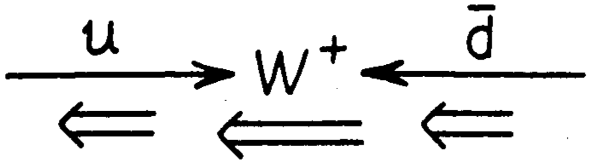

Figure 10.4
Polarized W^+ produced in a $p\bar{p}$ collider.

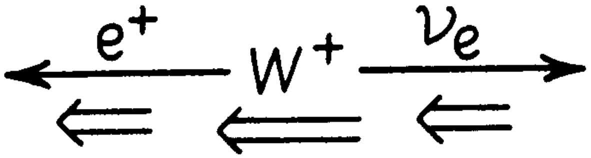

Figure 10.5
Spin configuration of W decay.

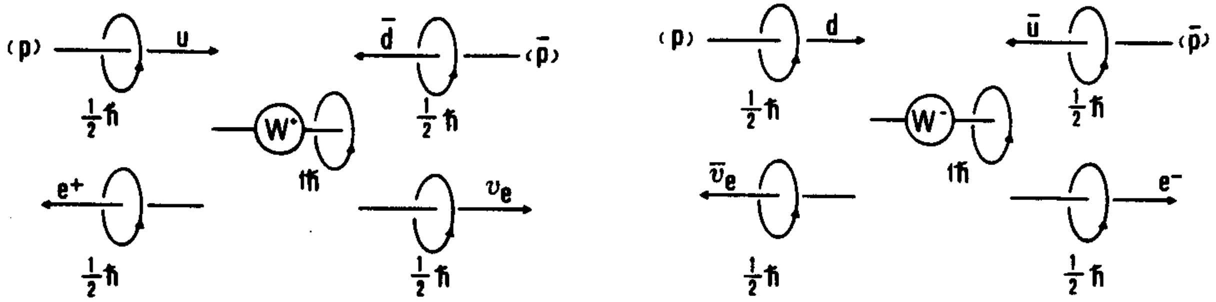

Fig. 3.12. Production and decay of W^+ and W^- showing the spin orientation of the particles. For example, the W^+ is formed from a left-handed quark (proton) and a right-handed antiquark (antiproton). It decays to a right-handed e^+ and left-handed ν_e, which are constrained to travel in the directions shown to conserve angular momentum, giving rise to a $(1 + \cos\theta^*)^2$ angular distribution. (Taken from Dowell [36]).

EVIDENCE FOR A NEUTRAL WEAK PROPAGATOR

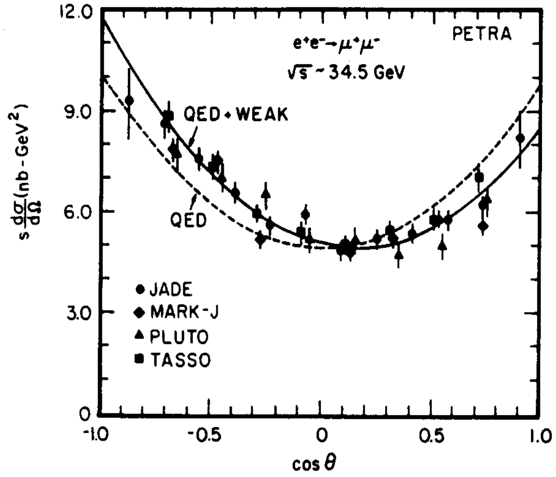

Fig. 2.61. Compilation of the PETRA measurements for the angular distribution of $e^+e^- \to \mu^+\mu^-$ at 34.5 GeV center of mass energy. The full curve is a fit to the data allowing for an asymmetry. The dashed curve is for the symmetric QED prediction after correcting for a small asymmetry from α^3 diagrams [20].

The ratio of the Z to the γ annihilation amplitudes grows with energy and peaks at $\sqrt{s} = M_Z$. Away from the resonance, the interference between the e, μ vector couplings to γ and Z, and their axial-vector coupling to Z generates a F-B asymmetry, $A_{\mu\mu} = (N_F - N_B)/(N_F + N_B)$ which is proportional to the axial-vector couplings of the Z:

$$\frac{d\sigma_{\mu\mu}}{d\Omega} = \frac{\alpha^2}{4s}\left[c_1\left(1+\cos^2\theta\right)+c_2\cos\theta\right], \quad A_{\mu\mu} \propto c_2 \propto a_e a_\mu$$

At Petra (e^+e^- ,$\sqrt{s} \sim 34$ GeV), $A_{\mu\mu} \sim 1\%$.

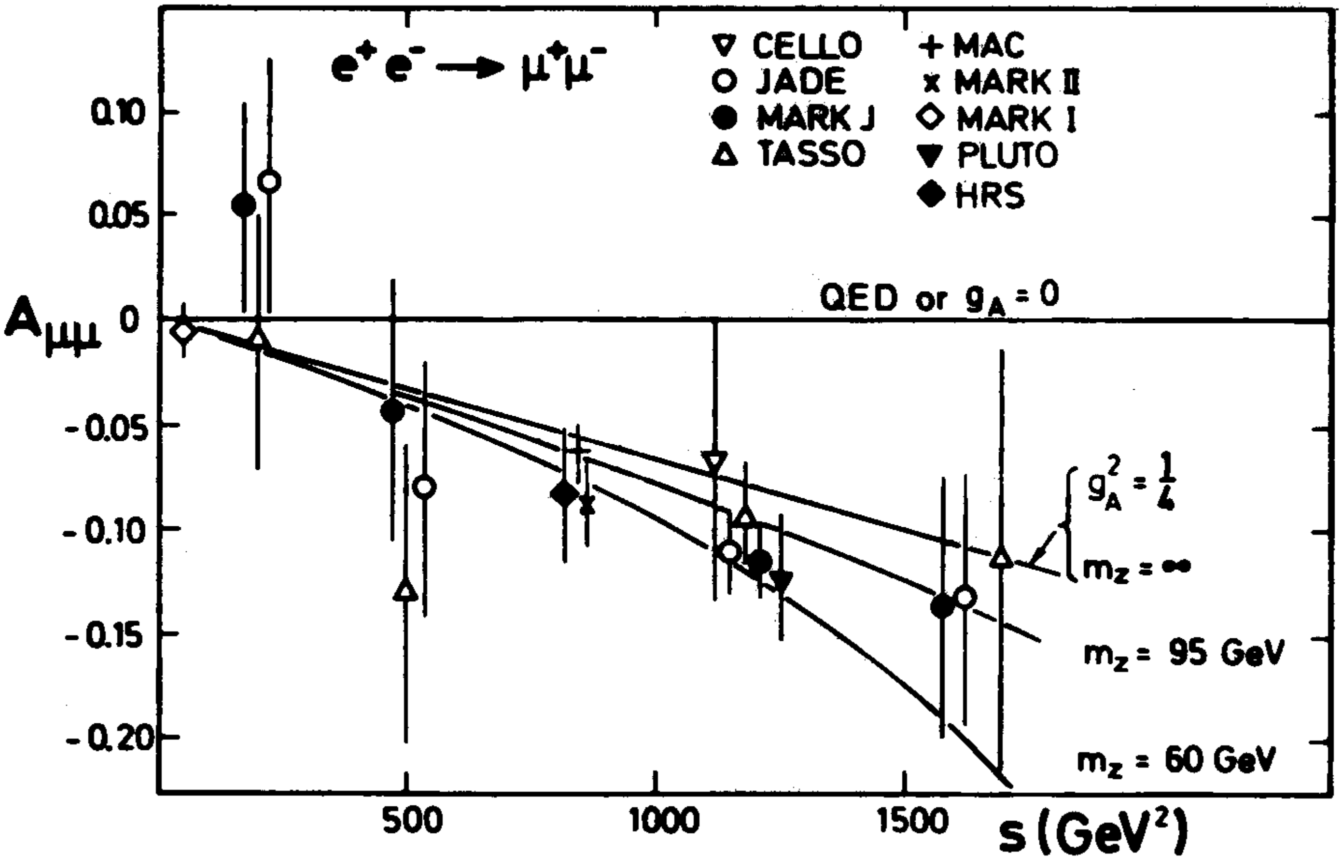

Fig. 23. Experimental evidence for a weak-electromagnetic interference effect in the process $e^+e^- \rightarrow \mu^+\mu^-$ at high-energy colliding beams. It can be seen that data are better fitted if the presence of a finite mass m_Z propagator is assumed.

The energy dependence of the forward-backward asymmetry of muon pairs in e^+e^- annihilation was giving a clear evidence of a contribution by the neutral Z.

The expected Z signature was very clear: **Z → μμ or Z → ee.**

However the Z was discovered second because its rate σB was about 10% of the W rate.

Indeed σ(W)/σ(Z) ~ 3 and B(W→eν) ~ 11% while $B(Z \rightarrow e^+e^-) = B(Z \rightarrow \mu\mu) \sim 3.3\%$.

$Z^0 \longrightarrow e^+e^-$

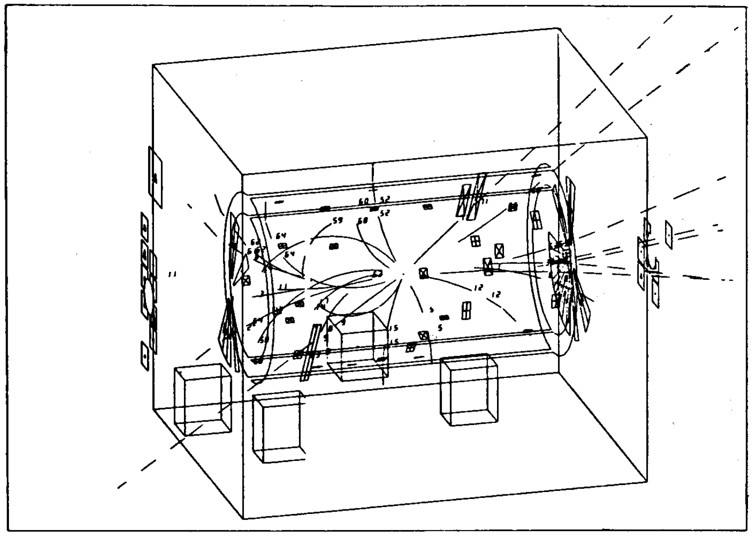

Fig. 25. Event display. All reconstructed vertex-associated tracks and all calorimeter hits are displayed.

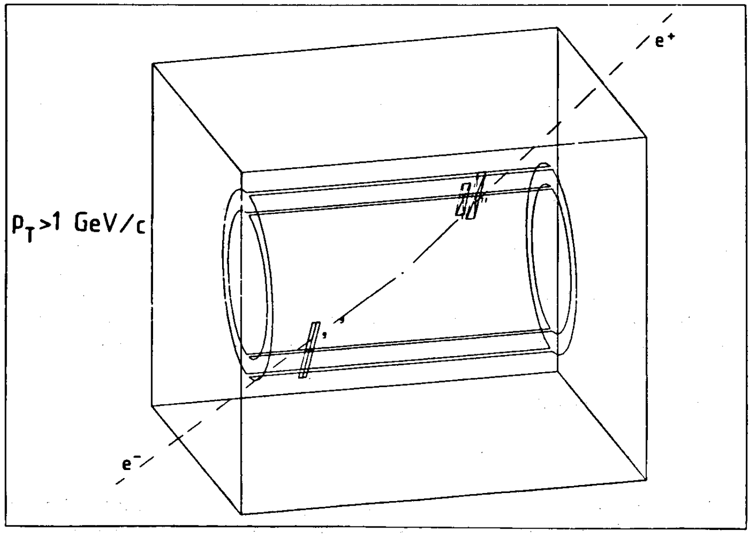

Fig. 26. The same as Fig. 25, but thresholds are raised to p_T>2 GeV/c for charged tracks and E_T>2 GeV for calorimeter hits. We remark that only the electron pair survives these mild cuts.

The calorimeter signals of the four Z→e^+e^- candidates of the first UA1 Z-search. Two large energy clusters in the e.m. calorimeter were searched for, with an isolated track pointing to them.

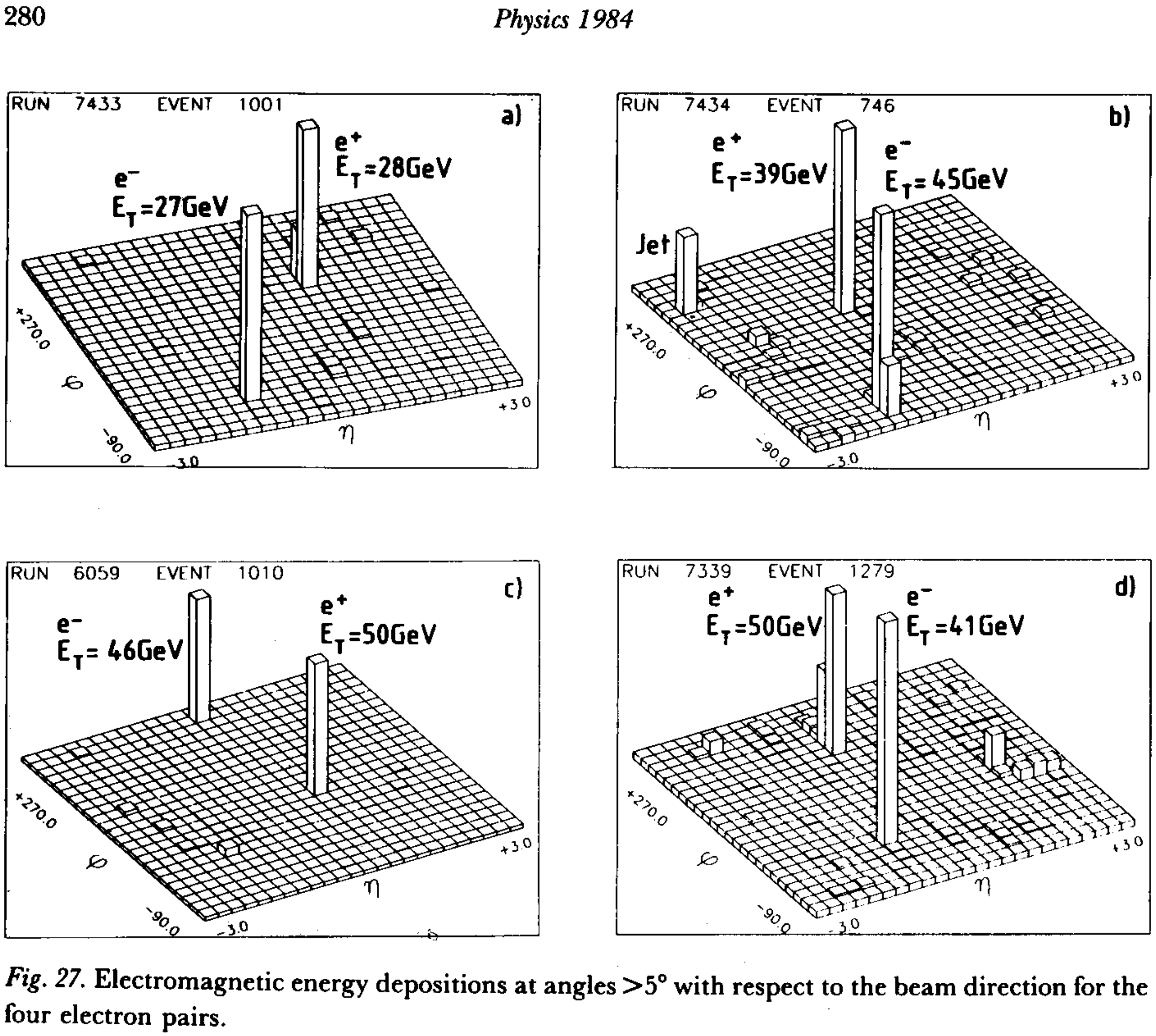

280 *Physics 1984*

Fig. 27. Electromagnetic energy depositions at angles >5° with respect to the beam direction for the four electron pairs.

THE UA2 DETECTOR

The first generation UA2 had magnetic bending in forward toroids, and initially also over a slice of azimuth at 90°. At large angles the solid angle was covered by a e.m. and hadron calorimeters.

The central calorimeter resolution was better than in UA1 in angle as well as in energy, given that it was split into projective towers and that there was no magnet material in front. However, the electron charge was not measured and momentum/energy balance was not available as an electron signature. The electromagnetic nature of a track was certified in the calorimeter only, by its early showering in a tungsten “pre-converter” and by the calorimeter shower shape.

In the firsf year of running about 20% of the azimuth at large angles was not covered by the central calorimeter. Charged particles were momentum analyzed and photons were detected in a matrix of Pb-glass shower counters.

From 1981 to 1985 by UA2 collected 910 nb^{-1}.

e 122B, number 5,6 PHYSICS LETTERS 17 Marc

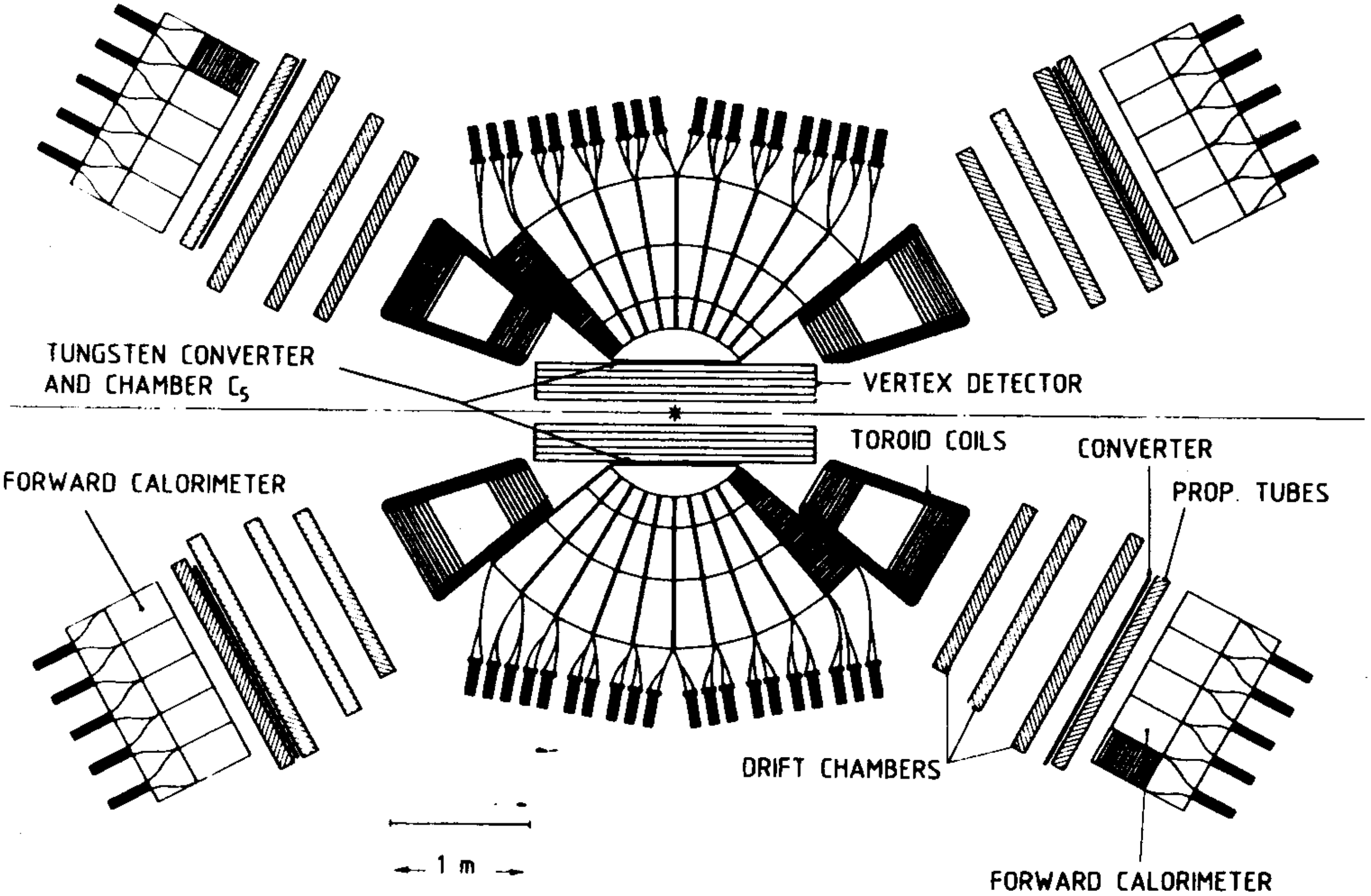

Fig. 1. The UA2 detector: Schematic cross section in the vertical plane containing the beam.

The first generation UA2 detector.
M.Banner et al., Physics Letters 122B, No.5,6, 476 (1983).

Main parameters of the UA2 1st generation detector

2 cylindrical drift chambers and 4 proportional chambers as a vertex detector. The position of the vertex was measured to ±1mm.
A projective tower e.m. and had. calorimeter at large polar angles, extending from θ = 80° to θ = 280° , initially with a missing 60° azimuthal sector. UA2 had no muon detectors.
In the 60° wide magnetic spectrometer at large angles, tracking chambers were followed by a lead-glass array to detect electrons and photons. After one year of operation this spectrometer was removed and the calorimeter coverage at large angles was completed.

Between 20° and ~38° from the beams (the region where the e+, e^- W decay is asymmetry is maximum) two rings of 12 toroidal magnets bent the charged particles radially, backed by telescope drift chamber telescopes. Ext electrons were converted in a Pb-sheet and the start of their showers was viewed by an array of proportional tubes. The forward detector ended with a matrix of Pb-glass e. m. calorimeters.

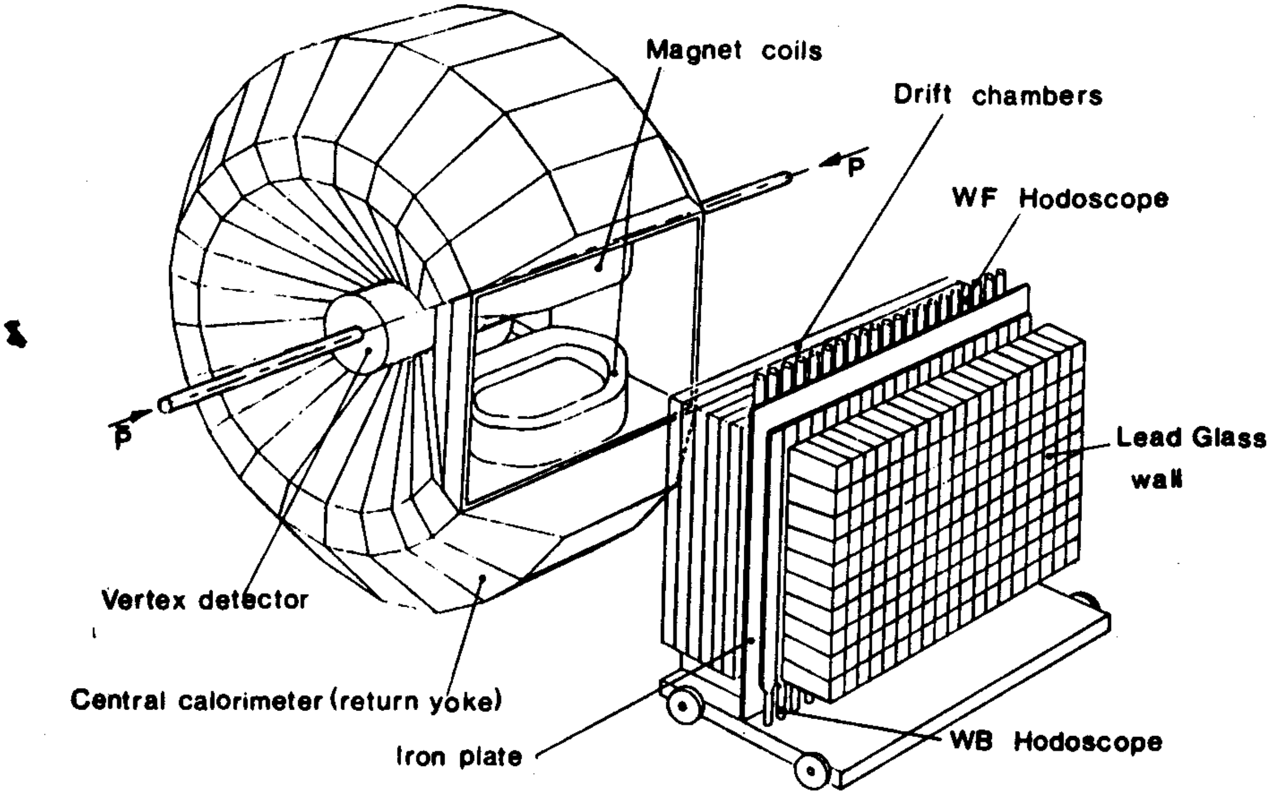

Fig. 2 : Perspective view showing the central calorimeter and the wedge detector.

In winter 1982 the central spectrometer was removed and the central calorimeter was completed.

B.Mansoulie, Proc. of the Third Moriond Workshop, 1983, p. 609.

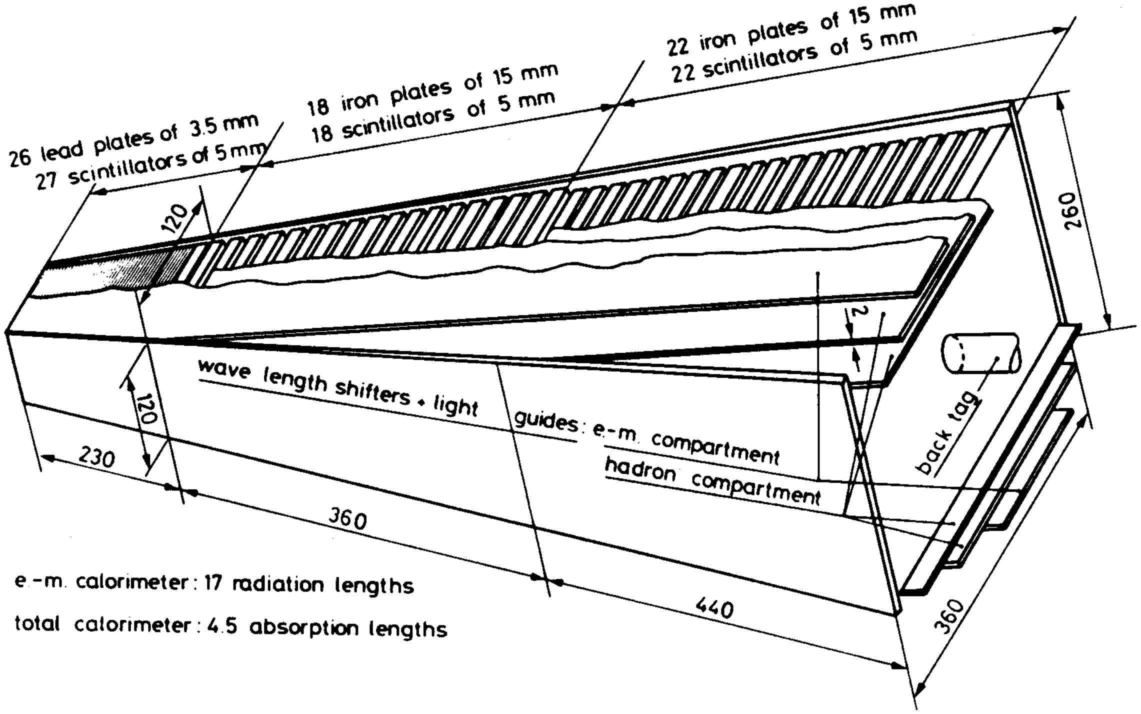

Fig. 6 : Central calorimeter cell.

In the central calorimeter 24 “orange slices” covered the entire azimuth. Each slice contained 10 polar cells of projective geometry as the one shown. The cells had 3 compartments:

- the 17 X_o thick e.m. calorimeter, by a Pb-scintillator sandwich;
- 2 hadron the calorimeter compartments, by Fe-scintillator sandwiches. In totlal the calorimeter was 4,5 λ thick.

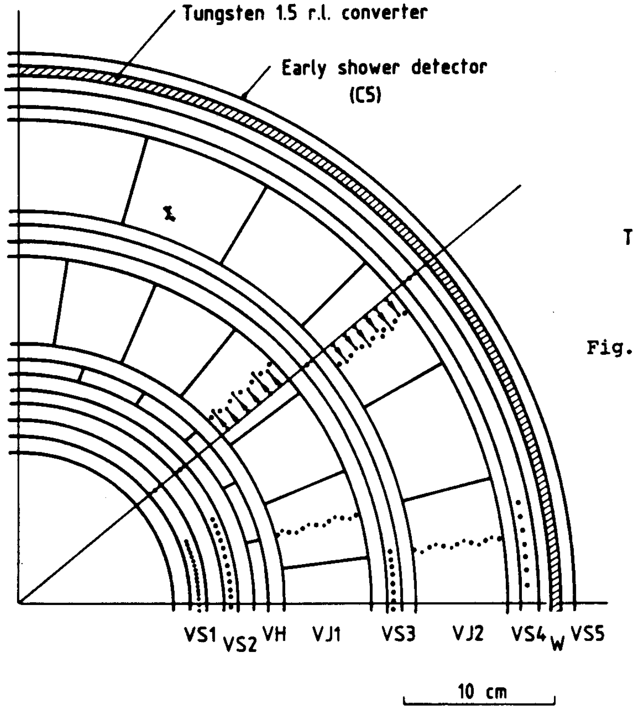

TRANSVERSE VIEW OF VERTEX DETECTOR

Fig. 3 : Small arrows indicate the path of electrons issued from an ionizing track and drifting to the wires in 'JADE' chambers.

VJ1 and VJ2 are “jet chambers” with multiple wire planes housed in the same gas volume (300 μm overall resolution). The longitudinal coordinate is measured by charge division at the ends of the resistive sense wires (with resolution 1% of the wire length).
Five proportional “strip chambers” and a barrel of trigger scintillators complete the vertex detector. An outer proportional chamber behind a 1,5 mm tungsten converter signals electrons.

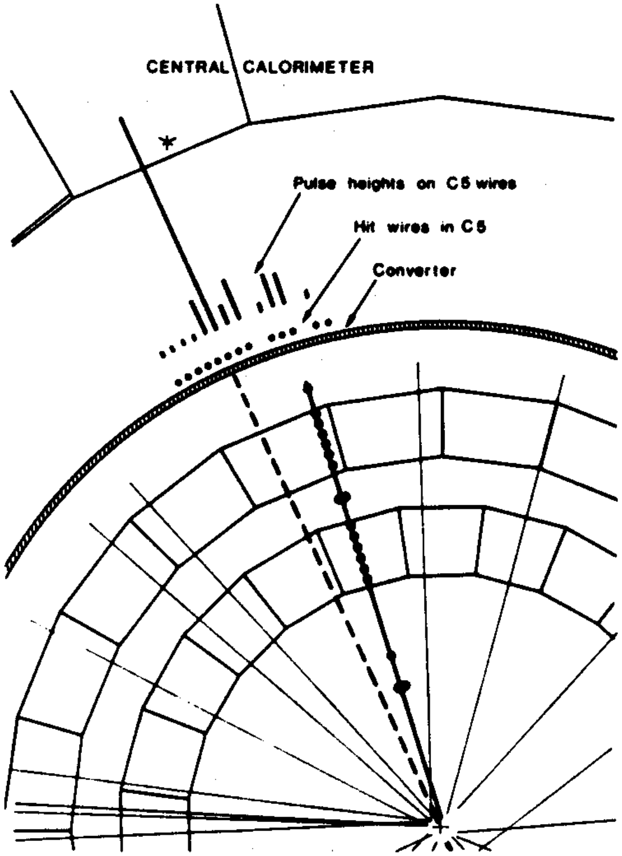

Fig. 5 : Transverse view of an "overlap" background event.

A typical background overlap event simulating an electron in the W search. It can be recognized as such because the pulse heights in the C5 chamber (3,5 mm resolution in both directions) behind the converter are not well aligned with the incoming charged track.

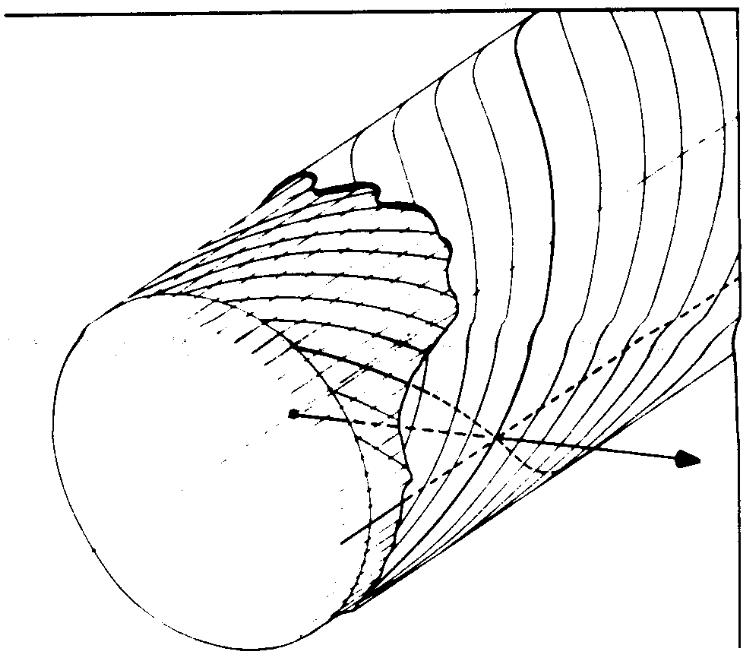

Fig. 4 : Schematic view of a strip chamber. Only one wire out of ten and one strip out of ten are drawn for simplicity. The arrowed line is a track coming from the beam line. Hit strips and wire are in thick.

In the proportional “strip” chambers the cathode signal was read out on a double layered plane of helical strips, oriented locally orthogonal to each other.

The overall vertex finding efficiency was 97%. The longitudinal position of the vertex was measured with ± 1,5 mm resolution.

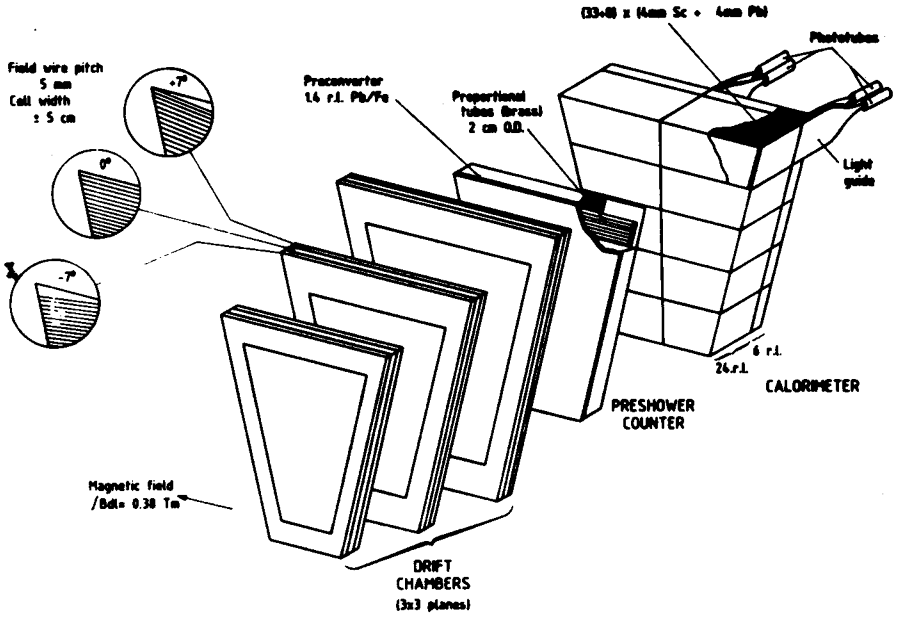

Fig. 10 : Forward-Backward detector : exploded wiew of one sector.

In the toroidal spectrometers the direction of the exiting tracks was measured by 3 drift chamber sandwiches of 3 planes each. In a sandwich, wires were aligned along the magnetic field and at ±7° with respect to it. The momentum resolution was $\Delta p/p^2 \sim 1\%$. Behind the chambers a $1{,}5X_0$ converter initiates e.m.showers which are detected by a 4-layered sandwich of proportional tube planes. Finally, electrons and photons are absorbed in a matrix of 24 X_0 thick Pb-glass cells backed by $4X_0$ thick hadron veto.

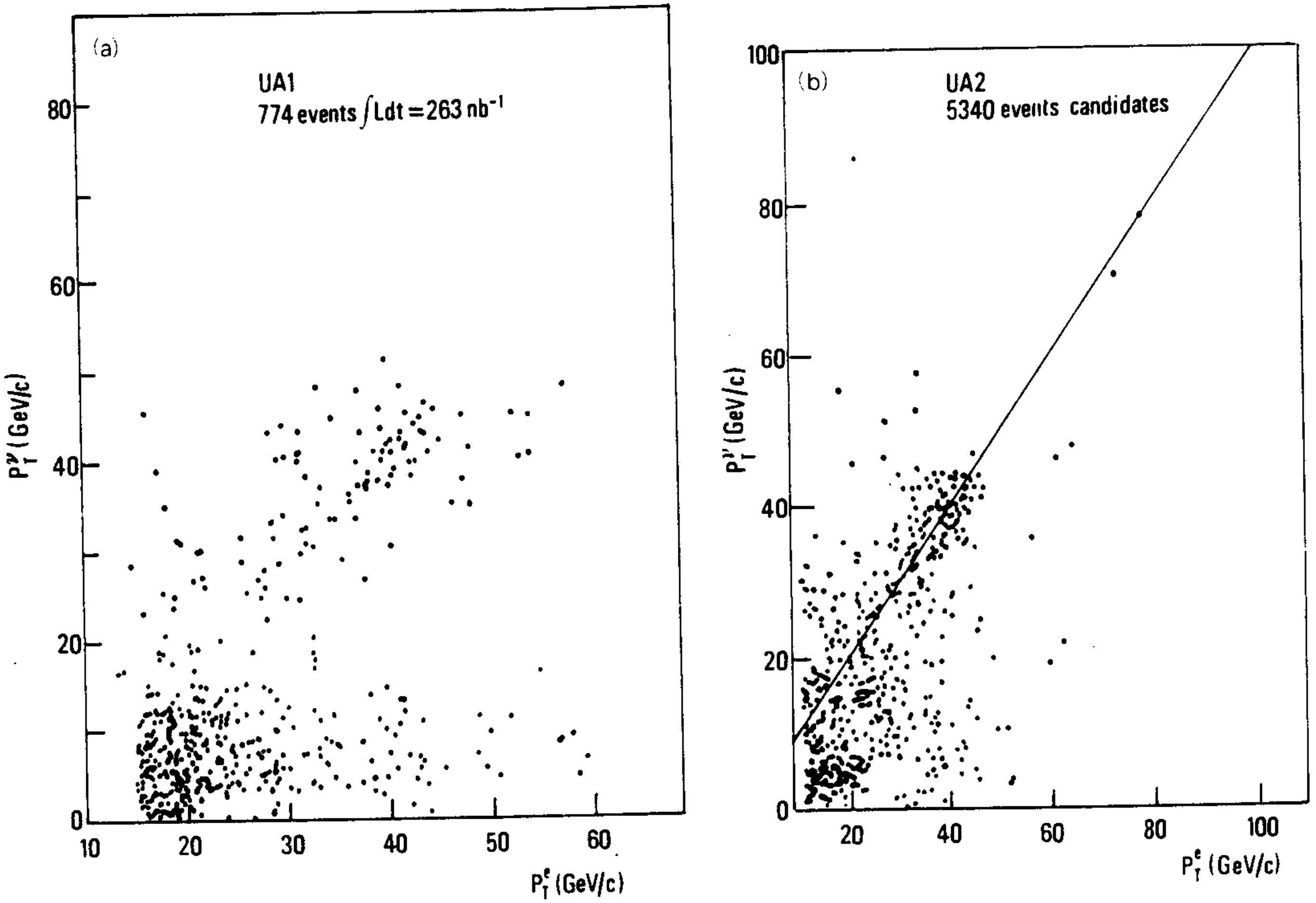

Fig. 3.4. Transverse momentum P_T^ν versus P_T^e: scatter plots of (a) UA1 and (b) UA2 [21, 22].

Because of the limited coverage of the central calorimeter, the missing transverse energy resolution of UA2 was less good than in UA1. However, a sufficient separation of the W electrons in the $E_{t,electron} - E_{t,miss}$ plane was reached..

The UA2 transverse mass plot also indicated a very clear W peak.

As in UA1, the W mass was determined by fitting this spectrum to a sum of Monte Carlo simulated templates, one to represent background and one to represent a mass-dependent W peak.

344 *G. Salvini and A. Silverman, Physics with matter–antimatter colliders*

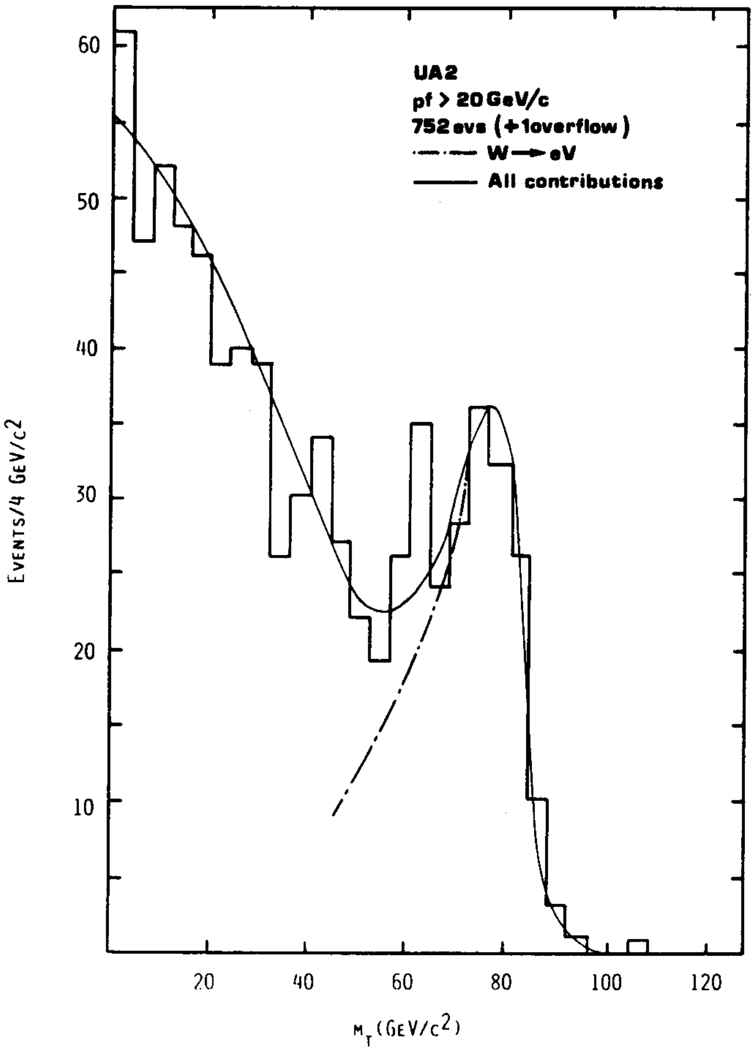

Fig. 3.8. The M_T distribution of the W according to UA2 [22] (decay W→ eν). Notice the fast decrease after 80 GeV/c^2. The different cuts explain the difference between figs. 3.7a and 3.8.

Dilepton mass of
the first Z events
in UA1 and UA2.

$$m = 4E_1E_2\sin^2\frac{\alpha}{2},$$

$$\frac{\delta m_Z}{m_Z} = \frac{1}{2}\sqrt{\left(\frac{\delta E_1}{E_1}\right)^2 + \left(\frac{\delta E_2}{E_2}\right)^2 + \left(\frac{\delta\alpha}{\tan\frac{\alpha}{2}}\right)^2}$$

The error is dominated by the errors on the absolute energies. This is Particularly true in the muon channel.

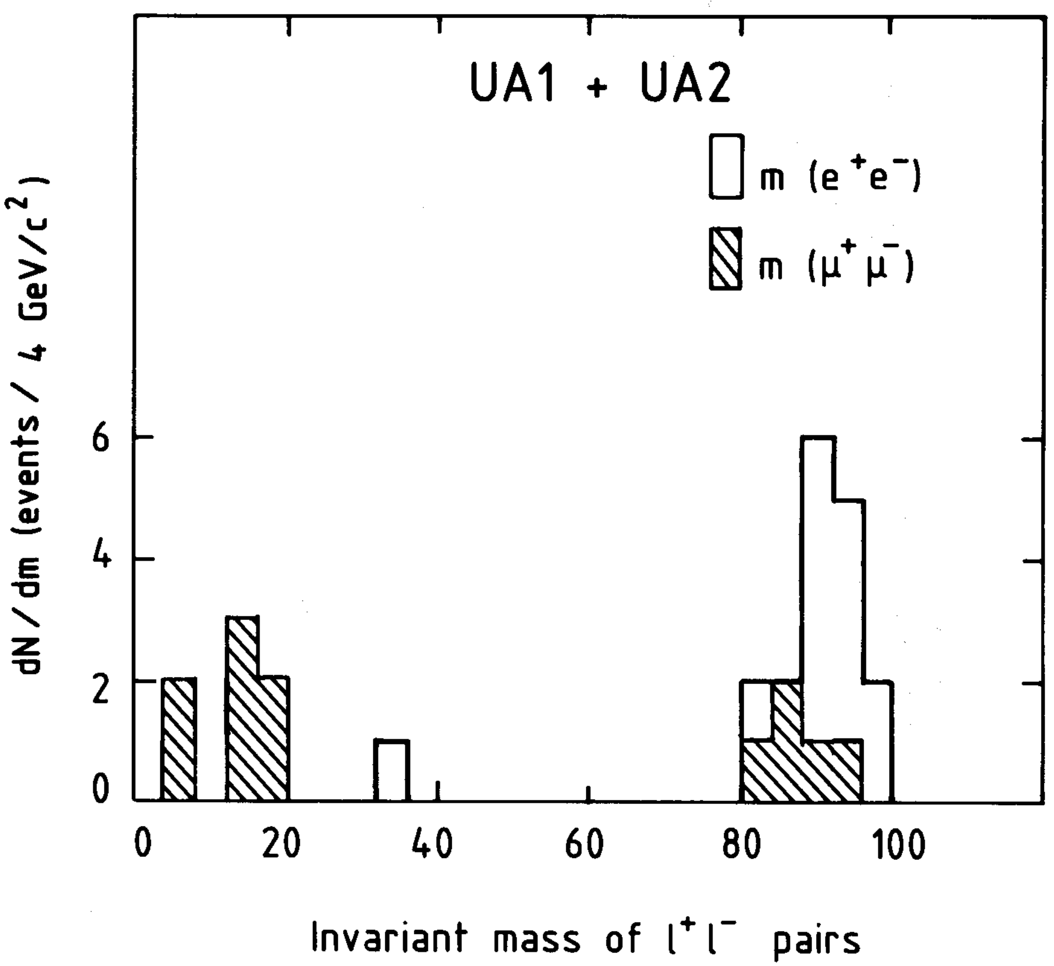

Fig. 29. Invariant mass distribution of dilepton events from UA1 and UA2 experiments. A clear peak is visible at a mass of about 95 GeV/c^2.

The 1987 W, Z masses in the electron channel:

UA2:
m_W = 80.2 +-0.6(stat.) +-1.4(syst.) GeV
m_Z = 91.5 +-1.2 +-1.7

UA1:
m_W = 82.7 +-1.0 +- 2.7
m_Z = 93.1 +-1.0 +- 3.1.

The larger UA1 systematic error reflect the difficult calorimeter calibration.

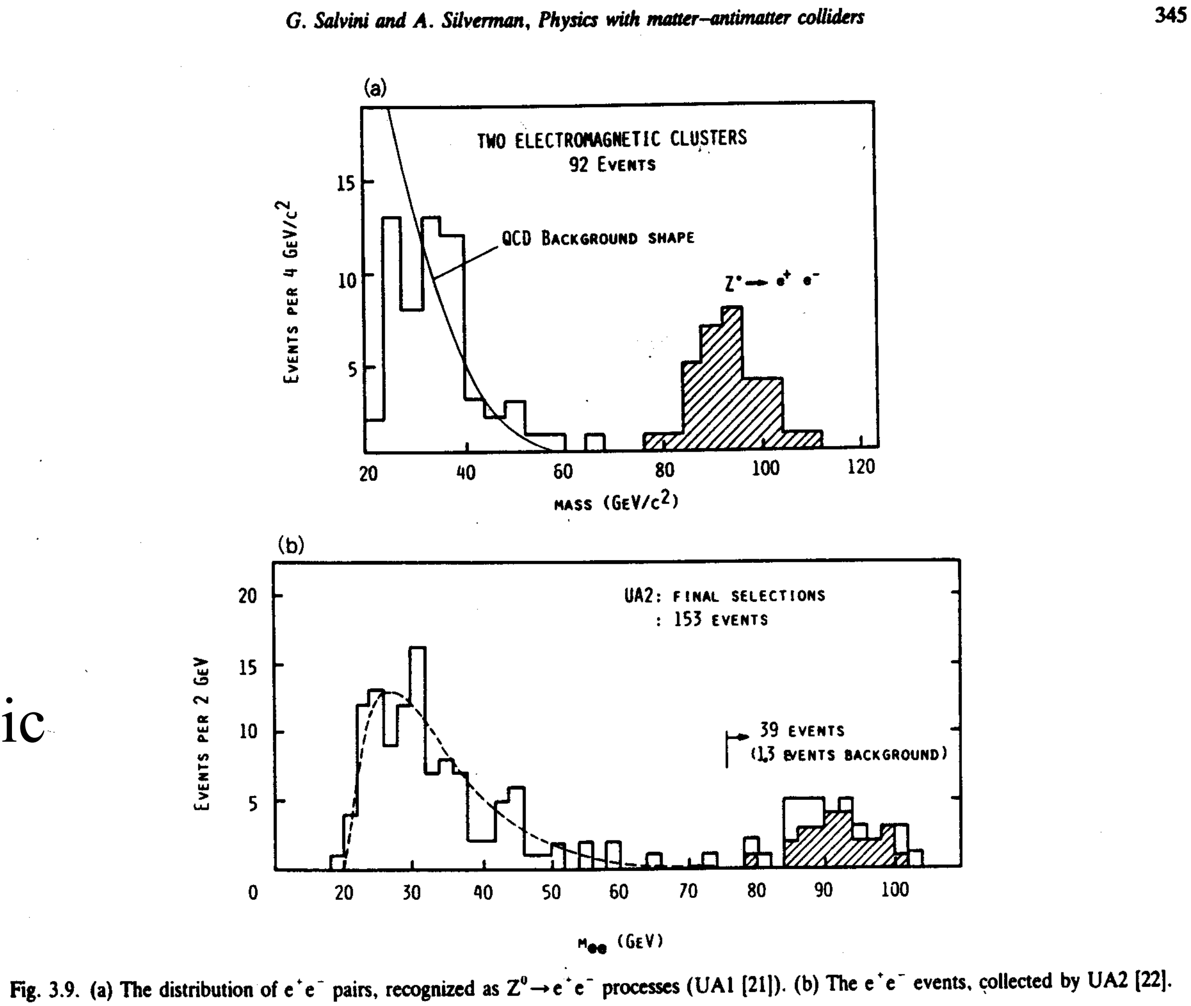

G. Salvini and A. Silverman, Physics with matter–antimatter colliders 345

Fig. 3.9. (a) The distribution of e^+e^- pairs, recognized as $Z^0 \to e^+e^-$ processes (UA1 [21]). (b) The e^+e^- events, collected by UA2 [22].

WHY IS THE MEASUREMENT OF M_W SO IMPORTANT

Radiative Corrections to the W Mass

⋆ $M_W = \frac{A}{\sin\Theta_W\sqrt{1-\Delta R}}$ where $A = \left(\frac{\pi\alpha}{\sqrt{2}G_F}\right)^{\frac{1}{2}}$

⋆ $\Delta R \sim \left(\frac{M_{Top}}{M_W}\right)^2, \ln\frac{M_H}{M_W}$

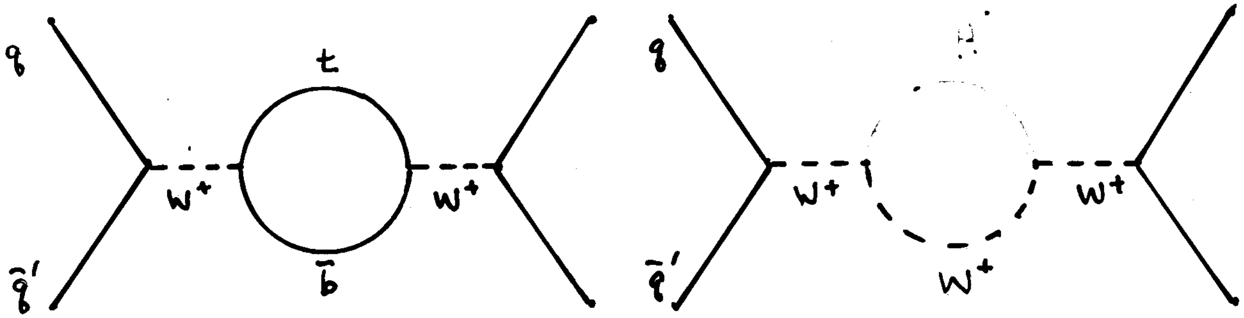

Within the Standard Model an accurate measurement of M_W measures of the sum of contributions by top quark exchange loops and by Higgs boson loops, and allows to constrain the top and the Higgs masses.

THE Z WIDTH AND THE NUMBER OF NEUTRINO SPECIES

The experimental measurement of the ratio R of the W→eν and the Z→ee rates was used at the SpS for an indirect but reliable measurement of the ratio of the W,Z total widths.

$$R = \frac{\sigma_W Br(W \rightarrow e\nu)}{\sigma_Z Br(Z \rightarrow ee)} = \frac{\sigma_W}{\sigma_Z} \frac{\Gamma_Z}{\Gamma_Z{}^{ee}} \frac{\Gamma_W{}^{e\nu}}{\Gamma_W}$$

$$\frac{\Gamma_Z}{\Gamma_W} = R \frac{\sigma_Z}{\sigma_W} \frac{\Gamma_Z{}^{ee}}{\Gamma_W{}^{e\nu}}$$

The production cross section ratio can be computed reliably in QCD. The partial decay widths Γ(W→eν) and Γ(Z→ee) can be accurately computed in the Standard Model. The only unknown is the ratio of the total widths.

UA1 and UA2 compared the experimental Γ_W/Γ_Z ratio to expectations as a function of the number of light neutrinos and of the top quark mass.

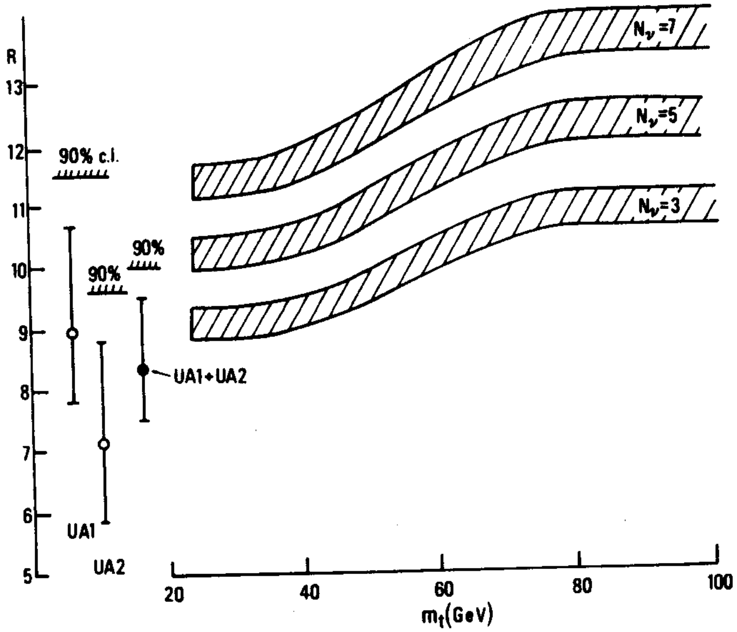

Fig. 3.15. The ratio $R = \sigma_W \, Br(W \to e\nu)/\sigma_Z \, Br(Z \to e^+e^-)$ as a function of the top quark mass, m_t. The shaded bounds are theoretical predictions for $N_\nu = 3$, 5 and 7 neutrino types. The data points are the UA1 and UA2 measurements, and the combined result UA1 + UA2. This presentation is taken from ref. [40]. An analysis of all existing indications for N_ν has been done recently by P. Colas, D. Denegri and C. Stubenrauch, submitted to Z. Phys. C [41].

The ratio W/Z depends both on the top mass and on the number of neutrinos. The top channel weights in Z decay more, and the ratio decreases if $m_{top} < M_Z/2$. For any value of m_{top} an additional neutrino channel would weight more in W decay and it would increase the ratio. The data favor 3 neutrinos and to some extent also a low mass of the top quark.

The excess of inclusive single particles at large p_t over lower energy extrapolations observed at the ISR, turned into a major phenomenon of a large flux of energy emitted transverse to the SpS beams.

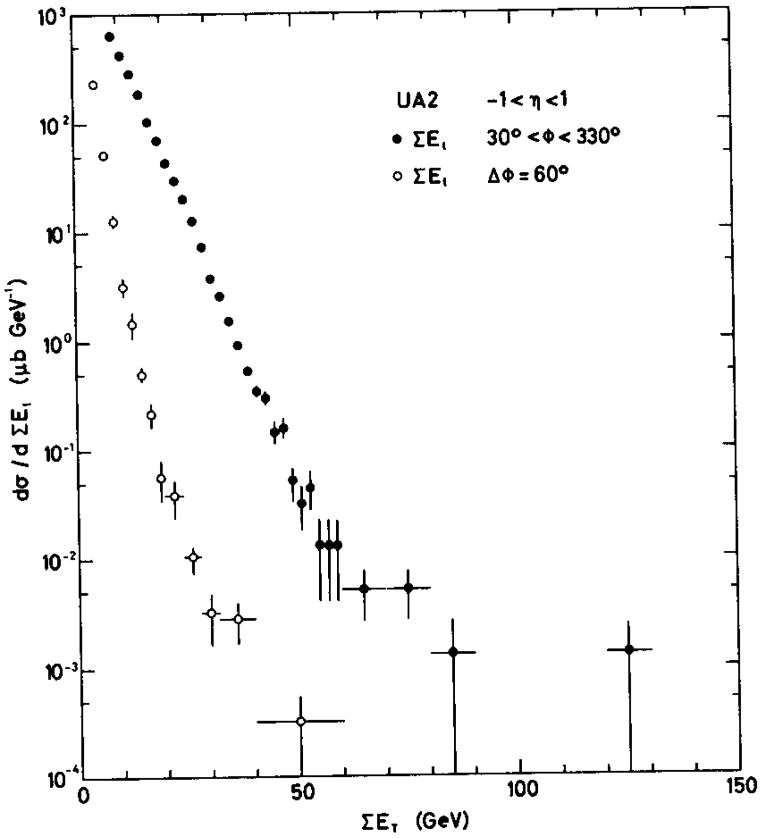

Fig. 9 Total E_T spectrum measured at the SPS $p\bar{p}$ collider (experiment UA2) at $\sqrt{s}$ = 540 GeV. Two azimuth ranges are shown; $|\eta| < 1$.

The onset of hadron jets, which was so difficult to determine at the ISR, was a spectacular effect at the SpS.The first unquestionable event was shown by UA2.

The jet energy was found by integrating over the calorimeter cluster. The jet cross section could be compared with QCD predictions after simulating the process leading from primary partons to jets.

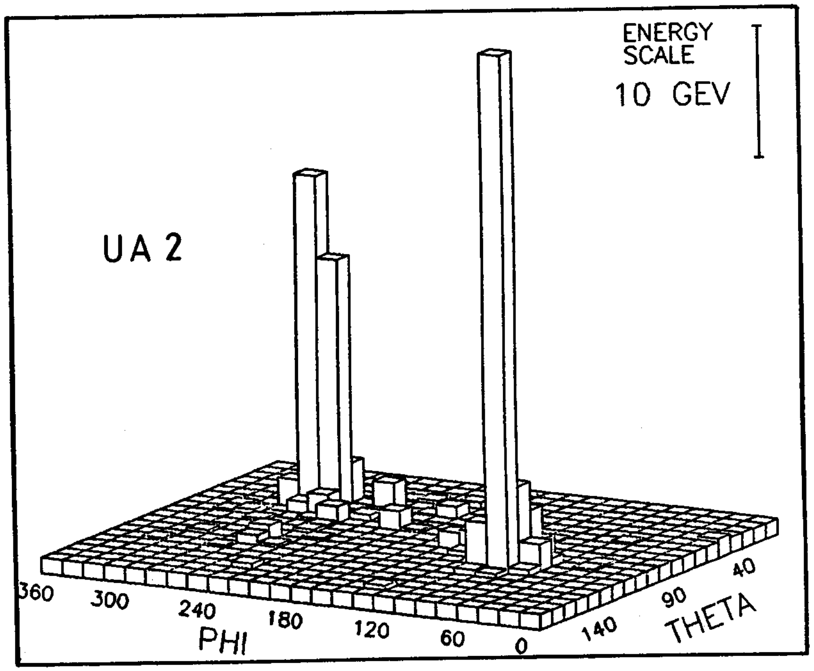

Fig. 10 The highest E_T event of Fig. 9, showing the E_T distribution in θ and ϕ (experiment UA2)

THE JET ENERGY SPECTRUM VERSUS QCD

Jets could be used to discover parton sub-structures in as much as these would manifest as deviation the QCD jet cross section at some large energy scale. Searches for such deviations with a null result were made by UA1/UA2 and extended to much larger p_t at the Fermilab Tevatron Collider.

JET PRODUCTION ANGULAR DISTRIBUTION VERSUS QCD

Although many amplitudes contribute to jet pair production, the jet angular distribution can be compared quantitatively with QCD since the most important sub-processes generating jets – gluon-gluon, quark-gluon, quark-antiquark scattering – have about the same angular dependence corresponding to vector boson (gluon) exchange:

$$\frac{d\sigma}{d\cos\theta^*_{ij}} \approx \frac{1}{\left(1-\cos\theta^*_{ij}\right)^2}$$

As a consequence, one can take the elementary cross section for partons i,j

$$\frac{d^3\sigma_{ij}}{dx_1 dx_2 d\cos\theta^*_{ij}} = \frac{F^i\left(x_1,Q^2\right)}{x_1}\frac{F^j\left(x_2,Q^2\right)}{x_2}\frac{d\sigma}{d\cos\theta^*_{ij}}$$

and replace the structure functions F_1^i, F_2^j with a single function built out of a combination of the quark and gluon structure functions, weighted according to the QCD strength of their couplings :

$$F^i(x) = F^j(x) = F(x) = G(x) + \frac{4}{9}\left[Q(x) + \overline{Q}(x)\right]$$

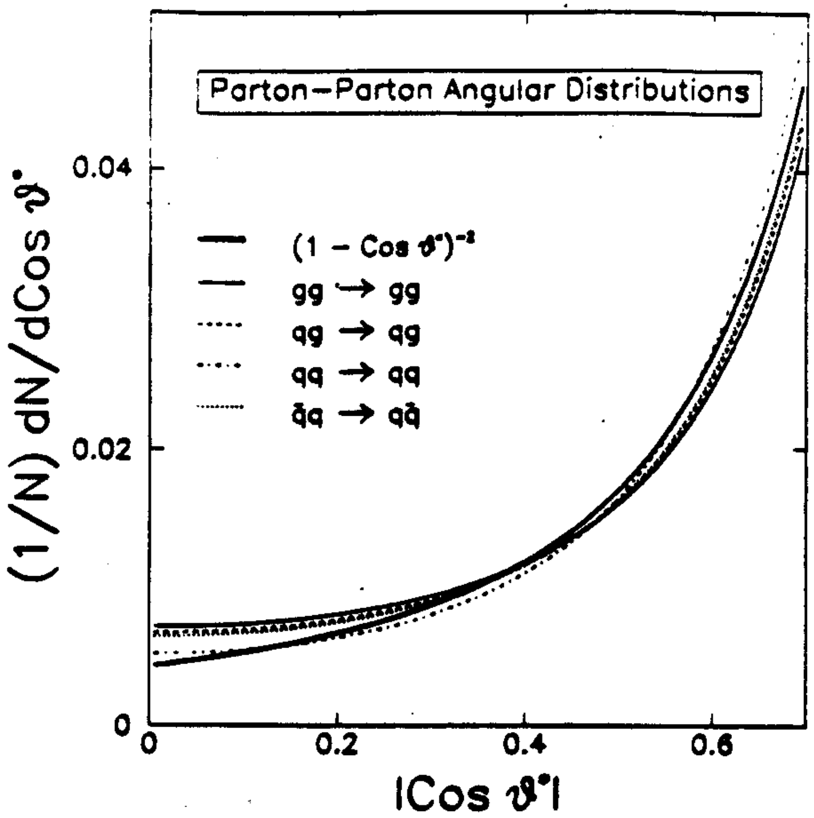

Figure 9: Calculated subprocess angular distributions for quark-antiquark, quark-gluon, and gluon-gluon scattering. The solid curve shows the expectation for Rutherford Scattering.

All subprocesses generating jet pairs give approximately the same angular distribution.

THE UA1 SEARCH FOR THE TOP QUARK

UA1 searched for a top quark of mass less than the W mass, produced either weakly in W decay or strongly as pair production:

$$p\bar{p} \to W + x \to t + \bar{b} + x \to l\nu b + \bar{b} + x, \quad or$$

$$p\bar{p} \to t + \bar{t} + x \to l\nu b + q\bar{q}\bar{b} + x$$

leading to final states with

-a jet from W decay, a lower energy jet, a lepton and missing p_t from top decay, or

-a jet and a lepton and missing p_t from one top, 3 lower energy jets from the other top which is assumed to decay hadronically.

In the first 1981-1985 run the signal was searched for in the muon as well as in the electron channels.

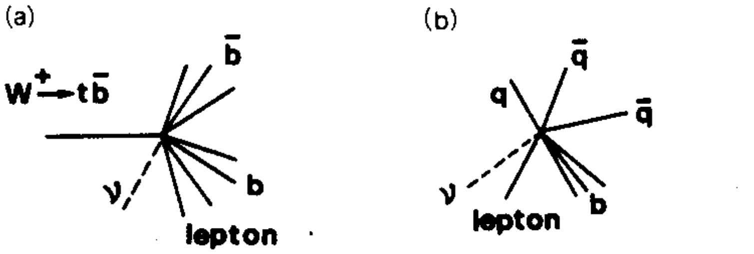

Fig. 3.32. Schematic representation of (a) the decays W→ t + $\bar{b}$ and (b) t + $\bar{t}$ production with t and $\bar{t}$ decaying in b + lepton + neutrino and three quarks.

The production rate in the $W\rightarrow tb$ channel can be promptly deduced from the measured $W\rightarrow e\nu$ rate as:

$$\sigma(W\rightarrow tb) = 3\sigma(W\rightarrow e\nu)\phi(m_t)$$

The factor of 3 is because of the 3 quark colors. The phase space factor $\phi(m_t)$ was easily computed (up to ~ 5% because of the uncertainty on the W mass). The top b.r. $t\rightarrow \nu eb$ is 11% in the S.M. Thus the expected signal in the W decay channel was well known.

The ttx QCD cross section was less well known, but for $40 < m_t < 75$ GeV the estimate was several times less than the W-channel cross section.

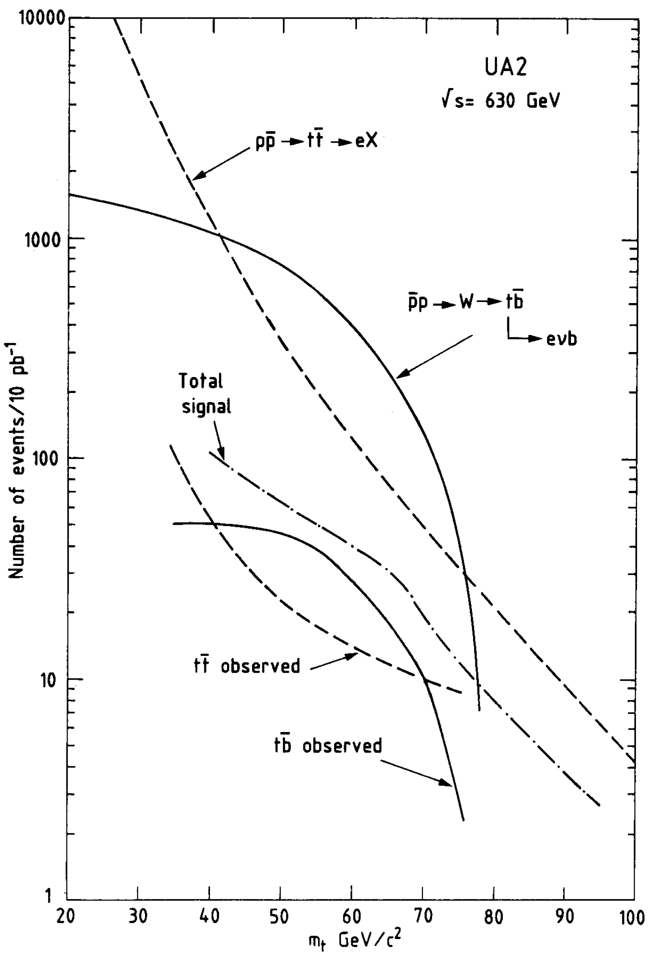

A W→tb decay would be followed by t→W*b and (~10% of times) W*→eυ decays.

The event would contain 2 b-jets, one electron and large missing E_t. The total mass would be the W mass, while a sub-system mass would indicate the mass of the top quark.

UA1 got some early indication for m_t ~ 40 GeV. However, it was later understood that the events were background, probably from bb+jet production.

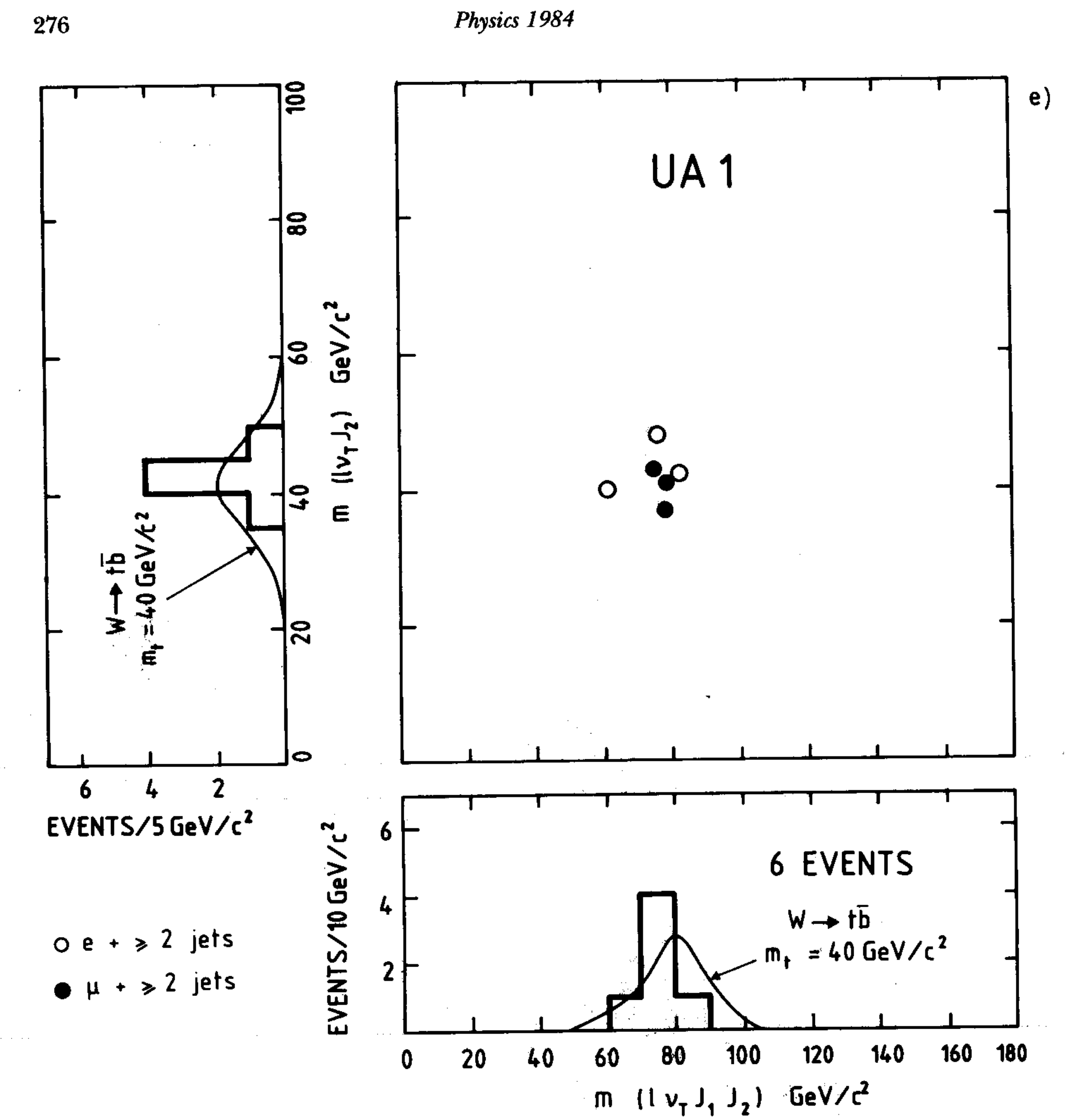

G.Arnison et al, Phys.Lett. B147 (1984), 493.

THE SECOND GENERATION UA1 FOR THE TOP SEARCH

In order to avoid signal pileups in the π-wide gondolas at the higher expected luminosity, the e.m.calorimeter was redesigned into a tower structure using warm heavy liquid as sensitive medium (tetramethyl pentane, TMP) and uranium converter plates. The gondolas were removed early in 1986 to leave room for the new detector. However, this was not completed on time.

Moreover, since the new detector extended down to the beam pipes in order to be more hermetic, also the forward arms had been removed. The forward coverage of UA1 was thus limited to that of the hadron calorimeter, $-3 < \eta < +3$. Consequently the $E_{t,miss}$ resolution was less good, $(\Delta E_{t,miss}/E_{t,miss}) \sim 80\%/\sqrt{E(GeV)}$. The hadron calorimeter was re-calibrated as with no material in front, and the muon detector was improved to cover $-2,3 < \eta < +2,3$.

Because of this inconvenience UA1 started late the 1988-1989 run and could search for the top only in the muon channels.

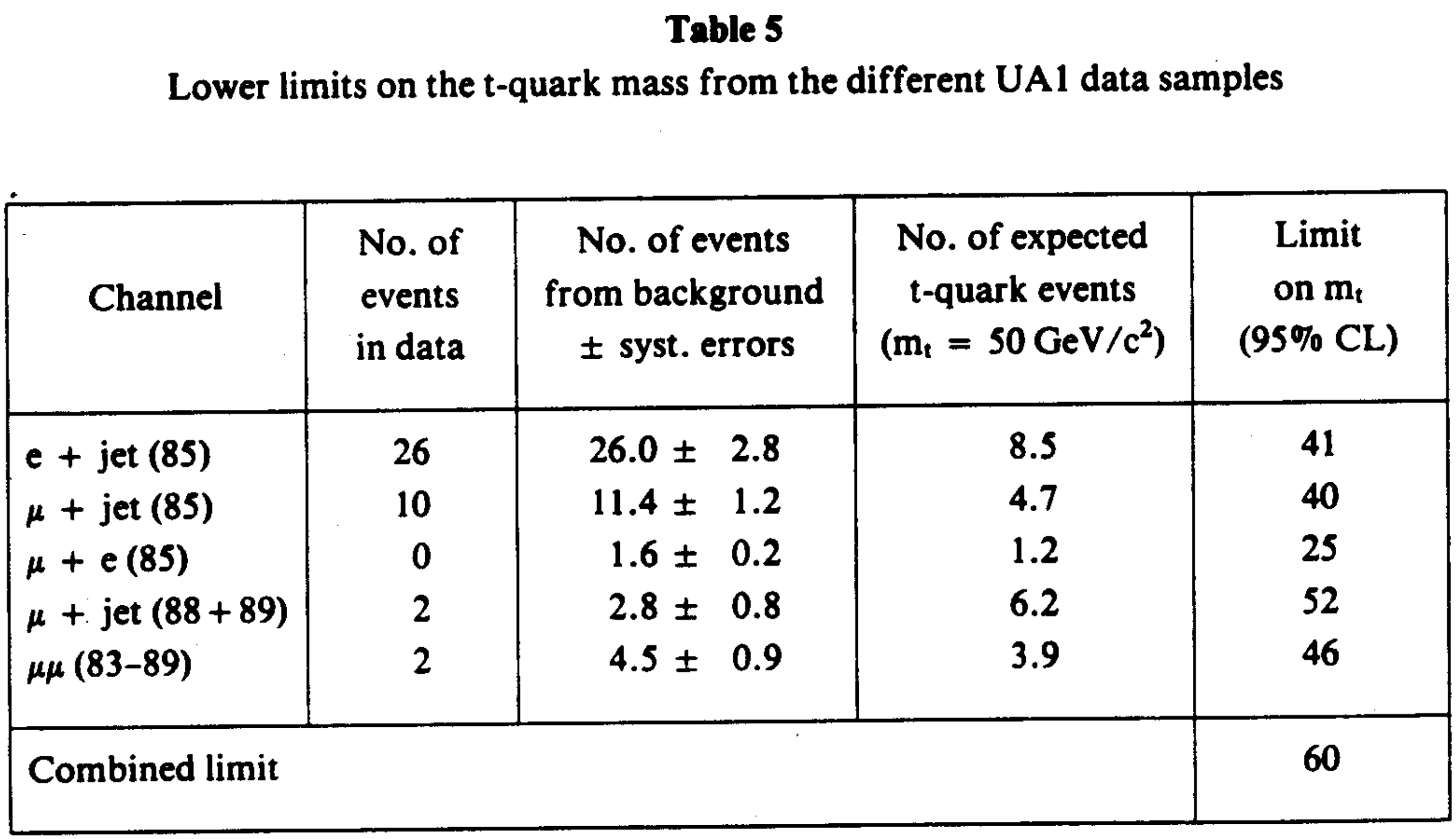

Table 5

Lower limits on the t-quark mass from the different UA1 data samples

Channel	No. of events in data	No. of events from background ± syst. errors	No. of expected t-quark events (m_t = 50 GeV/c^2)	Limit on m_t (95% CL)
e + jet (85)	26	26.0 ± 2.8	8.5	41
μ + jet (85)	10	11.4 ± 1.2	4.7	40
μ + e (85)	0	1.6 ± 0.2	1.2	25
μ + jet (88 + 89)	2	2.8 ± 0.8	6.2	52
$\mu\mu$ (83–89)	2	4.5 ± 0.9	3.9	46
Combined limit				60

The statistics collected by UA1 in the 1988-1989 run was similar to that already collected in 1995.

The final UA1 limit to the top quark mass was presented in 1990, based on 4,7 pb^{-1} of data collected in 1988-1989 and including the analysis of the $t \to \mu\nu$ search:

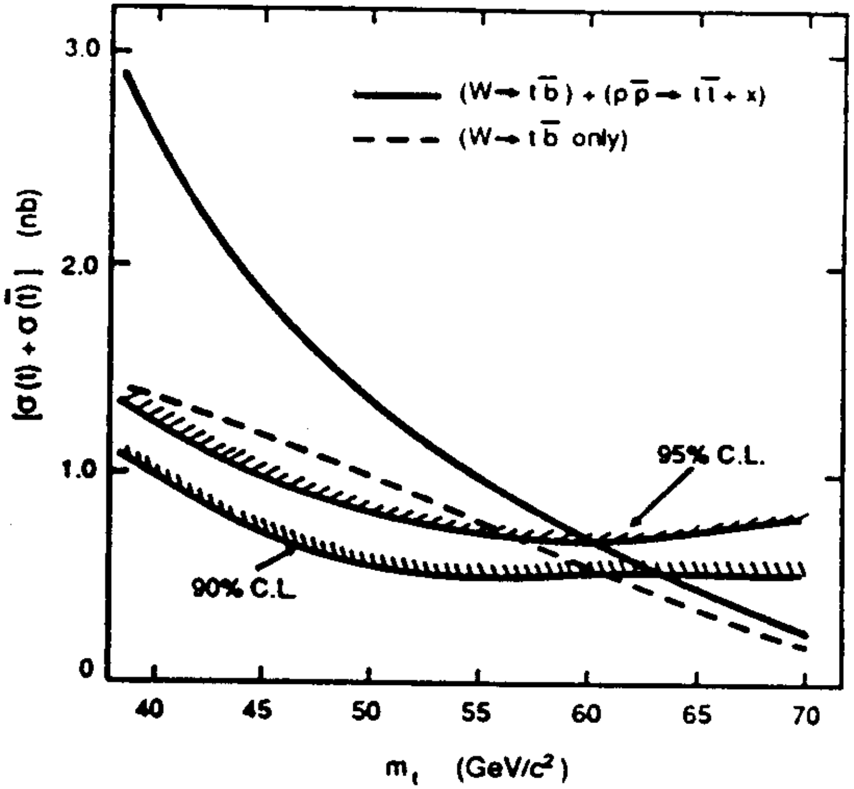

$m_t > 60$ GeV with 95% c.l..

S.Lammel, Proc. of the 1990 La Thuile Rencontre, p. 435.

THE SECOND GENERATION UA2

In 1986-87 the UA2 detector was greatly modified, in order to:

a) Improve the electron signature. A cylindrical central tracker was built including very light “jet chambers” inside, a layer of silicon pads to reject photons converting in the tracker, a transition radiation detector to signal electrons, and a scintillating fiber tracker/converter to signal the electron trajectory at the calorimeter entrance.

b) Improve the missing E_t resolution. The forward detectors were completely remade and the toroidal spectrometers were replaced with electromagnetic and hadronic calorimeters similar to the large angles ones.

==

J.M.Gaillard, Proc. Of the Int. Sym.on Physics of P.-Antip. Coll., Tsukuba, 1985, p.254.

L.Mapelli, proc. of the 1988 La Thuile Rencontre, p.613 .

The second generation UA2 was a full coverage em + hadron calorimetric detector.

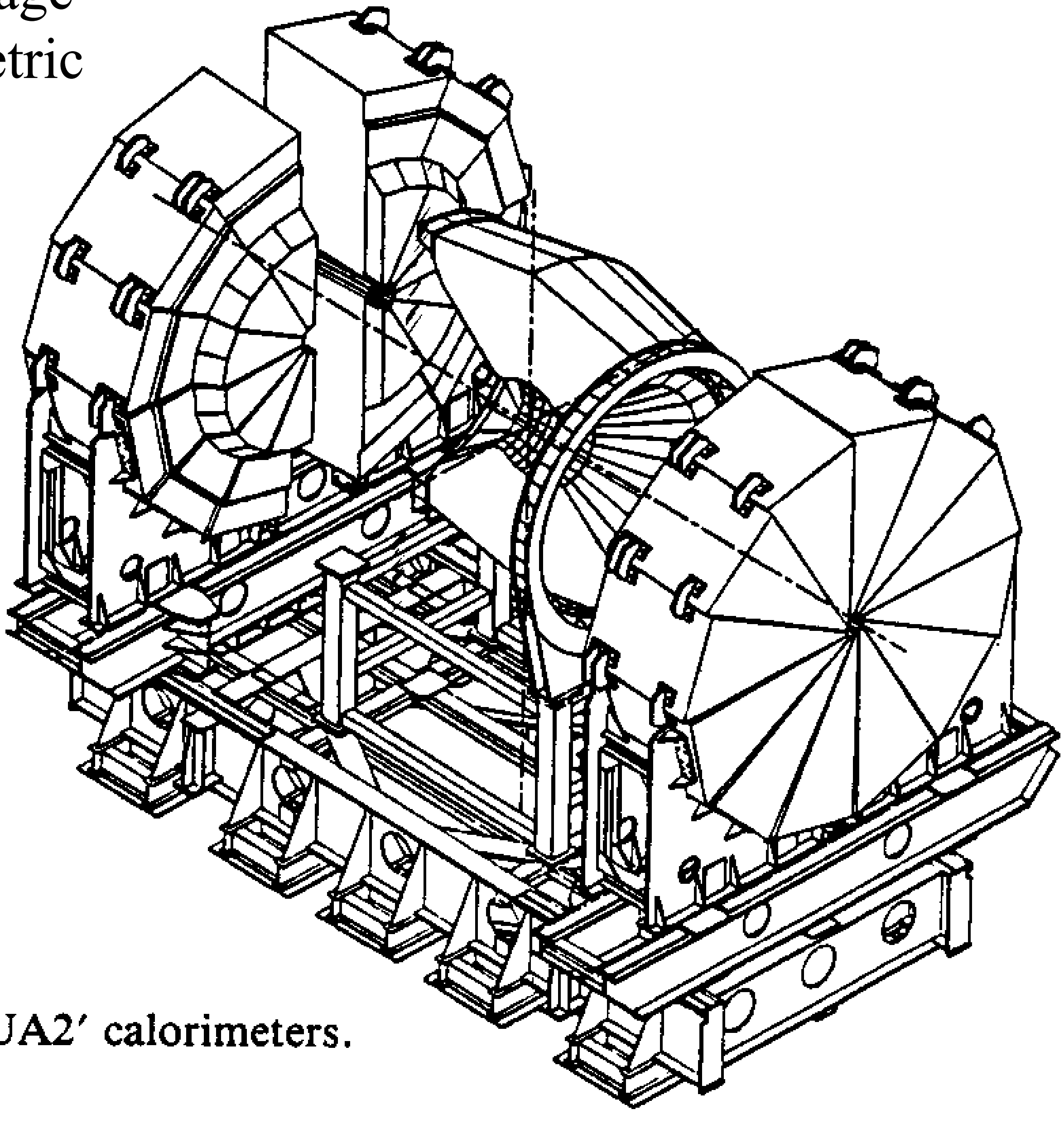

' the UA2′ calorimeters.

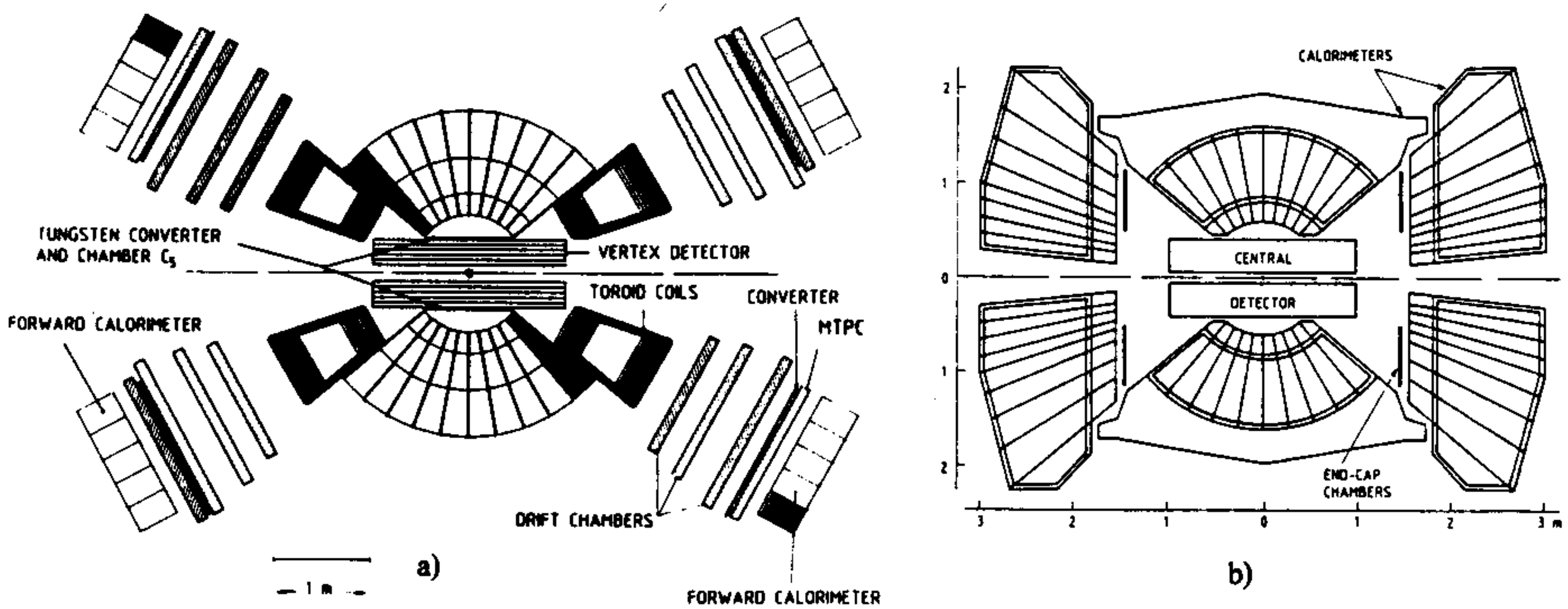

Fig. 7 Longitudinal view showing the different calorimetry of a) UA2 and b) UA2′.

Even the edges of the old central calorimeter were cut away in order to allow making the UA2 calorimeter more hermetic.

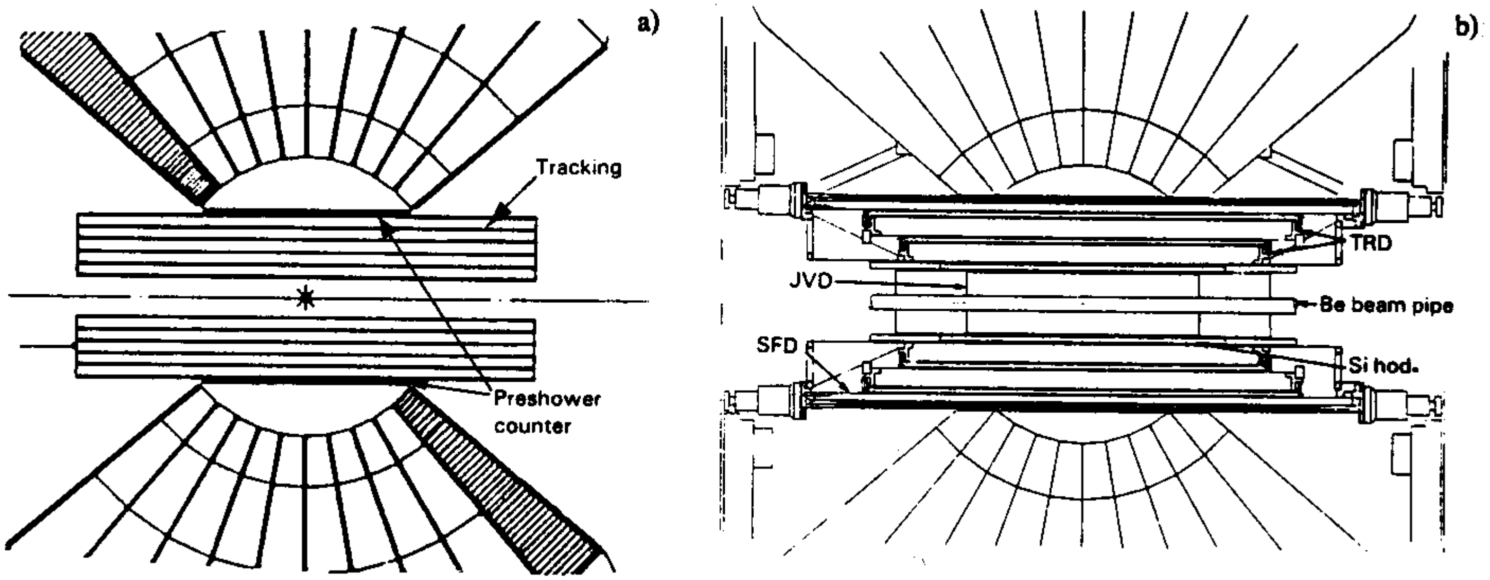

Fig. 1 Longitudinal view of the central detectors of a) UA2 and b) UA2′. Note the smaller beryllium beam pipe and the shortened calorimeter edges of UA2′.

Background electrons due to late photon conversion do not give signal in the silicon pad hodoscope which is behind the jet chamber. The 4 cm thick scintillating fiber package SFD has 4 triplets of stereo layers in front of a 1,5 cm thick lead sheet. Two more triplets follow the lead converter to signal electrons.

THE UA2 SEARCH FOR THE TOP QUARK

The last years of SpS collider running , from winter 1987 to spring 1990 were devoted primarily to the effort to find the top quark. The lower limit to the top mass reached in 1988 from the analysis of the ~900 nb^{-1} of the first SpS collider run was 56 GeV. It was estimated that in the 10 pb^{-1} to be integrated in a second run, the top quark could be detected (with > 150 events) as long as its mass was not larger than ~ 75 GeV.

The search was based on a study of the $e\nu$ transverse mass in W events. In top decay the W would be virtual and it would appear as a lower mass signal in the transverse mass plot.

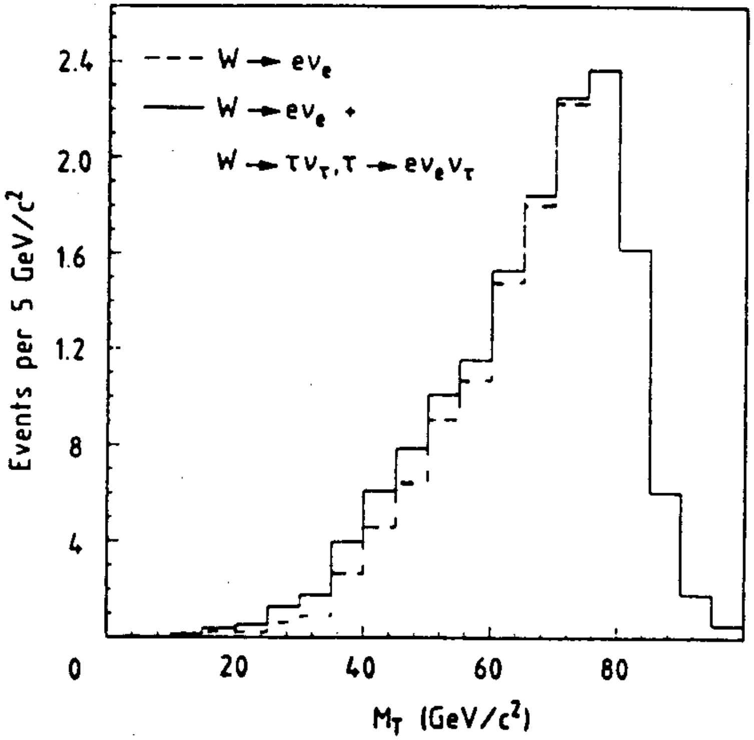

Fig.5 $M_T^{e\nu}$ distribution for W events

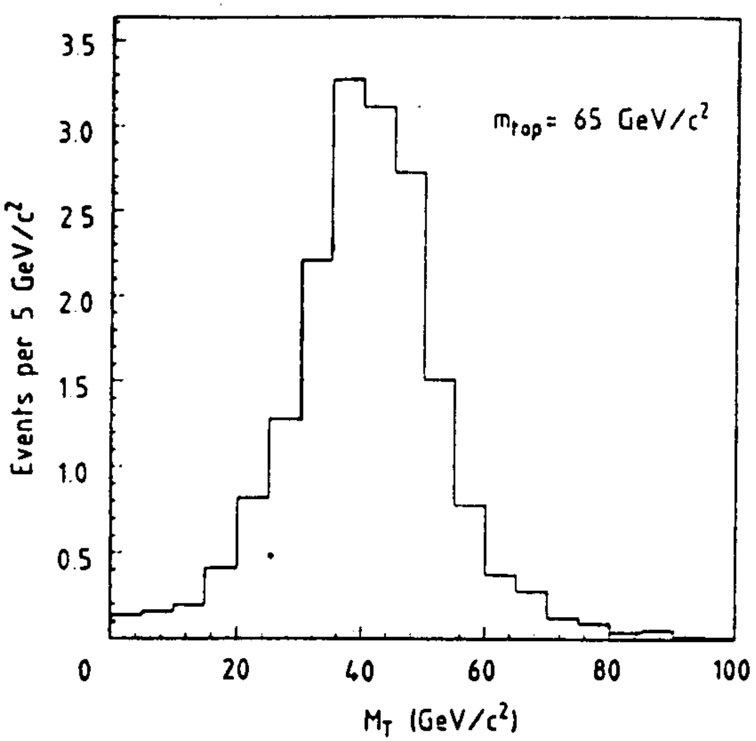

Fig.6 $M_T^{e\nu}$ distribution for 65 GeV top.

Monte Carlo simulations showed that the virtual W* peak would be confused with the left W tail if the top mass would be too close to the W mass (larger than ~ 70 GeV).

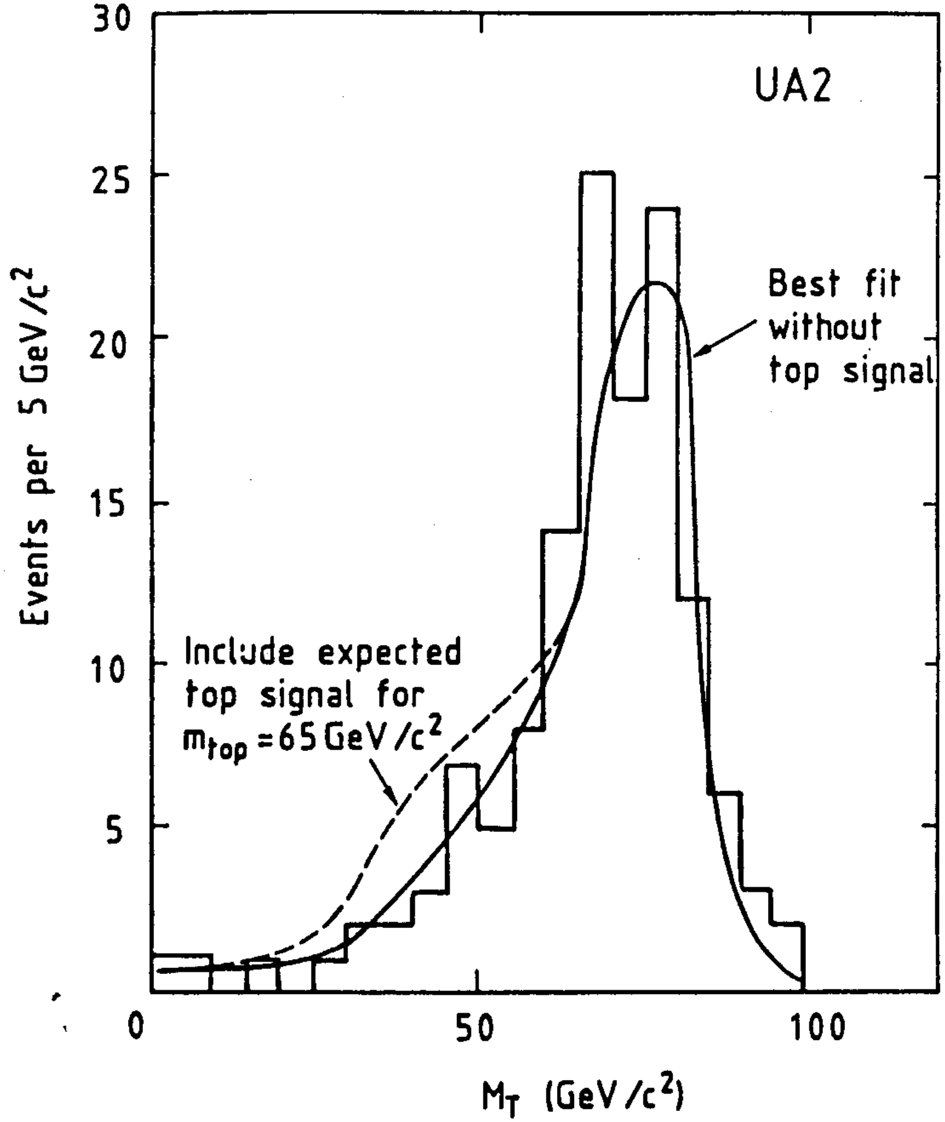

Fig.7
Best fit (full curve) to the $M_T{}^{e\nu}$ distribution of fig.5 with no top signal. The lowest expected contribution from 65 GeV top is added (dashed curve).

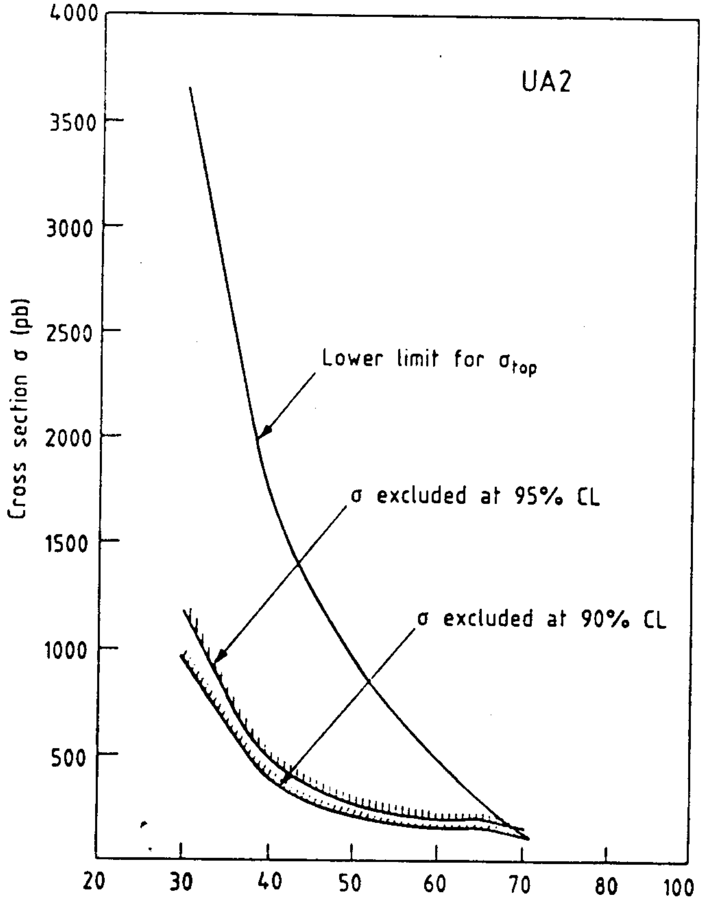

Fig.8
Lower limit for the top production cross-section and the 90 and 95% CL excluded cross-sections as a function of top quark mass.

The final UA2 lower limit was 69 GeV at a 95% c.l. . The top mass was too large to allow a sufficient rate at the SpS. The collider was shut down about one year later.

TOTAL AND ELASTIC SCATTERING BY UA4

UA 4 was located left and right of UA2. The experiment measured the small angle elastic scattering including the real part of the forward elastic amplitude . The total cross section was also measured by comparing the forward elastic to the total elastic+inelastic rate.

The elastic scattering detector was a set of small drift chamber telescopes located in “roman pots”. In order to cover a wider t-range, including the coulomb interference region around $t \sim 10^{-3}$ $^{(}$GeV/c$)^2$, a number of runs were made with beams from strongly focused at the crossing point (low local betatron wave length β) to nearly parallel beams (high β). Overall the t-range covered was

$$0{,}001 < -t < 1{,}5\ (\mathrm{GeV}/c)^2 .$$

The total inelastic rate was measured with two drift chamber spectrometers located left and right around the beam pipes, which tracked charged prongs down to pseudorapidity $|\eta| = 5{,}6$.

UA4 LAYOUT

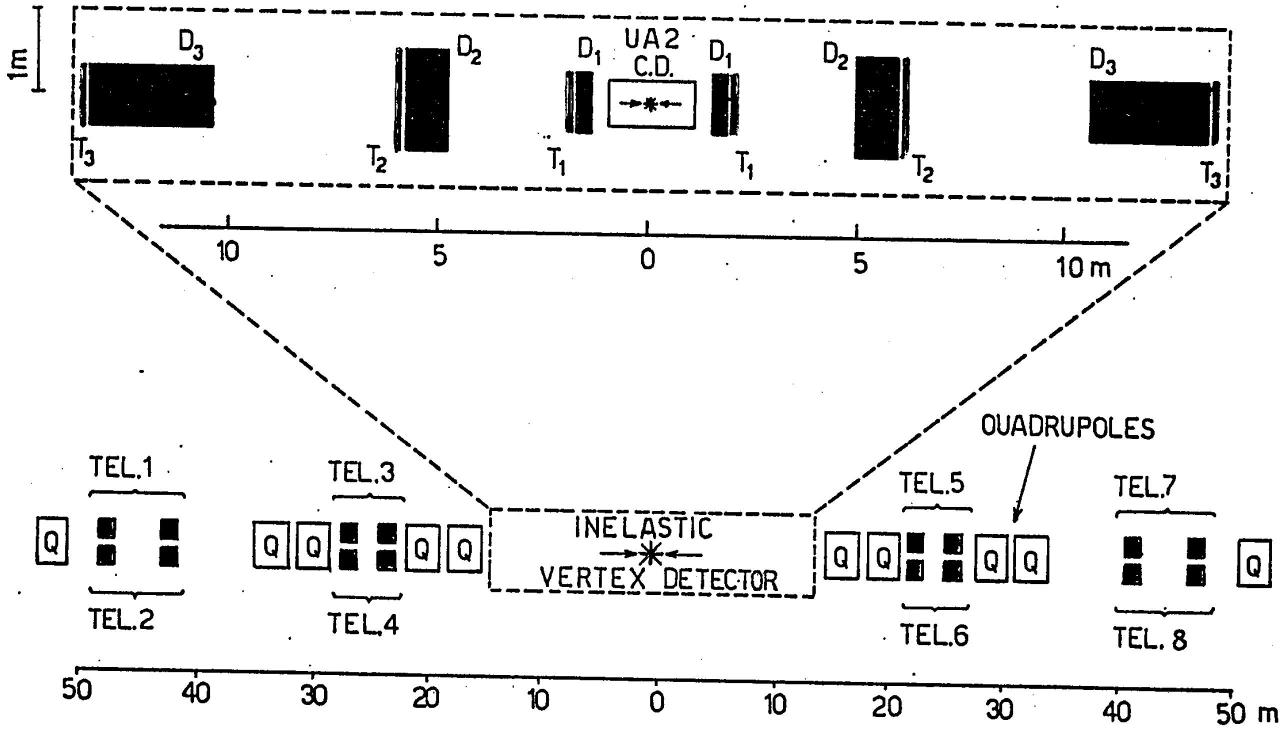

UA4 was located on the two sides of UA2 and used the UA2 detector for his measurement of the total inelastic rate. Telescopes 1,2,7,8 measured small angle elastic scattering. Telescopes 3,4,5,6 measured intermediate angle inelastic events.

MEASURING σ_t BY COMBINED MEASUREMENTS OF TOTAL RATE AND OF FORWARD ELASTIC RATE

Allowing for a fraction ρ of real to imaginary part of the scattering amplitude in the forward direction, neglecting spin effects and making use of the optical theorem, assuming an exponential t-dependence of the cross section with slope b around t = 0, the following relations hold:

$$\sigma_t{}^2 = \frac{16\pi}{1+\rho^2}\left(c.{h}/{2\pi}\right)^2 \frac{1}{L}\left(\frac{dR_{el}}{dt}\right)_{t=0}$$

$$\sigma_t = \frac{R_{el}+R_{inel}}{L}$$

$$\sigma_t\left(1+\rho^2\right) = 16\pi\left(c.{h}/{2\pi}\right)^2 \frac{bN_{el}}{N_{el}+N_{inel}}$$

where L is the integrated luminosity and N_{el} and N_{inel} are the total elastic and inelastic events in the same run or in a run of the same luminosity.

==

G.Sanguinetti, Proc. of the 3rd Moriond Workshop, 1983, p.25.

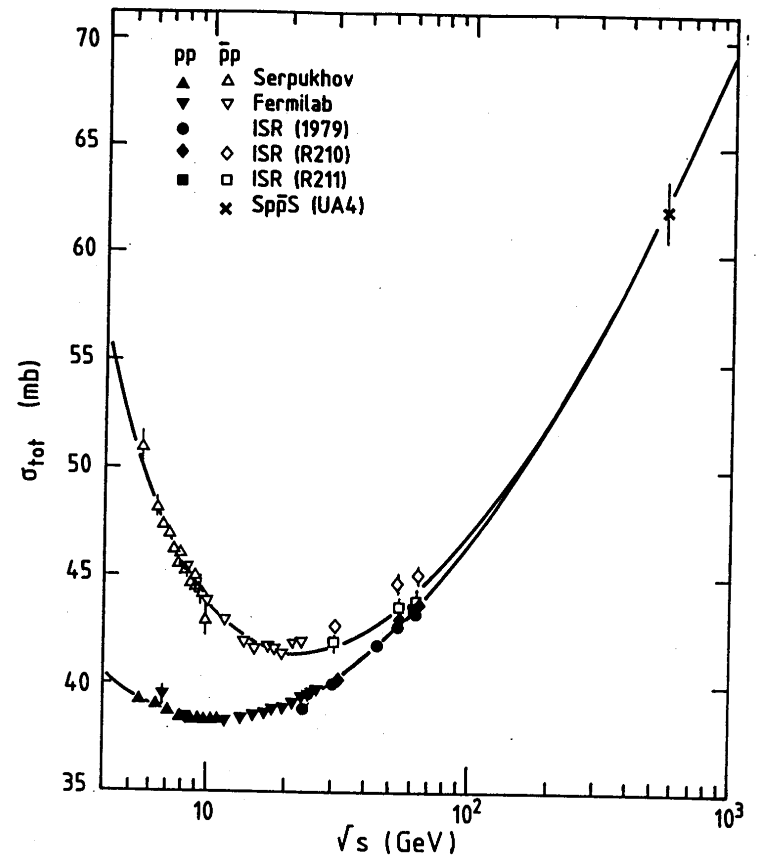

Figure 11. Total cross-section data for pp and $\bar{p}p$ scattering [early, low-statistics measurements at the SPS Collider (18,35) are not shown]. The curve represents the dispersion relation fit of Reference (7).

The σ_t result was consistent with the presumption that proton and antiproton total cross section were becoming sensibly equal, and with an increase of σ_t as $\log^2 s$ from the ISR.

The result $\rho = 0,24 \pm 0,4$, was much larger than expected. The following possible sources of systematic errors should be mentioned:

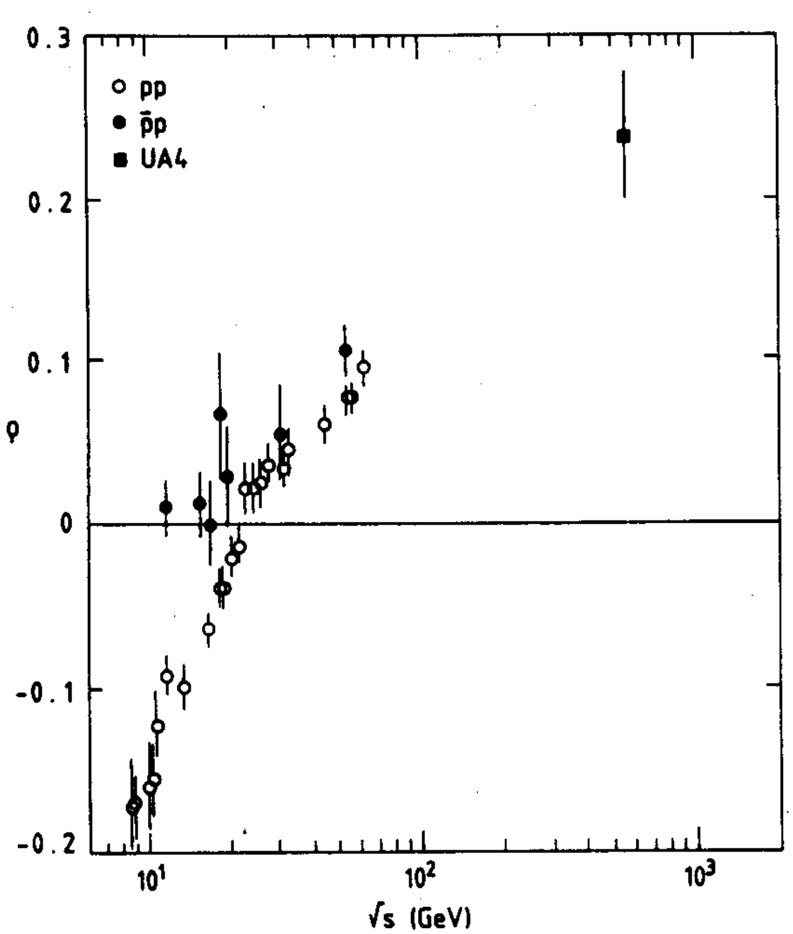

Fig. 4. The present result on the parameter ρ is shown together with lower energy data for pp and p̄p elastic scattering.

- the slope b of the forward peak was assumed to be constant below t – 0,06 GeV^2 , with $b = 15,7\ \mathrm{GeV}^2$. If the slope would sharpen towards zero σ_t would be larger and ρ would be smaller;

- ρ was assumed to be a constant in the same t range. If instead the slope of the real part would be smaller of the slope of the imaginary part, ρ would be smaller.

The total cross section was as predicted for proton-proton assuming an $\ln^2 s$ dependence. The increase from the ISR was by nearly 50%.

$\sigma_t(p\text{-}\bar{p})(1+\rho^2) = 63.3 \pm 1{,}5$ mb at 546 GeV
$\sigma_t = 60 \pm 0{,}2$ mb, given that $\rho = 0{,}24 \pm 0{,}04$

The elastic to total cross section ratio was surprisingly higher than at the ISR:

$\sigma_{el}/\sigma_t = 0{,}213 \pm 0{,}06$ at 546 GeV.

This was an increase by about 20% from the ISR (where it was ~ 17,5%), showing that the SpS energy range was not asymptotic yet.

The similarity between p-p and p-p scattering was limited to the forward peak. The first diffraction maximum started at lower p_t and was much less pronounced.

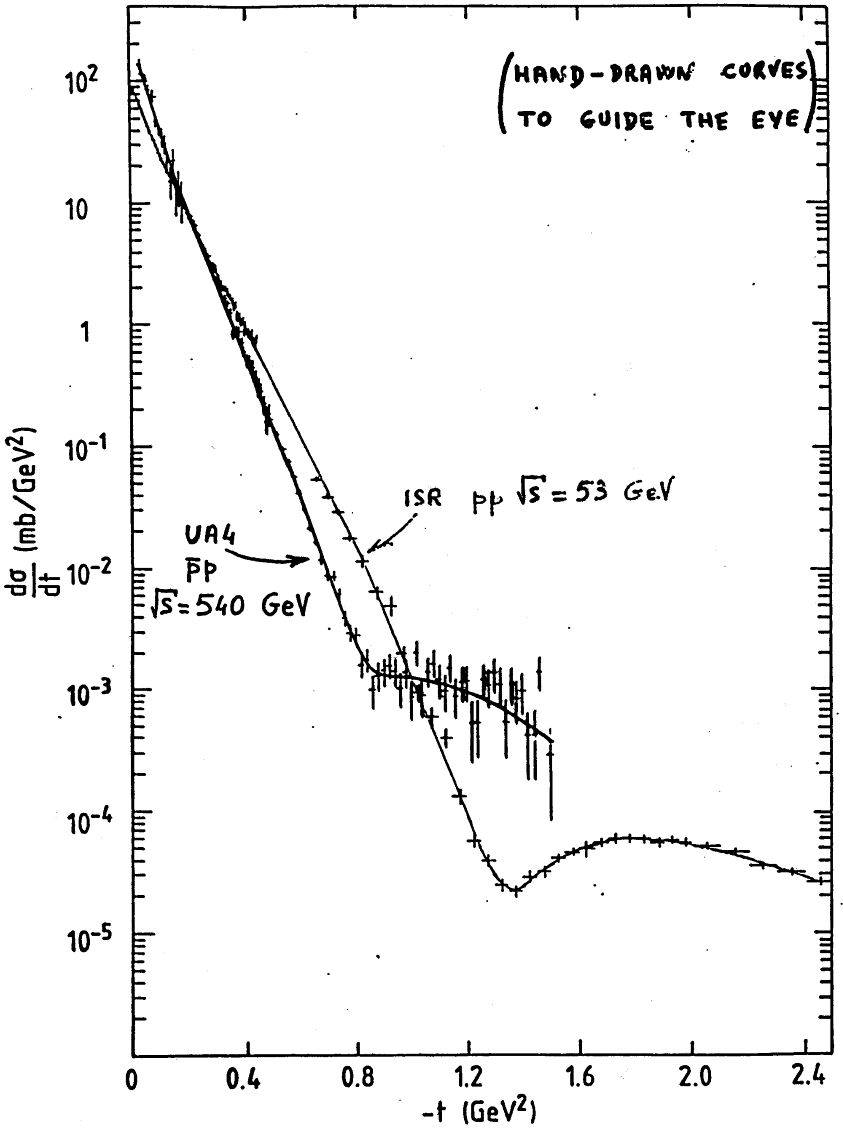

THE UA5 EXPERIMENT

UA5 used a streamer chamber that could take data at ~ 1Hz and track almost all charged particles generated in an interaction. The goal was to measure the main features of inelastic events. Photons could also be detected by inserting a sheet of converter material in front of the visible region. Measurements included:

-the energy dependence of the mean charged multiplicity
-the mean photon multiplicity
-the increase of the mean p_t of secondaries with increasing event multiplicity

260 *UA5 Collaboration, UA5: A general study of proton–antiproton physics at $\sqrt{s} = 546$ GeV*

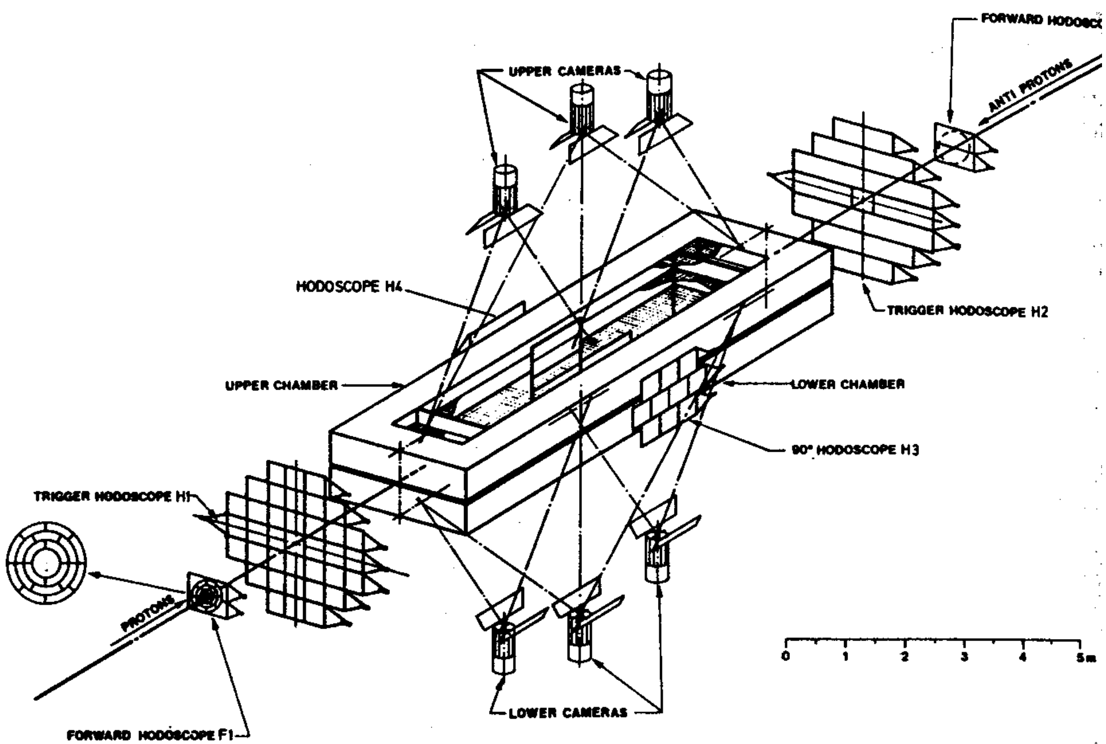

Fig. 2.2. Schematic layout of the streamer chamber system.

Two identical 6m long streamer chambers were located above and below the interaction point. Each chamber contained two 25 cm high volumes, with grounded walls and the HV plane in the middle. Voltage was raised to ~ 375KV by a trigger and tracks were photographed.

G.J.Alner et al.,Physics Reports 154, no.5 (1987), p.247.

Hadron decays like $K_s \rightarrow \pi\pi$ and $K_l \rightarrow \pi\pi\pi$ could be observed.

UA5 Collaboration, UA5: A general study of proton–antiproton physics at $\sqrt{s} = 546$ GeV 295

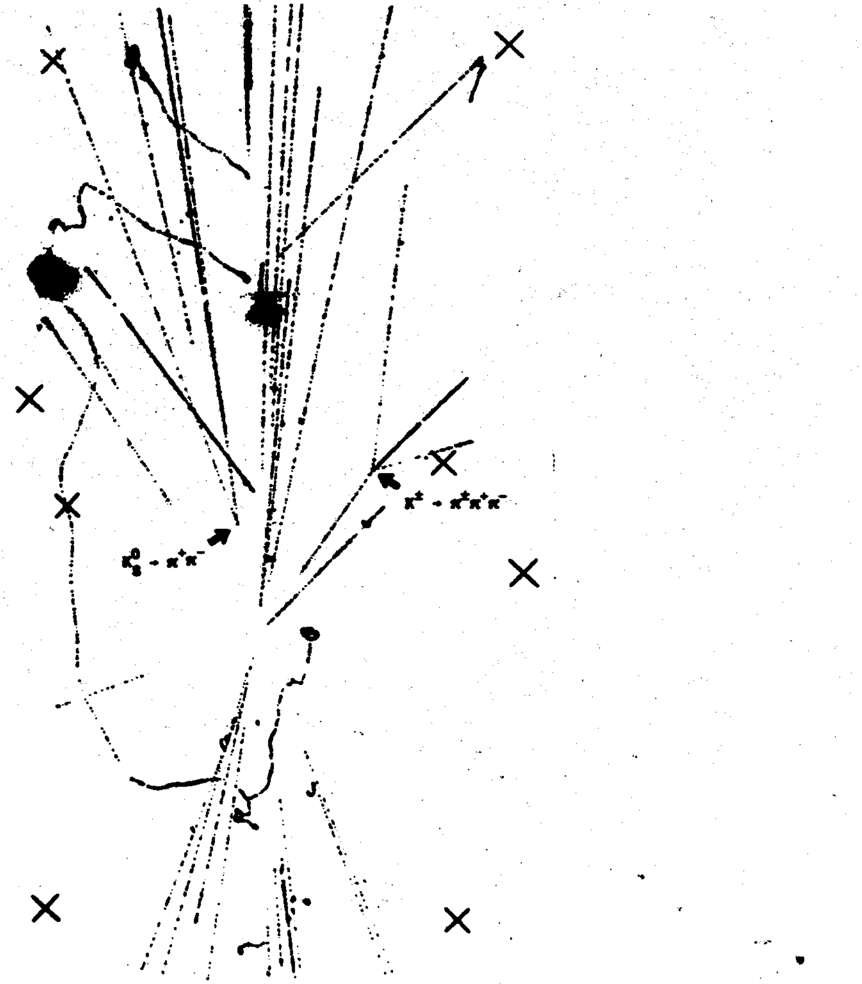

Fig. 3.14. Photograph of an event as seen in one of the streamer chambers. The arrows point to the decays of a K^0_s and a $K_{\pi 3}$ respectively.

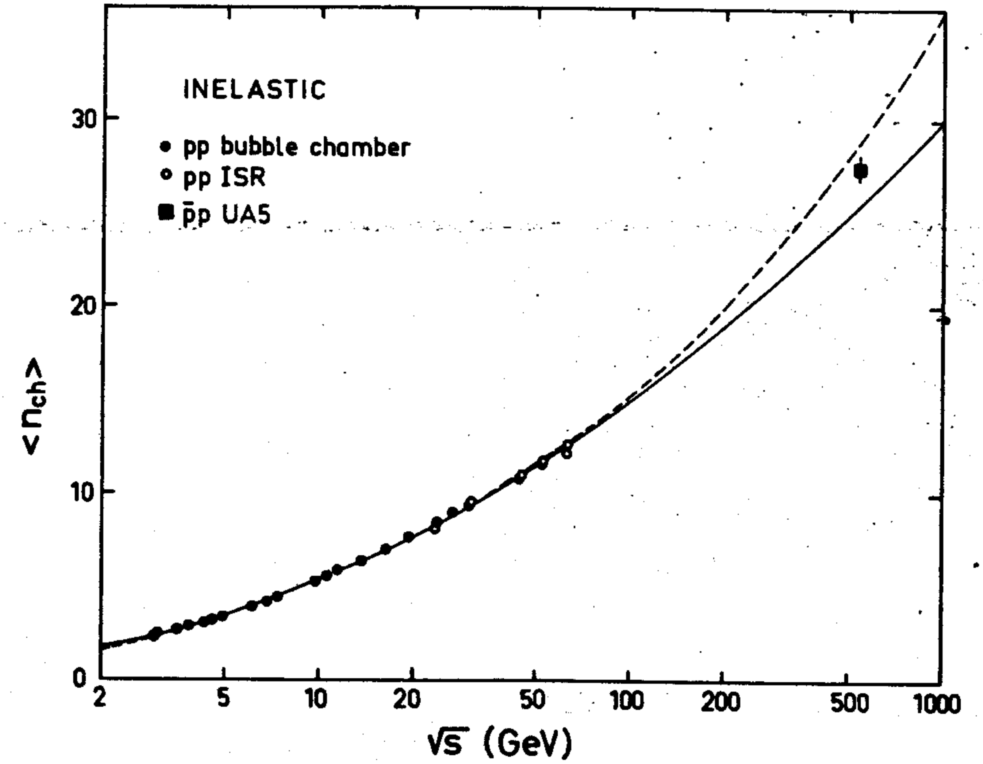

Fig. 4.3. Mean charged multiplicity in all inelastic pp or $p\bar{p}$ events as a function of c.m. energy, $\sqrt{s}$. The curves are fits to the data, as in fig. 4.2, over the energy range $\sqrt{s} = 4–546$ GeV, with parameters given in table 4.1.

Multiplicity distributions of prongs in inelastic events, as well as inclusive pseudorapidity distributions could be integrated to give the mean charged multiplicity at 546GeV:

$$<n_{ch}>_{inelastic} = 27{,}5 \pm 0{,}7$$